Dipl.-Ing. Alexander Schiffmann

Creation and Characterization of Tailored Plasmonic Nanoparticles

DOCTORAL THESIS

to achieve the university degree of

Doktor der technischen Wissenschaften

submitted to

Graz University of Technology

Supervisor

Univ.-Prof. Dipl.-Phys. Dr.rer.nat Wolfgang E. Ernst

Co-Supervisor

Dipl.-Ing. Dr.techn. Florian Lackner

Institute of Experimental Physics

Graz, October 2020

Affidavit

I declare that I have authored this thesis independently, that I have not used other than the declared sources/resources, and that I have explicitly indicated all material which has been quoted either literally or by content from the sources used. The text document uploaded to TUGRAZonline is identical to the present doctoral thesis.

Date	Signature

Acknowledgement

First of all, I want to sincerely thank Prof. Wolfgang E. Ernst for giving me the opportunity to experience the merits of scientific work first hand. He supported me all the way towards this thesis with his experience and encouraged me to give my best.

It was a pleasure for me to work together with so many nice colleagues during the four years I spent at the IEP. The whole institute is a well operating machinery and I enjoyed to meet all the people from various scientific groups, the secretariat, and the workshops.

Martin Schnedlitz and Maximilian Lasserus introduced me to the helium droplet synthesis approach and the laboratory, with Roman Messner I shared the office and the apparatus during the second half of my thesis, and with Thomas Jauk I spent the better part of a year in the basement setting up the NanoESCA laboratory. I had a great and productive time with all of them. Special thanks go to Florian Lackner, who always had an open ear and supported me in many ways. With his valuable experience in the laboratory he was the first responder whenever a problem occurred or additional input was needed. I am happy that these reliable coworkers became friends during my time at the IEP.

For over ten years the core of my social life in Graz has been a group of fellow students that I befriended as an undergraduate. I am very grateful for all the inspiring discussions and the fun I have with them.

Finally, I want to thank my whole family and especially my wonderful wife for their unreserved and caring support. Their love is the base for every achievement in my life.

Abstract

The helium droplet synthesis approach is already a well established method for the production of tailored nanoparticles. With their unique properties the helium droplets serve as a pristine nanolab, in which a wide range of different nanoparticle types can be synthesized. In a reproducible and reliable process e.g. core@shell particles are formed by subsequent doping with two different metals. The approach has the advantage of dispensing no chemicals or other additional additives besides the high purity metals and the superfluid helium matrix. Due to features arising from the superfluidity, also elongated nanorods and nanowires can be formed. All those shapes and a variation of sizes are readily accessible by adjusting a small set of parameters at the apparatus.

The present thesis focuses on the advance of the synthesis approach from pure fundamental research aspects towards possible applications. Several investigative methods were employed on the produced nanoparticle samples for the first time, in addition to the well established analysis by scanning transmission electron microscopy: electron energy loss spectroscopy, surface enhanced Raman spectroscopy, photoemission electron microscopy, ultraviolet photoelectron spectroscopy, two-photon photoelectron spectroscopy, and XUV absorption spectroscopy. It is shown that the helium droplet approach is suitable for the formation of plasmonic active structures like Ag@Au core@shell nanoparticles with a shifting localized surface plasmon resonance in dependence of the material ratio. Also the combination of a plasmonically active Ag core with a stable and uniformly shaped ZnO shell is examined in detail. Furthermore, the search for new substrates is covered with the first reported application of ultra-thin hexagonal boron nitride in nanoscale plasmon spectrosocpy.

Overall, the reported new material combinations and the experimental upgrades towards the production of high density nanoparticle surfaces on various substrates are likely to draw the attention of a wider audience towards the intriguing possibilities the helium droplet synthesis approach offers. The findings in this thesis will build a foundation for future application-oriented research.

Kurzfassung

Die Heliumtröpfchenmethode ist ein bereits sehr gut etabliertes Verfahren zur Herstellung von maßgeschneiderten Nanopartikeln. Die Heliumtröpfchen mit ihren einzigartigen Eigenschaften agieren dabei als ultra-reine Nano-Labore in denen eine große Vielfalt an verschiedenen Nanopartikeln hergestellt werden kann. So können zum Beispiel Core@Shell Partikel in einem sehr zuverlässigen Prozess durch das aufeinanderfolgende Dotieren mit zwei verschiedenen Metallen synthetisiert werden. Ein großer Vorteil dabei ist, dass keine Chemikalien oder andere Zusätze verwendet werden müssen. Für die Synthese werden nur hochreine Metalle und die suprafluiden Tröpfchen benötigt. Aufgrund von speziellen Eigenschaften, die sich aus der Suprafluidität ergeben, können auch längliche und fadenförmige Partikel geformt werden. Um bei der Herstellung zwischen den verschiedenen Formen und Größen zu wechseln, ist es ausreichend einige wenige Parameter an der Apparatur zu verändern.

Die vorliegende Doktorarbeit beschäftigt sich vor allem mit dem Voranbringen dieser Methode in Richtung möglicher Anwendungen. Abseits der etablierten Rastertransmissionselektronenmikroskopie wurde dazu eine Reihe von Messmethoden erstmals an den synthetisierten Nanopartikeln durchgeführt: Elektronenenergieverlustspektroskopie, oberflächenverstärkte Ramanspektroskopie, Photoemissionselektronenmikroskopie, UV-Photoelektronenspektroskopie, Zwei-Photonen Photoemissions-Spektroskopie und XUV Absorptionsspektroskopie. Außerdem wird gezeigt, dass sich die Heliumtröpfchenmethode ausgezeichnet für die Herstellung von plasmonisch aktiven Strukturen wie etwa Ag@Au Core@Shell Nanopartikeln eignet. Diese zeigen auch eine veränderliche Resonanz der lokalisierten Oberflächenplasmonen in Abhängigkeit vom Verhältnis der beiden Metalle. In einem weiteren Experiment wurde ein plasmonisch aktiver Ag Kern mit einer sehr gleichmäßigen ZnO Schicht ummantelt und analysiert. Mit der erstmaligen Anwendung von ultra-dünnen h-BN Schichten in der Plasmonen Spektroskopie auf Nano-Ebene wird auch die Suche nach neuartigen Substraten thematisiert.

Insgesamt lässt sich mit den vorgestellten neuen Materialkombinationen, der Weiterentwicklung der Heliumtröpfchenmethode und den vielversprechenden Möglichkeiten, die damit einhergehen, ein breites Publikum ansprechen. Die präsentierten Ergebnisse bilden damit eine Grundlage für zukünftige Experimente, die noch stärker in Richtung anwendungsorientierter Forschung gehen werden.

Scientific Output

The following list includes all peer reviewed scientific papers containing contributions from the author in chronological order of publication. All articles were published during the author's engagement as a PhD student at the Institute of Experimental Physics. The scientific papers (4), (5), (7) and (8) are reprinted as part of this doctoral thesis in Chapters 3, 4, 6 and 5 respectively.

(1) "Thermally induced alloying processes in a bimetallic system at the nanoscale: AgAu sub-5 nm core–shell particles studied at atomic resolution" by Maximilian Lasserus, Martin Schnedlitz, Daniel Knez, Roman Messner, **Alexander Schiffmann**, Florian Lackner, Andreas W. Hauser, Ferdinand Hofer, and Wolfgang E. Ernst in *Nanoscale* **10**, 2017–2024 (2018).
https://doi.org/10.1039/C7NR07286D

(2) "Spectroscopy of gold atoms and gold oligomers in helium nanodroplets" by Roman Messner, **Alexander Schiffmann**, Johann V. Pototschnig, Maximilian Lasserus, Martin Schnedlitz, Florian Lackner, and Wolfgang E. Ernst in *The Journal of Chemical Physics* **149**, 024305 (2018).
https://doi.org/10.1063/1.5026480

(3) "Modelling electron beam induced dynamics in metallic nanoclusters" by Daniel Knez, Martin Schnedlitz, Maximilian Lasserus, **Alexander Schiffmann**, Wolfgang E. Ernst, and Ferdinand Hofer in *Ultramicroscopy* **192**, 69-79 (2018).
https://doi.org/10.1016/j.ultramic.2018.05.007

(4) "Ultra-thin h-BN substrates for nanoscale plasmon spectroscopy" by **Alexander Schiffmann**, Daniel Knez, Florian Lackner, Maximilian Lasserus, Roman Messner, Martin Schnedlitz, Gerald Kothleitner, Ferdinand Hofer, and Wolfgang E. Ernst in *Journal of Applied Physics* **125**, 023104 (2019).
https://doi.org/10.1063/1.5064529

(5) "Helium nanodroplet assisted synthesis of bimetallic Ag@Au nanoparticles with tunable localized surface plasmon resonance" by Florian Lackner, **Alexander Schiffmann**, Maximillian Lasserus, Roman Messner, Martin Schnedlitz, Harald Fitzek, Peter Pölt, Daniel Knez, Gerald Kothleitner, and Wolfgang E. Ernst in *The European Physical Journal D* **73**, 104 (2019).
https://doi.org/10.1140/epjd/e2019-90696-8

(6) "Effects of the Core Location on the Structural Stability of Ni–Au Core-Shell Nanoparticles" by Martin Schnedlitz, Ricardo Fernandez-Perea, Daniel Knez, Maximilian Lasserus, **Alexander Schiffmann**, Ferdinand Hofer, Andreas W. Hauser, Maria Pilar de Lara-Castells, and Wolfgang E. Ernst in *The Journal of Physical Chemistry C* **123 (32)**, 20037-20043 (2019). https://doi.org/10.1021/acs.jpcc.9b05765

(7) "Ultrashort XUV pulse absorption spectroscopy of partially oxidized cobalt nanoparticles" by **Alexander Schiffmann**, Benjamin W. Toulsen, Daniel Knez, Roman Messner, Martin Schnedlitz, Maximilian Lasserus, Ferdinand Hofer, Wolfgang E. Ernst, Oliver Gessner, and Florian Lackner in *Journal of Applied Physics* **127**, 184303 (2020). https://doi.org/10.1063/5.0004582

(8) "Helium Droplet Assisted Synthesis of Plasmonic Ag@ZnO Core@shell Nanoparticles" by **Alexander Schiffmann**, Thomas Jauk, Daniel Knez, Harald Fitzek, Ferdinand Hofer, Florian Lackner, and Wolfgang E. Ernst in *Nano Research* **13**, 2979–2986 (2020). https://doi.org/10.1007/s12274-020-2961-z

The author also presented his work on several occasions during international conferences. Those contributions are listed below in chronological order.

(C1) "Synthesis and Analysis of Core-Shell Nanoparticles Grown Inside Superfluid Helium Droplets" [Presentation]. 7th FOCUS PEEM Workshop, Hünstetten-Kesselbach, Germany (2017, June 21).

(C2) "Synthesis and Analysis of Core-Shell Nanoparticles Grown Inside Superfluid Helium Droplets" [Poster Session]. 7th FOCUS PEEM Workshop, Hünstetten-Kesselbach, Germany (2017, June 21).

(C3) "Temperature Studies of Ni@Au and Co@Au Core@Shell Systems on the Nanoscale" [Poster Session]. EU Cost Action MOLIM Workshop, Graz, Austria (2018, February 6).

(C4) "Ultra-thin h-BN films employed as STEM substrates for nanoscale plasmon spectroscopy" [Presentation]. European Conference on Surface Science (ECOSS) 34, Aarhus, Denmark (2018, August 30).

(C5) "Plasmon spectroscopy of metallic nanoparticles on ultra-thin h-BN films" [Presentation]. 68th Annual Meeting of the Austrian Physical Society, Graz, Austria (2018, September 11).

Contents

List of Figures

List of Tables

1 Introduction

1.1 Motivation - Nanoparticle synthesis and analysis

There is one main motive for almost every kind of research and entrepreneurship: curiosity. It gives us all the necessary motivation and probably is the most human trait of all. Curiosity powered the rise of the human species right from the beginning. There were always people, who were not satisfied with the current state, who were sure that things could be changed and improved. This is as true for modern societies as it was for the hunters and gatherers of old. Curiosity prevailed as an incitement towards any exploration of the new and unknown. Especially in fundamental research it is of utter importance that we want to shed light on unknown things and that we are driven by our own curiosity.

Nano-science excited the curiosity of scientist constantly over the past decades, since it is the realm where familiar concepts about materials and matter have to be reconsidered. Today, it is not a scientific niche anymore, structures and particles on the nanoscale are a main field in research and are present in everyday life. Therefore, it is more important than ever to learn about properties of nanomaterials. The Institute of Experimental Physics at Graz University of Technology acquired expertise in the production and analysis of metallic nanoparticles with diameters below 10 nm since the helium droplet synthesis laboratory was established in the year 2011. In a well controlled process, nanoparticles of varying shapes and sizes can be synthesized within superfluid helium droplets. This scheme features several advantages in comparison to e.g. wet chemical fabrication routes. Throughout the whole process, only the high purity helium and the metals are present and there are no further additives like solvents or surfactants involved. Also, there is no need for the development of new synthesis routes for every employed material. The helium droplet approach is, in principle, working with almost every metal. Furthermore, the shape and size of the synthesized nanoparticles can be readily adjusted over a wide range and the tailoring of core@shell particles, composed of two different metals, is a straight forward process. Those are good reasons why the helium droplet synthesis approach should be of interest for a wide audience in modern-day nanoparticle research.

In the past, the main research goal was to gain basic knowledge about the process, its parameters, and the quality of the formed nanoparticles. During that time, mostly Ag and Au species were produced and analyzed by means of scan-

ning transmission electron microscopy (STEM). In recent years, however, the focus shifted from pure fundamental research aspects towards possible applications. To this end, the portfolio of employed analytical methods was greatly expanded by the addition of surface enhanced Raman spectroscopy (SERS), electron energy loss spectroscopy (EELS), XUV absorption spectroscopy, and photoemision electron microscopy (PEEM). At the same time, the selection of materials used for nanoparticle formation was broadened by a stepwise exchange of the easy to handle noble metals Ag and Au with e.g. Fe, Ni, Co, or Zn.

The present thesis focuses mostly on the tailoring of sub 10 nm plasmonic nanoparticles and the implementation of the above mentioned measurement methods. The concept of coupling light to nanostructures and nanoparticles via their plasmonic properties received increased attention, since there is a wide field of possible applications opening up, especially in sensorics. Therefore, both the fabrication and the reliable investigation of plasmonic nanoparticles were explicit goals of the conducted experiments. For the investigation of Ag@Au core@shell nanorods by means of EELS an ultra-thin hexagonal boron nitride substrate was developed and used in plasmon spectroscopy to improve the obtained signal quality [1]. In a further study on Ag@Au core@shell nanoparticles the localized surface plasmon resonance was tuned by a variation of the material ratio. By depositing those particles samples with a high surface coverage were produced for the first time to utilize them as substrates for SERS, which is a well established technique for sensor applications [2]. As a next step the Au shell was replaced by ZnO with the formation of plasmonically active Ag@ZnO nanoparticles [3]. Measurements were conducted in the newly established PEEM laboratory and comprised ultraviolet photoelectron spectroscopy (UPS) and two-photon photoemission (2PPE) spectroscopy. Besides the plasmonic nanoparticles, CoO nanowires were investigated with a particularly interesting method: pulsed XUV absorption spectroscopy [4]. The successful measurement was the first one conducted on a comparable nanoparticle substrate.

In related articles further investigations were carried out on the influence the electron beam in STEM has on small metallic nanoparticles [5], or on nanoscale alloying processes in the Ag-Au system [6]. Furthermore, spectroscopy of atoms and oligomers directly in the helium droplets is still an important branch of research. Transitions in Au were investigated by resonant two-photon ionization spectroscopy [7]. In another exemplary work, measurements on the core location in Ni@Au core@shell nanoparticles were conducted and compared to molecular dynamics simulations to closely investigate the relevant diffusion processes [8].

With all those interesting research possibilities at hand, there is a good chance

that curiosity will also be excited in a future generation of scientists and PhD students engaged with the helium droplet synthesis approach.

1.2 Thesis Structure

This doctoral thesis is organized in a cumulative way and centered around the already published work of the author. Those peer reviewed papers are reprinted with permission of the respective journals and are presented in Chapters 3 - 6. At the beginning of the according chapters the contribution of all co-authors is disclosed in detail. To provide context for the four publications, an elaborate introduction into the fundamentals of the employed experimental setups is given in Chapter 2. The conjunctive topic of all four papers is the fabrication of tailored nanoparticles with the helium droplet synthesis approach and the subsequent analysis of those nanoparticles with a varying set of spectroscopic methods. Detailed information on the relevance and the spectrum of possible applications for the different nanoparticle types is given in the introductions of the respective chapters.

Chapter 3 contains information about the synthesis of plasmonically active Ag nanoparticles and Ag@Au core@shell nanorods in the sub 20 nm size regime, which were deposited on a specially prepared ultra-thin hexagonal boron nitride (h-BN) substrate [1]. In close cooperation with the Institute of Electron Microscopy and Nanoanalysis at Graz University of Technology that substrate was chosen because of its excellent properties for electron energy loss spectroscopy (EELS). The nanoparticles were investigated with scanning transmission electron microscopy (STEM), EELS, and energy dispersive X-ray spectroscopy (EDS), confirming the advantages of the h-BN substrate. Furthermore, maps of the localized surface plasmon resonance (LSPR) of the nanoparticles were obtained.

In the second paper presented in Chapter 4, the Ag@Au core@shell system was further investigated regarding its plasmonic properties [2]. By varying the Ag:Au ratio of the nanoparticles the LSPR becomes tunable in between the resonances of pure Ag and Au. For this experiment, besides STEM, a new set of analytical methods was used. After deposition of the nanoparticles on fused silica slides, the plasmon resonance was first measured by means of UV/vis absorption spectroscopy. In a second step those nanostructures were functionalized with 4-methylbenzenethiol (4-MBT) molecules and analyzed by surface-enhanced Raman spectroscopy (SERS).

In a next step, the range of materials for nanoparticle synthesis was further expanded beyond noble metals. Preliminary experiments were conducted with various metals and their oxides. For the publication presented in Chapter 5, Ag@ZnO core@shell nanoparticles were synthesized and investigated [3]. Zinc oxide is not only a very popular material in a wide range of scientific fields, but also turned out to form very uniform shells in our synthesis process. This is proven for spherically shaped particles and elongated wire-like structures by STEM imaging. The newly established energy-filtered photoemission electron microscope (EF-PEEM) facility was used to obtain further information about the oxidation state of the ZnO shell by ultraviolet photoelectron spectroscopy (UPS). Furthermore, the plasmonic properties of the Ag cores were investigated by two-photon photoelectron spectroscopy (2PPE), also employing the EF-PEEM facility and the second harmonic of a Ti:Sapphire laser system.

Finally, with nanowires made of cobalt another metal and its oxide were investigated in the publication presented in Chapter 6 [4]. Nanowires were synthesized employing the helium droplet approach and deposited on special Si_3N_4 substrates. They were characterized by STEM and EDS, including an analysis of their oxidation state. In cooperation with the Lawrence Berkeley National Laboratory in California a high-order harmonic generation (HHG) based laser source was used for conducting table-top ultrafast XUV spectroscopy. The experiment confirmed the feasibility of this measurement scheme for nanoparticles with sub-monolayer surface coverage by yielding spectra with assignable absorption features.

2 Fundamental Concepts and Experimental Methods

Within this chapter the experimental methods, which form the basis of this work, are presented and explained. An elaborated overview on the synthesis approach and all the employed analytical methods and setups is given. The author gained experience concerning these methods, but in most cases measurements were conducted together with experts in the respective fields to ensure that the obtained results are of high quality and fulfill the scientific standard. Exceptions are the nanoparticle synthesis and the field of photoemission electron microscopy, where the author built his own expertise. However, discussions with co-workers and colleagues at the institute happened at all stages of the experiments and were always appreciated and helpful.

2.1 Helium droplet synthesis approach

The helium droplet synthesis apparatus is the central experiment for the work present in this thesis. All of the publications revolve around the nanoparticles produced with the setup in Cluster Laboratory III at the Institute of Experimental Physics. In the following chapters the basic concepts of the helium droplets, the synthesis approach, the apparatus, and the surrounding laboratory facility will be explained. In 2011 the basic structure of the experiment was transferred from Bochum to Graz and in the following construction phase, lasting for about two years, it was adapted and rebuilt for its new purpose. This was done by the group of Prof. Wolfgang E. Ernst, namely by the former PhD students Alexander Volk [9] and Philipp Thaler [10] with support from the master student Johannes Steurer [11] and several bachelor students. More details and elaborated insights into the build-up process can be found in their respective theses. Moreover, they have authored a detailed manual on the handling of the apparatus and the laboratory equipment. The manual is attached to their PhD theses [9, 10] and served as a basic guideline for following generations of scientists. Also Martin Schnedlitz, Maximilian Lasserus, and Roman Messner need to be mentioned in connection with Cluster Laboratory III. All three worked, together with the author, at the apparatus during their master theses and subsequent PhD theses. Though everyone was engaged with slightly different topics, they formed a team that further evolved the helium droplet synthesis approach and opened up different fundamental research fields with the synthesized nanoparticles.

2.1.1 Helium and helium droplets

The first evidence for the existence of helium was observed in 1868, when a bright yellow spectral line at 587.49 nm was found in the solar spectrum by several researchers. The credit for this discovery was given to Jules Jansen and Norman Lockyer and the latter named the new element after the Greek word for sun. Since 1895, when William Ramsay first isolated helium on earth, the noble gas was thoroughly investigated and found to possess some surprising properties. There are two stable isotopes of helium: ^{3}He and ^{4}He. Since the ^{3}He isotope is very rare, the experiments covered in this work were conducted with ^{4}He. The use of helium or He in this thesis is therefore always related to ^{4}He. Because of its weak dispersion forces, He exhibits the lowest boiling point of all elements with $T_B = 4.2\,\mathrm{K}$ and remains liquid down to 0 K when kept at atmospheric pressure [12]. Besides that, the phase diagram of He, depicted in Fig. 1, shows another peculiarity: the λ-point at 2.17 K [13]. Upon being cooled below this temperature He enters the so-called He II phase, where it drastically changes its properties and becomes superfluid. In this state, discovered in 1938 [14, 15], the viscosity of He is close to zero and its specific heat conductivity reaches extraordinarily high values [13].

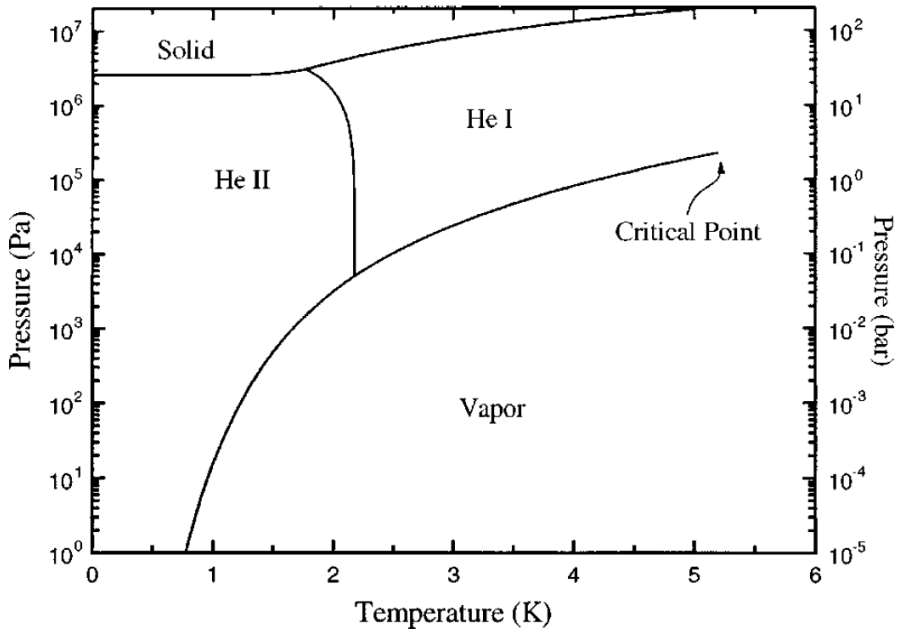

Figure 1: The logarithmic phase diagram for ^{4}He shows the so-called λ transition between the liquid He I and He II phase. Reprinted from Ref. [13], with the permission of AIP Publishing.

Because of its intriguing properties, He played an important role in fundamental research. Becker et al. managed to produce the first condensed He beam

in a free jet expansion in ultra-high vacuum (UHV) [16] and over the years the understanding of He droplets (He_N) was increased as their properties were thoroughly investigated. An important further step was the finding that He_N are able to pick up almost all atomic and molecular dopants upon contact. Hydrogen, alkali metals, and several alkaline earth metals are exceptions, they reside on the droplet surface instead of being immersed into the volume [17]. Pickup of foreign species is essential for the application of helium droplets in spectroscopy and nanoparticle synthesis, as will be discussed within the next chapter.

2.1.2 Helium droplet synthesis apparatus

In the following, Cluster Laboratory III and the He_N apparatus are introduced in more detail. Also the fundamental concepts concerning beam generation and nanoparticle formation are explained within the context of the experimental realization. Details on the laboratory infrastructure may be found in Refs. [9,10]. The apparatus is mounted on a massive steel framework and accessible from all sites. All vacuum pumps are controlled centrally and an electronic fail-safe system is in place to prevent damages in case of power outages or problems with the cooling water supply. The overview schematic in Fig. 2 gives an impression of the three chamber setup and includes the relevant features of the apparatus [10].

In the source chamber of the apparatus the He_N beam is created by supersonic expansion of high purity (99.9999%) helium through a cooled nozzle into the high vacuum of the chamber ($\approx 10^{-5}$ mbar). The gaseous helium is kept under a stagnation pressure of $p_0 = 20 - 60$ bar and is directly supplied to the nozzle, a platinum microscope aperture with a 5 μm diameter, situated on a copper block. The end of the supply pipe and the copper block with the nozzle are cooled down to $T_0 = 4 - 10$ K. Cooling is achieved with a closed cycle refrigeration unit (*Sumitomo* RDK-408D2) and the temperature is measured with a silicon diode temperature sensor (*Lake Shore Cryotronics Inc.*, model DT-670B1-BO) that directly feeds the measured value to an electronic control system (*Eurotherm* 3500). With this feedback loop a power resistor is regulated to heat against the refrigeration unit, which would otherwise cool the nozzle to 3.8 K. The well adjusted system actively stabilizes the temperature with an accuracy of ± 0.02 K during the experiments [9]. Temperature stability is important for controlling the He_N size. As shown in Fig. 3, the mean number of helium atoms in a single droplet and thus its diameter depends directly upon T_0 and p_0 [18]. By controlling the two parameters a wide range of droplet sizes is accessible.

For discussing the three depicted regimes of operation in Fig. 3, the expansion

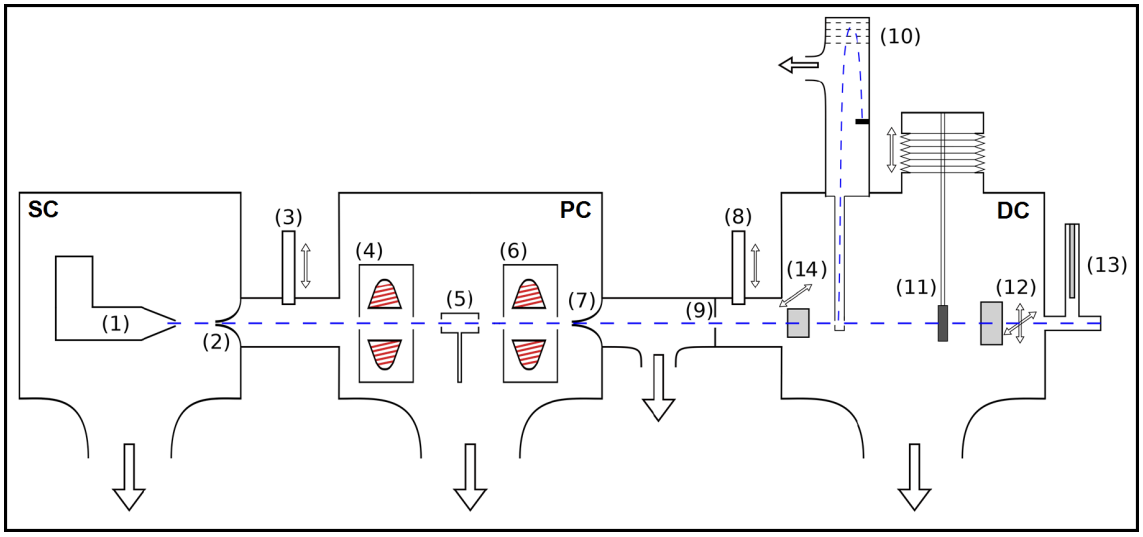

Figure 2: Schematic of the He droplet apparatus consisting of source chamber (SC), pickup chamber (PC), and diagnostics chamber (DC), separable by gate valves (3) and (8). The He_N beam is produced by expansion through a cooled nozzle (1) and collimated by skimmers (2) and (7) and an aperture (9). Doping is enabled by a gas pickup cell (5) and the resistively heated evaporation cells (4) and (6). For in-situ diagnostics a time-of-flight mass spectrometer (10), a quartz crystal microbalance (12), and a quadrupole mass spectrometer (13) are available. Substrates for deposition can be inserted via the fixed holding system (11) or the UHV transfer system (14). Modified from Ref. [10].

process of the helium into vacuum will be explained according to Refs. [17,18]. During the expansion the gas flow reaches supersonic speed, if the relation of gas pressure to vacuum pressure is high enough. In this quasi adiabatic process the internal energy of the gas is shifted towards translational kinetic energy and the beam becomes strongly directional with a very narrow velocity distribution. Under "subcritical" conditions, corresponding to the condensation of gas regime, the collisional cooling of the helium precedes the clustering. Once clusters were formed, they are cooled down further to 0.37 K by evaporative cooling. Therefore, for nozzle temperatures above $\approx$ 10 K in Fig. 3 the He_N growth is dominated by atomic collisions during the gas expansion. For nozzle temperatures below $\approx$ 4 K, in the "supercritical" regime of the Rayleigh break-up, a jet of liquid helium expands through the nozzle and breaks up into larger droplets. As a simplified analogon, a stream of water upon leaving the faucet shows similar behavior. Nozzle temperatures in between lie in the fragmentation of liquid regime, where the liquefied share is fragmented by the gaseous part of the helium. In all three regimes the formed He_N are evaporatively cooled to the above mentioned 0.37 K. The temperature was experimentally confirmed from

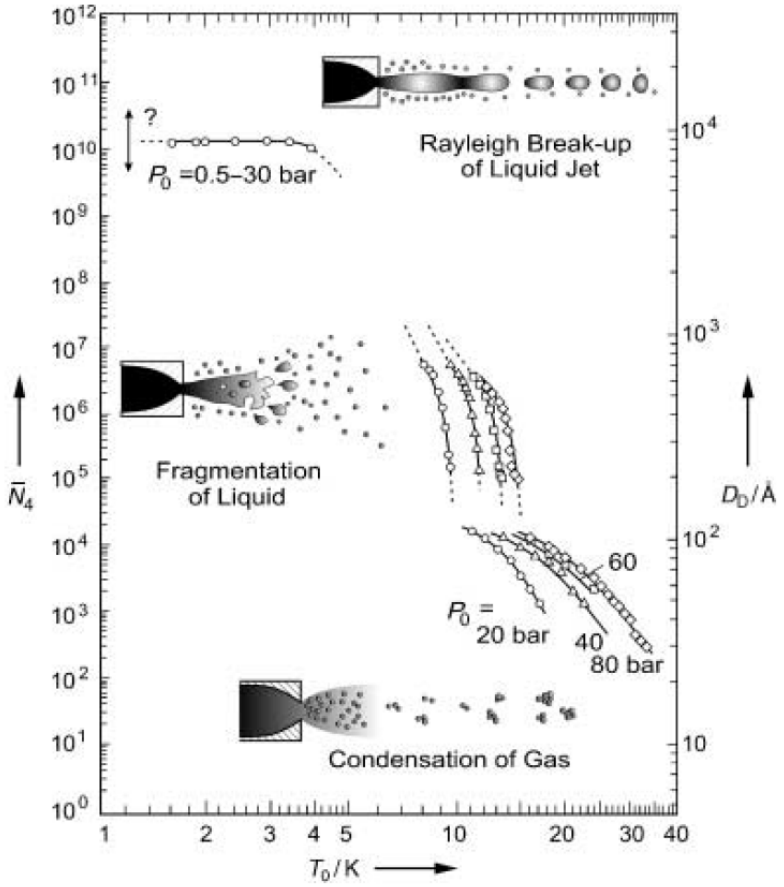

Figure 3: The He_N size, represented by the mean number of ^{4}He atoms $\bar{N}_4$ and the liquid-droplet diameter D_D, as a function of the the nozzle temperature T_0 and the stagnation pressure p_0. The three regimes of operation, namely condensation of gas, fragmentation of liquid, and Rayleigh break-up, are temperature dependent and schematically depicted close to the according measurement data. Reprinted from Ref. [18], with permission of John Wiley & Sons, Inc.

spectra of immersed SF_6 molecules [19] and even the surface temperature agrees with this value as measured from Zeeman spectra of alkali dimers [20]. The droplets reach the superfluid He II state as long as the number of clustered He atoms exceeds $\approx$ 60 [21]. Typical beam velocities of He_N lie between 200 and 400 m/s.

For most of the experiments discussed within this thesis a parameter set of 20 bar and 6 - 8 K was used, working in the fragmentation of liquid regime with He_N diameters around 100 nm. Only for the synthesis of nanowires the Rayleigh break-up regime was reached, with 20 bar and 4 - 5.4 K, yielding the largest droplet sizes with about 1 μm in diameter. The He_N size naturally limits the overall amount of dopant atoms that are picked up and the nanoparticle

growth, as will be discussed in more detail later on.

A further feature that influences the particle growth process, especially in larger droplets, is the occurrence of vortices within the He_N. The concept will be outlined according to Ref. [22]. Angular momentum taken up by the droplets upon expansion through the nozzle cannot be transferred into a rotation once they are cooled below 2.17 K because of the insignificant viscosity in the He II phase. Still, the conservation of angular momentum is essential and, thus, vortices within the droplets are generated. In a superfluid medium the vortices are quantized by quanta of circulation. A vortex usually carries one quantum of circulation, but also the sharing of a quantum by two vortices is possible. A transfer of large angular momenta to the superfluid leads to the formation of multiple vortices, which preferably order in a hexagonal array. An important property is the pressure gradient surrounding a vortex that is directed towards its core [23]. Atoms or particles immersed in the superfluid are captured and move towards the vortex core. The impact on nanoparticle growth will be discussed in the following paragraphs.

After its generation in the source chamber, the He_N beam is directed through a skimmer with a diameter of 0.4 mm into the pickup chamber. Here, only a small portion in the center of the beam is allowed to pass. The rest of the helium stays in the source chamber and is pumped out a by large oil diffusion pump with a throughput of 12 000 l/s. The dimension of the pump allows to keep the pressure steady in the high vacuum range despite the constant flow of pressurized helium. The propagation direction and angle of the He_N beam can be adjusted with a tripod that holds the cooled nozzle setup.

In the pickup chamber, kept at a pressure of $\approx 10^{-7}$ mbar, the He_N are doped by passing through three especially designed pickup cells. As shown in Fig. 2, there are two evaporation cells and a gas pickup cell in between. The evaporation cells consist of resistively heated tungsten baskets coated with aluminum oxide (*Ted Pella Inc.*, Prod. No. 84-27), situated on water-cooled base-plates and covered with water-cooled copper shields. Each cell is connected to a power supply (EA-PS 9080-100) and individually controlled. The temperature is determined indirectly by an in-situ measurement of the tungsten baskets resistivity, which has a known temperature dependence. High purity metals are filled into the baskets and heated until the partial vapor pressure in the cells is high enough for pickup to happen, usually starting at $\approx 5 \times 10^{-5}$ mbar. As mentioned above, metal atoms are picked up and immersed in the He_N upon contact.

The amount of doped material can be controlled by the temperature of the

evaporation cell and the He_N size. For small He_N ($T_0 > 10\,K$) and low doping rates, small clusters, oligomers, dimers, or even single atoms are formed [7]. Once within the droplet, the dopants are cooled down to the helium temperature, but otherwise the interaction with helium is negligible. Therefore, the He_N serve as an ideal matrix for spectroscopic investigations and are already well established in this role [17,18,24].

Due to the superfluidity of the He_N, the dopant atoms can move unobstructed through the droplets and accumulate to clusters upon statistical collisions [25,26]. The cluster growth starts with multiple centers before they further agglomerate and grow until they form nanoparticles with several hundreds or thousands of atoms. As droplet size and dopant vapor pressure are increased nanoparticle growth is supported. In the apparatus the final nanoparticle size cannot be measured directly, but by capitalizing on the fact that He is evaporated from the droplets upon the cooling of dopant atoms. About 1 600 He atoms are lost per 1 eV of dissipated energy [18]. Therefore, the overall decline in He measured at the quadrupole mass spectrometer (QMS) at the end of the beam path in the diagnostics chamber can be linked to the immersed amount of dopant atoms and the nanoparticle size [27]. For a skilled operator the attenuation of the He signal is the most important parameter for a controlled and reproducible nanoparticle synthesis. Note that a rather broad size distribution of the fabricated nanoparticles is inherent to the approach because of the lognormal distribution of the droplet sizes [28].

As indicated above, the nanoparticle growth in larger He_N produced in the Rayleigh break-up regime is strongly guided by vortices within the droplets. Upon pickup the atoms and clusters accumulate along the cores of the vortices. If enough dopant metal is supplied, elongated nanowires are formed with lengths up to several hundred nm and high aspect ratios [27,29–31].

For nanoparticle and nanowires of any size and shape it is readily possible with the helium droplet approach to form core@shell structures with two different metals. The first and the second evaporation cell are filled with the respective core and shell materials. Upon passing through the pickup cells the He_N are subsequently doped with the metals. Once the beam reaches the second cell the cores have already formed and the shell atoms attach to the existing particles [1–3,6]. Compared to other synthesis techniques the approach is very versatile. Moreover, switching between the different formation modes is facile and takes only minutes once the beam is aligned and the evaporation cells are prepared.

The additionally available gas pickup cell consists of a steel cylinder with a small hole on each end to let the He_N pass through. A gas can be supplied over an attached line, which is connected to a separately pumped reservoir on the

outside. In principle, materials with high vapor pressure, e.g. organic molecules, can be doped into the He_N for spectroscopic measurements or to attach them to metallic nanoparticles.

The diagnostics chamber, at a base pressure of $\approx 5 \times 10^{-10}$ mbar is the last section of the apparatus reached by the He_N beam. At this stage the nanoparticles are already formed and still immersed within the superfluid droplets. The diagnostics chamber contains a set of analytical tools for the conduction of in-situ measurements on the He_N and the nanoparticles. The above mentioned QMS is almost exclusively used for monitoring the He attenuation resulting from particle growth.

The quartz crystal microbalance (QMB) can be moved into the beam path and is utilized for determining the mass deposition rate. This is especially important for the preparation of substrates with high surface coverages. Because of the low mass flow in the range between 10^{-5} and 10^{-3} $\mu g/(cm^2 s)$ typically reached by the helium droplet approach, the QMB needs to be very sensitive. It monitors the resonance frequency f_0 of an oscillating quartz crystal, which undergoes a change of Δf upon an applied change in mass Δm. In the Sauerbrey equation in Eq. 1 the correlation is stated, containing the piezoelectrically active area A, the density of the quartz ρ_q, and the shear modulus of the quartz μ_q [32]:

$$\Delta f = -\frac{2 \cdot f_0^2}{A \cdot \sqrt{\rho_q \cdot \mu_q}} \cdot \Delta m \tag{1}$$

To allow for high resolution measurements of the mass deposition the QMB is kept at a constant temperature of 35°C with a directly attached small light bulb. The temperature is measured with a thermocouple and stabilized by an electronic feedback loop.

The final step in the production of nanoparticles is the deposition onto a suitable substrate. Therefore, the substrate needs to be positioned in the He_N beam path. A fixed holding system, that can be rotated and tilted for positioning, is available right in front of the QMB. It is optimized for holding circular amorphous carbon substrates with a diameter of 3 mm, used primarily for transmission electron microscopy. It has the disadvantage that a big flange on the side of the chamber has to be unscrewed and opened for every sample transfer. Afterwards, the chamber also needs to be baked to reach the desired base pressure again. As a major improvement in sample handling the UHV transfer system, described in the following Chapter 2.1.3, was established.

Regarding the deposition process, the He_N provide another beneficial side effect by cushioning the impact of the nanoparticles on the substrate surface in a so-called soft landing process [33–35]. Upon termination of the beam on the substrate the droplets hit the surface with velocities of up to 400 m/s, disaggregating the He_N and leaving the metallic nanoparticles undamaged. The cushioning effect also contributes to keep ultra-thin substrates, like amorphous carbon, hexagonal boron nitride, or Si_3N_4 with a thickness of only about 10 nm, intact [1, 3]. Besides the mentioned thin substrates employed for transmission electron microscopy or XUV absorption spectroscopy, also other materials like p-type Si, Au coated Si, fused silica, or glass slides with indium tin oxide (ITO) coating were used to terminate the beam and receive the nanoparticles.

2.1.3 UHV sample transfer system

The UVH sample transfer system is an essential part of the experimental setup and was upgraded several times to function with various kinds of substrates. It mainly consists of a vacuum suitcase (*Ferrovac GmbH*, NexGeneration UHV Suitcase) that allows for storage and transport of samples under full UHV conditions. The suitcase volume is passively pumped by a non evaporable getter (NEG) pump keeping the pressure in the low 10^{-10} mbar region. For regeneration the system needs to be baked regularly, while it is pumped with an external turbomolecular pump. On one side a DN40CF flange is sealed with a gate valve, which can be attached to any suitable vacuum chamber. A 700 mm wobble stick with a pincer, controlled by magnetic coupling from the outside, can be used to introduce substrates into the He_N beam path. It is not flanged directly to the diagnostics chamber, but to a transfer chamber that can be vented and pumped separately without breaking the vacuum in the apparatus. Bigger substrates like fused silica slides can be prepared in the transfer chamber and then picked up with the wobble stick for deposition. Sample holding systems were built to allow for storage of several electron microscopy substrates at once and subsequent deposition onto them.

The suitcase includes a storage shelf for up to three small sample plates used in the NanoESCA photoemission electron microscope, cf. Chapter 2.6. This allows for the UHV transfer of prepared nanoparticle samples directly to the NanoESCA, where also a small and independently pumped transfer volume is used to connect the suitcase. While transported, the NEG pump runs on a battery for up to 48 h. This allows, in principle, for the transfer of samples to external laboratories and partners under clean vacuum conditions.

With the implementation and stepwise upgrade of the UHV transfer system

sample handling was tremendously simplified and the experimental efficiency was boosted. Several samples can be prepared at once and the small transfer volume can be pumped and baked over night. Pumping and baking of the whole diagnostics chamber, on the other hand, can take up to two days depending on the degree of contamination.

2.2 Electron microscopy

For conducting high quality research on nanoparticles it is essential to have measurement techniques at hand which can provide information down in the nm range and below. Though, there is a lot of methods to gain information, it is favorable to obtain images of the particles. This way it is possible to make assumptions on their size, shape, and even their morphology. Microscopic imaging methods are thus an important part of research on the nanoscale. The author had the opportunity to closely work together with experts at the Institute of Electron Microscopy and Nanoanalysis (FELMI) at Graz University of Technology. This experimental cooperation and its results form the backbone of the work on different nanoparticle systems.

Advances in microscopic imaging methods were always big steps for science as a whole. It became possible to verify theoretical predictions and also find completely new insights by looking closer and closer into matter itself. Thereby, the Abbe diffraction limit, cf. Eq. 2, gives a minimum for the resolvable distance d with the wavelength λ, the refractive index of the medium n, and the half-angle θ [36].

$$d = \frac{\lambda}{2 \cdot n \cdot \sin(\theta)} \tag{2}$$

A real leap in the technological evolution of microscopy was the development of electron microscopes back in the 1920s and 1930s [37]. Up to that point the resolution in light microscopy was limited in the range of 100 nm. By using accelerated electrons instead of photons the resolution was, in principle, suddenly reduced down into the sub nm regime. This is due to the very short de Broglie wavelength λ_{dB} of the electrons. λ_{dB} can be derived via Eq. 3 with the Planck constant h, the mass of the electron m_e, and the acceleration voltage U [38].

$$\lambda_{dB} = \frac{h}{\sqrt{2 \cdot m_e \cdot U}} \tag{3}$$

There are instrument related limitations like the mechanical stability of the setup, the quality of the electron source, or aberrations of the employed electromagnetic

lens systems, but in state of art transmission electron microscopes it is already possible to investigate nanoparticles in quasi-atomic resolution.

A vital part of every electron microscope is the electron source. In a standard setup the source is a hot cathode, made of a tungsten filament or a lanthanum hexaboride crystal, which is heated and emits the electrons. In more sophisticated setups a field emission gun (FEG) is employed for cold emission, where electrons are ripped from a fine tungsten tip by means of applied high voltages. This method yields a narrower but less intense electron beam. A combination of both types is the heated FEG, known as Schottky emitter, which uses zirconium oxide as source material and has the advantage of higher beam intensities. The electron beam, at typical energies of several 10 keV to several 100 keV, then passes through a set of electromagnetic condenser lenses and is, thereby, focused to a spot size in the nm range or below.

2.2.1 Scanning electron microscopy

In a scanning electron microscope (SEM) the focused primary electron beam is moved over the sample surface by scanning coils or deflector plates, allowing for a deflection of the beam in both the x and y direction. During the scan the beam stops in between for short times. The information gathered at every stop corresponds to one pixel in the final SEM image that is formed by scanning a rectangular area line by line. Upon impact the primary electrons interact with the sample material. They are repeatedly scattered within the pear-shaped interaction volume up to several μm deep into the specimen. Thereby, they can be elastically scattered and leave the sample again as so-called backscattered electrons (BSE) or they exchange energy with the sample by undergoing inelastic scattering processes, resulting in the emission of secondary electrons (SE) and photons.

There are different detection methods for obtaining information from scattered electrons. BSE still posses high energies after elastic scattering with the specimen atoms and escape the sample from depths up to several 100 nm [39]. They are most frequently scattered back under wide angles close to 180°, almost parallel to the primary beam. Therefore, the semiconductor detectors, which are normally used, are positioned in a toroidal arrangement around the primary electron beam straight above the specimen. The images acquired by BSE detection are used to gain information about the composition of the sample. Elements with higher atomic numbers appear brighter because they backscatter more electrons than light atoms [39]. For obtaining images with surface contrast, on the other hand, SE are used. SE are ejected upon inelastic scattering with the primary electrons, which are lower in energy and mostly originate from depths of only a

few nanometers below the sample surface [39]. Because of the shallow escape depth, kinks and edges on the sample surface appear brighter and give the image a strong 3D character. For detection an Everhart-Thornley detector [40] is used. A positively biased collector grid attracts the SE. Then they are further accelerated onto a scintillator and the emitted photons finally produce a signal in a photomultiplier. The Everhart-Thornley detector is usually positioned only on one side of the sample. Besides the electron detection, there is also the possibility to use the characteristic X-ray signature of elements to find out about the chemical composition of the sample. The high energetic photons are a byproduct of the interaction of the primary electrons with the sample and can be detected by an X-ray detector (cf. Chapter 2.2.3).

Modern SEM systems reach resolutions down in the nm range. This is still not good enough to image details from the nanoparticles produced by the helium droplet synthesis approach, where the whole particle is just a few nm in diameter. Nonetheless, it is sufficient to obtain overview images, which can be used to roughly estimate the surface coverage or even the particle sizes and shapes, especially for larger wire-like nanoparticles. A main constraint for the use of an SEM is the need of a conductive substrate to avoid charging effects through accumulated electrons on the surface. If the substrate is conductive and the nanoparticle surface coverage is below a monolayer, the particles themselves can be non conductive. This was the case for the experiment presented in Chapter 5, where SEM was used to obtain images from Ag@ZnO core@shell nanoparticles and nanowires on an indium tin oxide (ITO) surface [1]. Part of the SEM image of a nanowire sample taken during this measurement is shown in Fig. 4. The inlens SE detector of a *Zeiss* Sigma 300 VP SEM operated at an acceleration voltage of 15 kV and a working distance of 2.3 mm was used to obtain this image.

As discussed above, the resolution is not good enough to make out details in Fig. 4, but the overall shape and size of the wire-like nanoparticles can be estimated and deduced from such SEM images. For a thorough evaluation it is important to take the artificial broadening due to the electron interaction volume into account. The secondary electrons, which are detected and form the image, originate from an expanded volume around the impact area of the incoming primary electron beam. SEM, as a complementary imaging technique, can be especially useful, if the specimen is not suitable for scanning transmission electron microscopy (cf. Chapter 2.2.2), as it is the case for the above mentioned sample where the ITO film is situated on a glass slide.

To demonstrate the capabilities for smaller particles, Fig. 5 shows part of a SEM image of sub-10 nm Ag and Au nanoparticles on a silicon nitride support. Again, the nanoparticles appear artificially enlarged, but the image allows for a

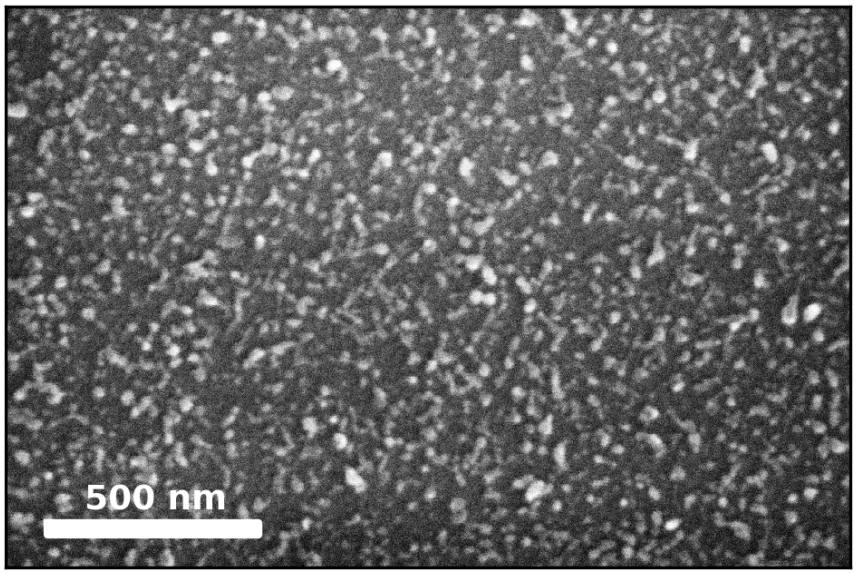

Figure 4: SEM image of Ag@ZnO nanowires on an indium tin oxide (ITO) surface. The elongated wire-like structures are clearly visible and a rough characterization of shape and size is possible. The thickened agglomerations of material form when nanowires are deposited on top of each other because of the statistical nature of the deposition process.

good estimation of the overall number and distribution of the deposited particles. The small bright spots can be well distinguished from the darker background.

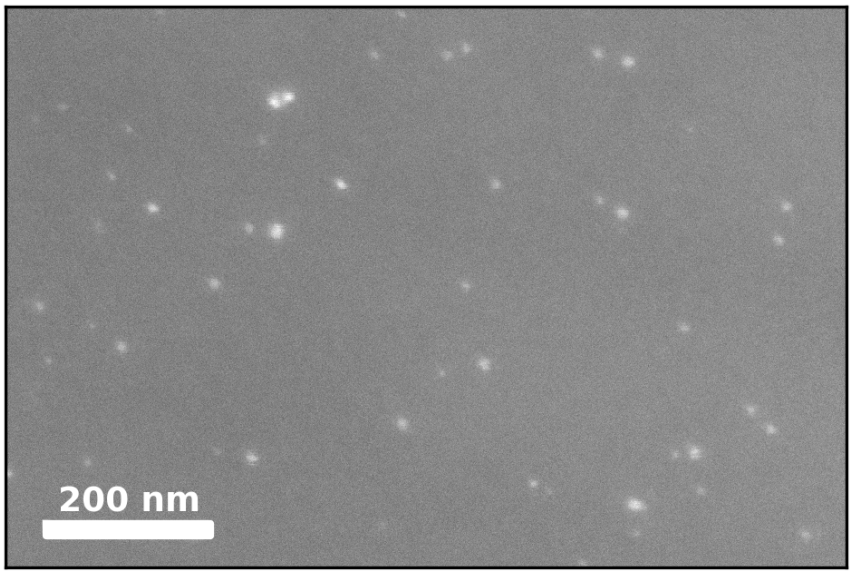

Figure 5: Detail from an SEM image of Ag and Au nanoparticles with a low coverage on a silicon nitride support. Individual particles give a bright signal and can be clearly distinguished from the background.

Overall, SEM is a good solution for doing overview characterization of nanoparticle samples, especially, because images can be acquired comparably fast. This method requires less effort for sample preparation compared to transmission electron microscopy, which will be explained in the next chapter.

2.2.2 Scanning transmission electron microscopy

Scanning transmission electron microscopy (STEM) has several advantages compared with the above mentioned SEM, when approaching the nm regime. STEM has become a standard method for the analysis of nanoparticles and nanostructures and is part of all of the author's publications within the scope of this thesis [1–4]. The working principle is essentially the same as for SEM: an electron beam is accelerated from a source with voltages up to 300 kV and focused with electromagnetic lenses onto a sample. But instead of detecting the backscattered and secondary electrons, information is obtained from changes in the primary electron beam after it passes through the sample. The specimen has to be very thin, usually thinner than 100 nm depending on its composition. Despite this constraint concerning the sample configuration, STEM could, even in its early states, produce images with an unprecedented resolution. Already in the early 70s, single heavy atoms were imaged on thin carbon substrates [41]. From that point the resolution was gradually improved by enhancing the major components and using very efficient monochromators to narrow the energy spread of the primary beam [42]. An important step towards today's high resolution STEM was the correction of spherical aberration (C_S), leading to resolutions in the Å range [42, 43] and further down to an information limit of only 0.5 Å, enabling the assignment of single atoms [44] and leading to new possibilities in materials science [45].

As mentioned above, there are constraints regarding the sample thickness and constitution when approaching atomic resolution. Therefore, sample preparation is an important part of the experimental work. Bulk samples can be prepared by e.g. cutting slices with a thickness of only a few 10 nm with a focused ion beam (FIB). Looking at nanoparticles simplifies the procedure, since the particles themselves have diameters of only several nm. They need to be deposited on a suitable ultra-thin substrate. Depending on the experiment, there are several commercially available options. The most widely used is an amorphous carbon layer on a holey carbon support with a backbone made of Cu or Au, but other materials like silicon nitride or boron nitride can also be used (cf. Chapter 3) [1].

For the acquisition of a micrograph the primary electron beam is deflected by deflector coils and scans over the specimen in x- and y-direction. It stops

regularly for a predefined acquisition time and every halt corresponds to a pixel in the obtained image. Upon passing through the sample, the electrons of the primary beam interact with the specimen matter and can be scattered or absorbed. Afterwards, the transmitted electrons reach the detectors, which are positioned in the back focal plane of the objective lens. There are usually two different imaging modes available: bright field (BF) and dark field (DF) imaging. The electron detectors for the acquisition of BF images are situated centrally in the path of the directly transmitted electrons. Therefore, bright pixels in the images correspond to a high intensity of electrons passing through the specimen unhindered or scattered under small angles. For acquisitions in DF mode, on the other hand, the detectors are positioned further from the center, allowing for a collection of electrons scattered under wider angles. For this work images were usually taken in the so-called high-angle annular dark field (HAADF) mode, where inelastically scattered electrons at high angles, usually over 5°, are detected [46]. HAADF is very sensitive to the atomic numbers (Z) of the specimen atoms, since with higher Z an increasing number of electrons is scattered to wider angles. Therefore, HAADF leads to a Z-contrast in the image, where atoms with higher atomic numbers appear brighter, and allows for high resolution [47]. It has the further advantage that because of the annular assembly of the detectors, the transmitted primary beam can pass to the electron energy loss spectroscopy detector, allowing for a simultaneous acquisition of an image and spectral information.

For the acquisition of high-resolution STEM images not only the detection mode and the sample constitution are relevant, but also the environmental conditions. Disturbances and perturbation due to mechanical vibrations, electromagnetic fields, acoustic waves, and unstable humidity or temperature need to be subdued and minimized to achieve significant results [48]. Especially temperature dependent drift of the sample holder or the support grid can be a problem, even, if the laboratory conditions are sufficiently good.

As an example for STEM imaging on the nanoscale, an HAADF image of Ag@ZnO core@shell nanoparticles is shown in Fig. 6. This micrograph was acquired with a probe-corrected *FEI* Titan^3 60-300 STEM with an X-FEG field emission source operated at 300 kV. Details on the particle synthesis and their morphology can be found in Chapter 5. This image also serves as a good example for the HAADF Z-contrast. The core material, Ag with an atomic number of 47, appears comparably bright and can be clearly separated from the surrounding ZnO shell, which is distinctly darker. Zn and O with atomic numbers of 30 and 8, respectively, are abundant in a ratio of 1:1 leading to an average atomic number of 19 for the ZnO shell area. The background of amorphous carbon appears again

gradually darker, since C has an atomic number of 6. Because of the elemental contrast, the composition of the core@shell nanoparticles can be examined with the STEM micrographs. In the case of Fig. 6 the spherically shaped Ag cores are distinctly separated from the ZnO shell, which is very equally distributed around the cores with an uniform thickness. The visibility of the core in the images is probably the most important advantage of STEM regarding the analysis of core@shell nanoparticles. Most analytical methods are surface sensitive and can not penetrate deep into the sample. With STEM, on the other hand, the information from all of the sample's volume is collected and the final image represents a 2D overlay, where for one pixel all of the atoms in the way of the electrons contribute to the final signal. The abundance of information naturally impedes the interpretation of the obtained images. Therefore, expertise and experience are important for a thorough evaluation of STEM micrographs.

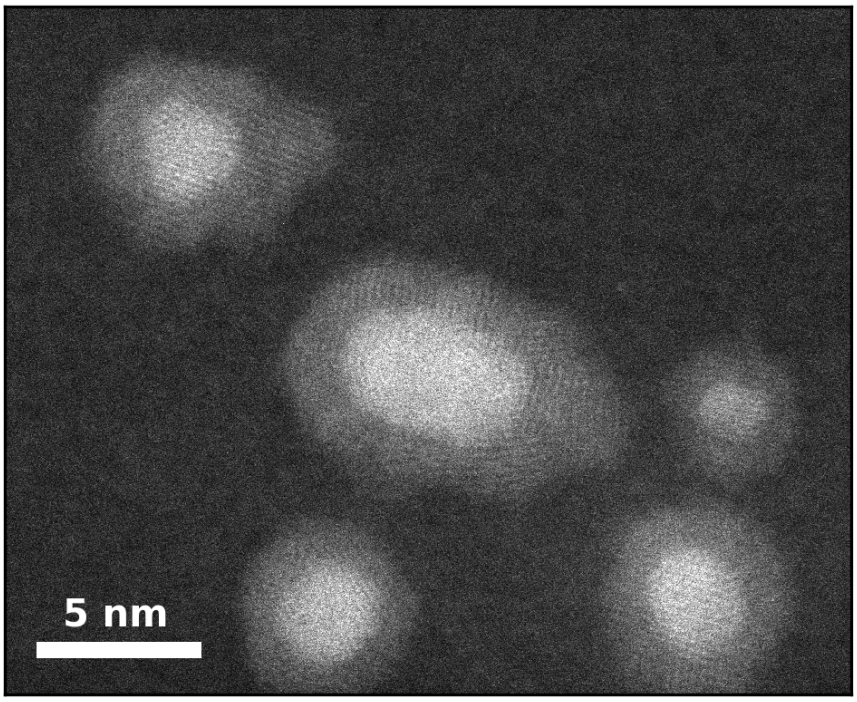

Figure 6: Detailed STEM HAADF image of spherically shaped Ag@ZnO nanoparticles on an amorphous carbon support. The Z-contrast of the imaging mode is obvious, as the heavier Ag atoms in the core appear brighter the the lighter Zn and O atoms in the shell.

There are advanced possibilities for the acquisition of information with a STEM, e.g. tomography to gain 3D information on the nanoparticle shape by tilting of the sample holder [49] or the use of a heatable support grid to learn about the temperature dependence of the particle properties and their alloying behavior [6, 8, 30, 50]. Further important analytical methods are energy dispersive

X-ray spectroscopy and electron energy loss spectroscopy, which will be explained in the following Chapters 2.2.3 and 2.2.4.

Besides the mentioned benefits of STEM, there are, of course, also disadvantages. Depending on the acquisition time and the electron dose, the incoming high energy electrons can alter or even destroy the specimen. Electron beam induced dynamics may cause displacement of surface atoms or sputtering effects [5], leading to altered alloying behavior or melting points. Nanostructures are more susceptible to such effects than bulk materials. To reduce the impact of the beam, the electron dose can be adapted or the accelerating voltage can be reduced [1]. Hydrocarbons pose another challenge, since they can be precipitated on the sample surface by the beam hindering the acquisition of high resolution images. Here, the helium droplet synthesis approach has advantages due to the absence of solvents, surfactants, or organic spacer molecules during fabrication, cf. Chapter 2.1.

2.2.3 Energy dispersive X-ray spectroscopy

A standard analytical method for the characterization of a sample's chemical composition, available in most types of electron microscopes, is energy dispersive X-ray spectroscopy (EDS). Upon stimulation by the incoming beam electrons, the specimen atoms emit characteristic X-rays. Those photons have sharply defined energies and can be unambiguously assigned to a specific atom species, identifying or even quantifying the present chemical elements [39]. For the emission of a photon the interacting beam electron must have enough energy to excite a ground state electron from an inner shell of the specimen atom. The resulting vacancy is filled by an outer-shell electron, which moves from a higher energy level to a lower one and emits its excess energy as an X-ray photon. For an efficient excitation process the beam energy should amount to at least twice the critical excitation energy of the respective atomic shell [39]. Beside the characteristic X-ray fingerprint of the specimen, the beam electrons additionally generate bremsstrahlung, thereby, creating a continuous background spectrum. This spectral background strongly influences the detection limit for abundant chemical elements in the specimen.

For the detection of X-ray photons direct semiconductor detectors are integrated in the microscopes. Within the doped silicon or high purity germanium detectors the photons are converted to electron-hole pairs and create a charge pulse proportional to the photon energy. Since the photon energy of characteristic X-rays is in the range of keV, up to several thousand electron-hole pairs may be generated. After the obtained signal is amplified and processed, it can be directly

related to the photon energy [51]. To keep the noise level low semiconductor detectors are often cooled with a liquid nitrogen reservoir. For the more modern silicon drift detectors (SDD) cooling is no longer necessary [52]. The typical energy resolution of the detector systems lies in the range of 120-140 eV [51].

In a scanning microscope, like a SEM or STEM system, EDS analysis can be conducted pixel by pixel, enabling the mapping of the occurrence of a certain element with spatial resolution. Since EDS data collection and micrograph acquisition can be done in parallel, it is even possible to project information about the chemical composition directly onto e.g. an HAADF image. The spatial resolution of the EDS data can be lower than for the corresponding micrograph because of an extended interaction volume in width and depth. X-ray photons originating from deeper within the sample are additionally reduced in intensity because they are subjected to absorption processes during their propagation to the surface. This is particularly problematic for lower photon energies [39].

In Fig. 7 an exemplary EDS spectrum of Ag@ZnO nanoparticles, deposited on an amorphous carbon support, is shown. It was acquired with an *FEI* Super-X four-quadrant detector in a probe-corrected FEI Titan^3 60-300 STEM. An HAADF micrograph of the analyzed area can be found in Fig. 38 (a) in Chapter 5. The spectrum was further processed and used for the generation of the spatially resolved EDS maps in Fig. 38 (b)-(d), mapping the distribution of Ag, Zn, and O with respect to the HAADF image to conclusively prove the formation of Ag@ZnO core@shell particles. In Fig. 7 the characteristic peaks of several elements are present in the collected energy range up to 10 keV and marked by colored vertical lines. Via lookup tables the peaks can be attributed to elements and level transitions: C K_α at 0.277 keV (black line), O K_α at 0.523 keV (green line), Zn L_α at 1.012 keV (red line), Si K_α at 1.740 keV (grey line), Au M at 2.120 keV (golden line), Ag L_α at 2.984 keV (blue line), Zn K_α at 8.637 keV (magenta line), and Au L_α at 9.712 keV (orange line). The peak around 0 keV is attributed to noise from the acquisition electronics. Because of the high count numbers for the C K_α and the O K_α peaks with about 22 700 counts and about 600 counts, respectively, the spectrum is cut on the y-axis to facilitate a presentation of the smaller peaks. All the other elemental peaks are fully displayed. In the whole spectrum the background from bremsstrahlung, as mentioned above, can be observed and it increases towards 0 keV. The still very common Siegbahn nomenclature was used for naming the peaks. The capital letter gives the atomic shell, where the original ionization occurs, and the following Greek letter in subscript denotes to the order of relative intensity for the different transitions into this shell [39]. It should be mentioned, that there is an alternative nomenclature from IUPAC, which will not

be further discussed here.

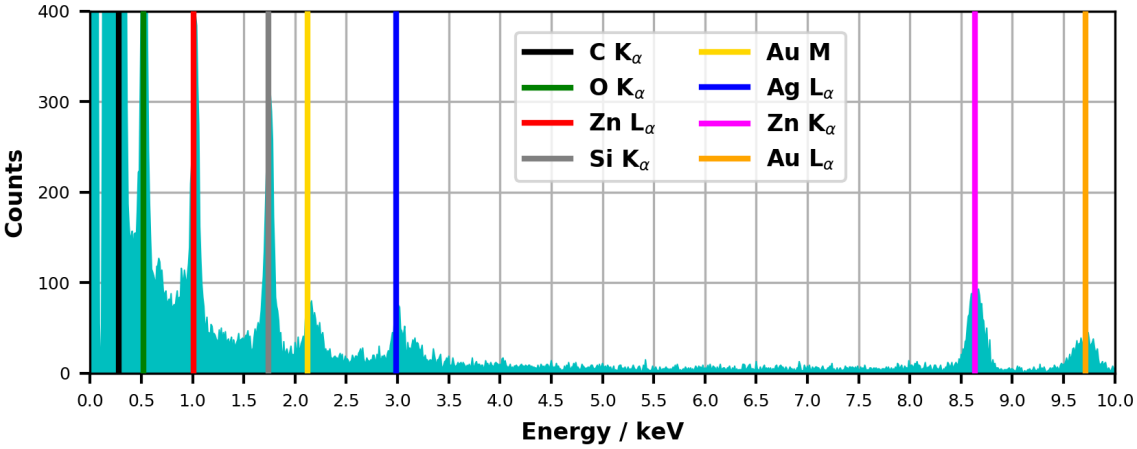

Figure 7: EDS spectrum of Ag@ZnO nanoparticles on an amorphous carbon support, as acquired by STEM. The characteristic X-ray peaks are marked with colored lines and attributed to the respective elements and level transitions.

From the peak assignments in Fig. 7 it is clear that the chemical elements found in the sample by means of EDS are C, O, Zn, Si, Au, and Ag. Since the sample under investigation consists of Ag@ZnO nanoparticles, the occurrence of silver, zinc, and oxygen is expected. A high carbon peak was expected as well, because the substrate, on which the particles reside, is made of amorphous carbon. The appearance of gold can be explained with the backbone grid of the sample support, which was in this case made of Au. If one uses a copper support, residues of Cu would be found instead. Silicon on the other hand should not be present on the sample, but is almost always found on this kind of substrates. The ultra-thin amorphous carbon layer is grown on a Si surface and there are residues left from this process. It further stands out that the Si peak and especially the C peak are very high compared to the other elements. This is explainable by the low surface coverage with nanoparticles. The bigger part of the scanned area comprises only of the amorphous carbon substrate. Finally, all the occurring elements are accounted for, but a certain experience in the evaluation of the EDS data is necessary to avoid misinterpretations.

2.2.4 Electron energy loss spectroscopy

The second important spectroscopic technique employed in STEM is electron energy loss spectroscopy (EELS). The technique has already been known since its development back in the 1940s [53], but had its breakthrough only in the late 20th century, when the technology in electron microscopes was rapidly advancing and modern day instruments became widely available. As mentioned

above, the electrons of the incoming beam can undergo inelastic scattering events upon their transition through the sample. The exact amount of energy lost because of inelastic scattering can give valuable insight into the origin of this loss. There are various possibilities for inelastic interactions like e.g. inner shell ionizations, band transitions in conductors, and phonon or plasmon excitations. Characteristic energy losses in the transmitted electrons can thus be linked to the chemical composition or the electronic structure of the sample [54]. The energy resolution of EELS spectra in a modern system can go down below 0.1 eV, whereas the method strongly profited from the development of highly efficient monochromators [42]. The high lateral resolution of acquired EELS data in aberration corrected STEM systems even allows for the investigation of single atoms [55].

For the discrimination of electrons according to their energy a magnetic prism is used. Within a uniformly applied magnetic field the electrons are forced on circular trajectories by the Lorentz force. The radius R of the trajectory is then, according to Eq. 4, determined by the kinetic energy of the electron E_{kin} with the mass of the electron m_e, the elementary charge e, and the applied magnetic field B being constant [36].

$$R = \frac{\sqrt{2 \cdot m_e \cdot E_{kin}}}{e \cdot B} \tag{4}$$

The overall deflection by carefully shaped electromagnetic polepieces is typically 90° and the electrons are discriminated according to R and, therefore, to their energy E_{kin}. An important second function of the magnetic prism is the focusing of the electrons. They may enter the spectrometer not perfectly perpendicular, but under a small angle. That changes their path length within the magnetic field and gives rise to an increase or decrease in the deflection angle. This way the electrons with equal energy but varying incoming angles are focused to a single point. The formed spectrum is finally projected on an electron detector and subsequently collected by a charged-coupled device (CCD) sensor. The entrance aperture for the spectrometer is positioned centrally below the sample. This allows for a simultaneous usage of the HAADF detectors (cf. Chapter 2.2.2), giving the advantage that EELS data can be mapped directly to a correlating HAADF micrograph. More detailed information about the EELS spectrometer, including schematics, can be found in Ref. [54].

The described EELS detection method allows for an assessment of the kinetic energy of the collected electrons. To provide absolute values of the energy loss, the measured energy needs to be subtracted from the incident energy E_0. As point of reference for this procedure the zero-loss peak (ZLP) in the acquired

spectrum can be utilized. The ZLP is a dominant feature in the spectrum and corresponds to the electrons which passed through the sample without losing any energy. In the final spectrum the ZLP needs to be centered at 0 eV of energy loss to ensure a valid assignment of other features. The energy loss is typically plotted on the positive x-axis with the count of detected electrons, corresponding to a certain energy loss, on the y-axis. Peaks and features in such a graph can be related to the events on which the electrons released that energy. Examples for EEL spectra and the information they contain, e.g about the chemical composition or the specimen thickness, can be found in Figs. 25, 26, 27, and 28 in Chapter 3.

As mentioned, the ZLP is quite dominant in the spectrum and potentially hides interesting features close to it in the low loss region of EEL spectra, where especially plasmonic peaks can be found. In contrast to the high energies necessary for the ionizations of inner shells, the excitation of plasmons in the sample just needs small amounts of energy, which is provided by the passing electrons. For bulk materials the peaks are well detectable because of the vast amount of specimen matter. For nanoparticles or nanostructures, on the other hand, things look different. The little volume and low thickness of investigated materials in such samples complicate the acquisition and evaluation of EELS data. To provide easier access to weak plasmonic peaks, ultra-thin hexagonal boron nitride was employed as a new kind of substrate for nanoscale plasmon spectroscopy and tested with Ag and Ag@Au nanoparticles synthesized with the helium droplet approach [1]. The thinner the underlying substrate, the better the signal to noise ratio for the EELS information acquired from the particles. Furthermore, boron nitride has the advantage of a wide bandgap, which keeps the background signal from the substrate in the low-loss region of the EEL spectra low. Details about this experiment may be found in Chapter 3.

2.3 Localized surface plasmon resonance

A plasmon, in short, is the quantum of a collective excitation of the conduction electrons and, thereby, a quasiparticle for an oscillation of the electron density with respect to the positive ions in metals [56]. The displacement of the electron cloud from the equilibrium position can be seen in analogy to a real plasma. In more detail, plasmons are classified as bosonic quasiparticles because of their well defined frequencies [57]. The bulk plasma frequency of the free electron gas ω_p can be derived using Eq. 5 with the number of electrons per volume unit n,

the electron charge e, its effective mass m_e, and the vacuum permittivity ϵ_0.

$$w_p = \sqrt{\frac{n \cdot e^2}{m_e \cdot \epsilon_0}} \tag{5}$$

Using ω_p within the context of Drude-Sommerfeld theory yields a frequency dependence of the dielectric constant $\epsilon(\omega)$, where its real part becomes negative for frequencies smaller than the plasma frequency, which includes the infrared and visible range. A consequence thereof is a high reflectivity of metals for visible light, though the theory needs to be expanded by taking the response of bound electrons into account. Those can undergo interband transitions and, thereby, modify the dielectric function of real metals [58, 59].

Within the bulk of a metal only longitudinal charge oscillations are possible, so called volume plasmons, which can be excited by particle impact but do not couple to transverse electromagnetic waves [60]. This changes when the surface of a real metal is taken into account, since specific plasmon modes at the surface can be excited by the electric field of electromagnetic radiation [57]. Due to the strong coupling between the surface plasmon and the incoming photon the resulting electromagnetic waves traveling on the metal surface are called surface plasmon polaritons (SPP). To compensate for a momentum mismatch upon the excitation of a SPP, phase-matching techniques like prism couplers, grating couplers or other geometric metallic structures and edges can be used [60].

In cooperation with the Nano-Optics Group at the Institute of Physics at Karl Franzens University Graz a measurement series on the newly established photoemission electron microscope (PEEM) was conducted to visualize SPPs on metallic surfaces. Details on the PEEM setup can be found in Chapter 2.6. The aluminum sample, produced by the Nano-Optics Group by means of electron beam lithography, contained a series of arrays with triangles in varying sizes and orientations. Those were illuminated by the second harmonic of a p-polarized Indigo-S Ti:Sapphire laser system (*Coherent*) tuned to a wavelength of 385 nm with a pulse duration of 30 ns and a repetition rate of 5 kHz at a laser power of 5 mW. In a two-photon photoemission (2PPE) process (cf. Chapter 2.6.2) electrons are emitted and collected by the PEEM for visualization. In Fig. 8 triangles with a side length of 3 μm are exemplarily shown with the laser light coming from the right side. For the acquisition of this image the energy filter of the PEEM was set to 4.2 eV with a 1750 μm aperture and an acquisition time of 300 s.

The edges of the triangles imaged in Fig. 8 serve as starting points for the SPPs, which are indirectly visualized as a Moiré pattern. The standing waves form as a superposition of the SPPs and the laser light field. The pattern changes for trian-

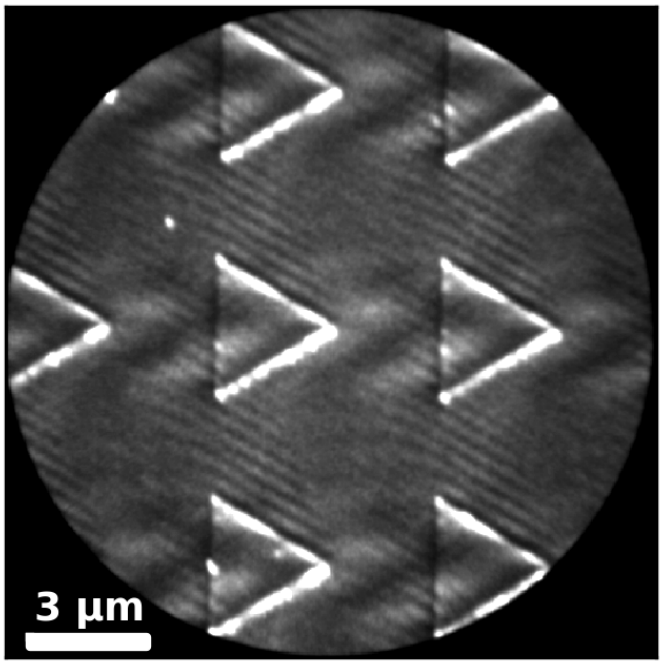

Figure 8: PEEM image of SPPs on an Al surface excited by a 385 nm p-polarized laser beam (coming in from the right side of the image). The brighter a pixel appears the more electrons are emitted from the according sample area. From the edges of the triangles SPPs are launched and the observed Moiré pattern corresponds to a superposition of the SPPs and the light field of the laser pulse allowing for an indirect visualization of the propagating SPPs. Modified from Ref. [61].

gles with other orientations and can be theoretically reproduced by considering the involved wave vectors. Further results and a more detailed explanation can be found in the Master's thesis of Thomas Jauk [61]. A more widely used method for the local excitation and investigation of SPPs is scanning near-field optical microscopy (SNOM), where coupling is achieved by bringing a confined light field close to a suitable interface [59].

When there is resonant interaction of the electrons with the incoming photons, it is called surface plasmon resonance (SPR). In the context of surface plasmons, the surface needs to be treated as an interface between the metal and the surrounding medium, which is best described by its dielectric function. Any changes at the interface strongly influence the SPPs and alter the spectral position of the resonance. SPR sensors utilize those shifts in the resonance to detect the presence of adsorbed molecules. The method is especially popular in the field of biochemistry, where it brings the advantage of working without any color or fluorescent markers [58]. A common way of experimentally realizing a SPR

sensor setup is the Kretschmann configuration [62], a prism coupling scheme. In the Kretschmann configuration a thin metal film is evaporated onto a glass prism. Light is guided through the prism to the back side of the film at an angle greater than the critical angle of total reflection. The evanescent electric field excites SPPs on the front side of the metal film at the interface between metal and adjacent medium, e.g. air or some liquid analyte. The SPP excitation is visible as a minimum in the reflected beam intensity depending on the angle of incidence [60]. The position of this minimum can be used as a reliable indication for environmental changes, allowing for the detection of the absorption or removal of a target species on metal surfaces with sub-monolayer accuracy [59].

As in many aspects, there are also major differences for plasmons when metallic nanoparticles are under investigation instead of macroscopic samples and surfaces. Once the size of the examined system becomes much smaller than the incoming wavelength, localized surface plasmons (LSPs) play a role. Contrary to the above mentioned SPPs LSPs are non-propagating excitations and can be excited directly, without the use of any coupling techniques. The oscillating electromagnetic field effectively displaces electrons in the sub-wavelength sized conductive nanoparticles, which then are subjected to restoring forces due to the curvature of the particle surface. The emerging resonance, called localized surface plasmon resonance (LSPR), leads to an electromagnetic field enhancement inside the particle and close to its surface on the outside. The quasi-static approximation of the interaction of a spherical sub-wavelength metallic nanoparticle with a harmonically oscillating electromagnetic field results in the term for the polarizability α of the particle shown in Eq. 6 [60]. α depends on the radius of the particle a, its dielectric function $\epsilon(\omega)$, and the dielectric constant of the surrounding medium ϵ_m with 2 being the geometrical factor for a sphere.

$$\alpha = 4 \cdot \pi \cdot a^3 \cdot \frac{\epsilon(\omega) - \epsilon_m}{\epsilon(\omega) + 2 \cdot \epsilon_m} \tag{6}$$

From Eq. 6 it can be deduced that a resonant enhancement of the polarizability is reached when the denominator goes to zero. For a small imaginary part of $\epsilon(\omega)$ this leads to Eq. 7, the so called Fröhlich condition [60].

$$\mathrm{Re}[\epsilon(\omega)] = -2 \cdot \epsilon_m \tag{7}$$

The Fröhlich condition describes the dipole mode of the plasmon and predicts a redshift of the resonance with increasing ϵ_m. If dipole oscillations in spherical nanoparticles with diameters under about 100 nm are considered, Mie theory

provides a good approximation for scattering and absorption under irradiation with visible or near-infrared light. It is often used for the simulation of according extinction spectra. For experimentally synthesized particles the picture is more complicated since the extinction bands are strongly influenced by the aspect ratio of ellipsoidal shaped particles and the particle size. The extinction peak in the spectrum is broadened and shifted, depending on the uniformity of the produced nanoparticles as well as on the substrate and the surrounding medium [63].

UV/vis absorption spectroscopy is a widely used method to determine the plasmonic properties of nanoparticle samples (cf. Chapter 2.5). Primarily, Au and Ag nanoparticles are investigated with visible light since for them the Fröhlich condition is met in the visible spectral region. Because of this fact, the use of colloidal Au in numerous applications, e.g. stained glass or ornamental valuables, is verified all the way back to the 4^{th} century. In 1825 Michael Faraday first related the optical properties to the size of the Au particles [57]. As a further application, LSPs in nanoparticles play an important role in surface enhanced spectroscopic methods like metal enhanced fluorescence or surface enhanced Raman spectroscopy (cf. Chapter 2.4). The strongly amplified electromagnetic field in close proximity of a particle leads to a much stronger Raman signal, since the Raman scattering signal scales approximately with the fourth power of field enhancement [63].

Another spectroscopic method, besides UV/vis spectroscopy, allowing for the excitation and visualization of plasmons is EELS (cf. Chapter 2.2.4). The fast moving electrons of the primary beam in a STEM system are well suited for the excitation of plasmons, both in the bulk and on the surface of a metallic specimen. When the electrons, with energies up to 300 keV, pass through the sample, nearby electrons are displaced by Coulomb repulsion. Thereby, a region of net positive potential, a so called correlation hole, is formed trailing behind the beam electrons and the displaced electrons create plasmons by showing an oscillatory response. The beam electrons themselves lose energy because of the backward attractive force of the correlation hole [54]. The inelastic scattering event upon the creation of a plasmon gives rise to peaks in the according energy loss spectrum at loss energies corresponding to the plasmon energy E_p, shown in Eq. 8, and its multiples. E_p is depending on the plasma frequency ω_p (cf. Eq. 5), with the reduced Planck constant $\hbar$.

$$E_p = \hbar \cdot \omega_p \tag{8}$$

Already before entering the bulk, the charge of the beam electrons polarizes the

surface of a metallic specimen, creating longitudinal charge density waves. The oscillation frequency of those surface plasmons needs to satisfy the boundary condition that the dielectric functions of the specimen and its surrounding medium add up to zero. For a metal insulator interface with a positive dielectric constant of the surrounding insulating medium ϵ_m this results in a surface plasmon energy E_s described by Eq. 9 [54].

$$E_s = \hbar \cdot \frac{\omega_p}{\sqrt{1+\epsilon_m}} \tag{9}$$

For the simple case of a metallic specimen surrounded by vacuum ($\epsilon_m = 1$) the surface plasmon peaks in the EELS spectrum appear at loss energies reduced by a factor $1/\sqrt{2}$ compared to E_p. It should be noted that not only the constitution of the sample and the surrounding contribute to the final spectrum, but also other factors like the incident angle of the electron beam relative to the surface normal of the sample. By tilting the specimen away from perpendicular incidence, for example, peaks originating from surface plasmon scattering become more dominant [54].

Also for the excitation of LSPs in nanoparticles the electron beam can be used instead of a light source. In the context of this work EELS was employed to obtain information about the plasmonic properties of single Ag and Ag@Au core@shell nanoparticles (cf. Chapter 3) [1]. The small size of these particles in the range of only 10 nm makes it difficult to obtain a reasonable signal to noise ratio. Besides the development of a specially designed algorithm for data extraction and background subtraction, the use of an ultra-thin hexagonal boron nitride (h-BN) substrate was essential for the generation of reliable data. As a result the resonances of several LSP modes of the nanoparticles could be identified in the EELS data and finally mapped directly onto STEM images, proving the feasibility of such measurements also for very small specimen volumes.

2.4 Surface enhanced Raman spectroscopy

The Raman effect was discovered by the Indian scientist C.V. Raman in 1928 [64], a few years after the theoretical prediction of inelastic scattering of light by A. Smekal [65]. The effect was named after him and for his discovery Raman was also awarded the Nobel prize in Physics in 1930, only two years after his publication. Raman scattering is a form of inelastic scattering by which the produced secondary photon differs in energy from the primary incident photon. When the incoming light scatters at matter, the difference in energy is transferred and corresponds to the vibrational energy of the irradiated molecule or crystal.

For molecules also the transformation into rotational energy is feasible. Figure 9 visualizes the process behind Raman scattering on the vibrational levels in a Lennard-Jones potential curve [51]. In panel (a) monochromatic light with the frequency ν_0 triggers an excitation from the vibrational ground state into a virtual unstable energy state, represented by the dashed line. The relaxation from this virtual state does not bring the system back into the ground state, but into another vibrational state at higher energies. Because of the smaller energy difference, the emitted photon posses a decreased frequency ν_R compared to ν_0. The so-called Stokes Raman scattering produces a red shifted spectrum. In panel (b), on the other hand, anti-Stokes Raman scattering is schematically explained. Here, the incoming photon is scattered from an excited vibrational state into a virtual state. Upon relaxation the system goes directly into the vibrational ground state and the emitted photon has an increased frequency. Therefore, anti-Stokes scattering produces a blue shifted spectrum.

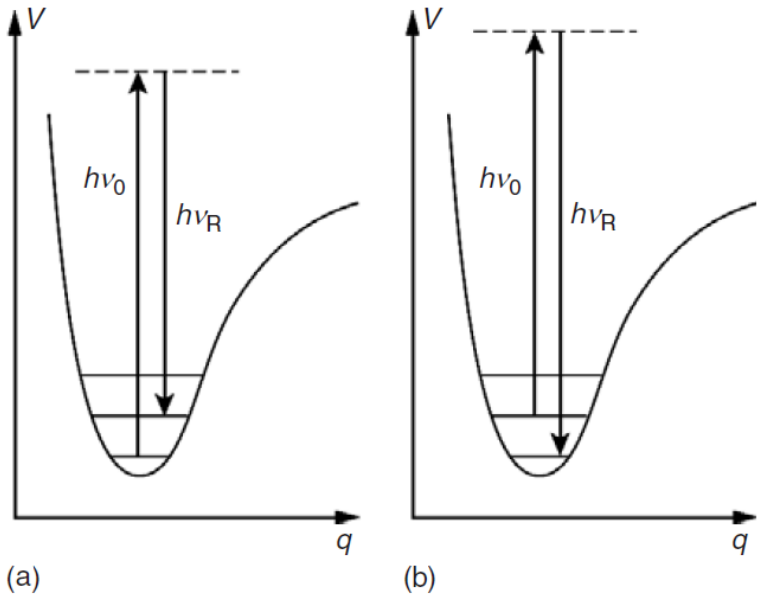

Figure 9: Vibrational modes in a Lennard-Jones potential schematically visualizing (a) Stokes Raman scattering and (b) anti-Stokes Raman scattering. Reprinted from Ref. [51], with permission of John Wiley & Sons, Inc.

Vibrational Raman spectroscopy is widely used as an alternative to infrared (IR) spectroscopy. The obtained spectrum for a molecule usually contains a whole set of bands that serve as a "fingerprint" of the molecule. The measured intensity is plotted above the Raman shift, which is the energetic difference between the detected light and the primary photons. Traditionally, the Raman shift is given in wavenumbers cm^{-1}, which equals 1 over the wavelength λ. The interpretation of a Raman spectrum can be difficult, depending on the complexity

of the molecule, and requires experience and knowledge about the bond structure. On the example of cellulose in an embedding compound, it is shown in Fig. 10 how the chemical composition of a sample can be deduced from the Raman spectrum [66]. By assigning the various stretching and bending vibrations, the bands disclose information on the H and C bonds and the functional groups present in the molecule. Because of the unambiguousness of Raman spectra a comparison to literature or to database entries can be used for the identification of the specimen. It should be mentioned that not all vibrational modes can be detected by Raman spectroscopy. Only vibrations, which change the polarizability of the molecule, are Raman active and give a signal [67].

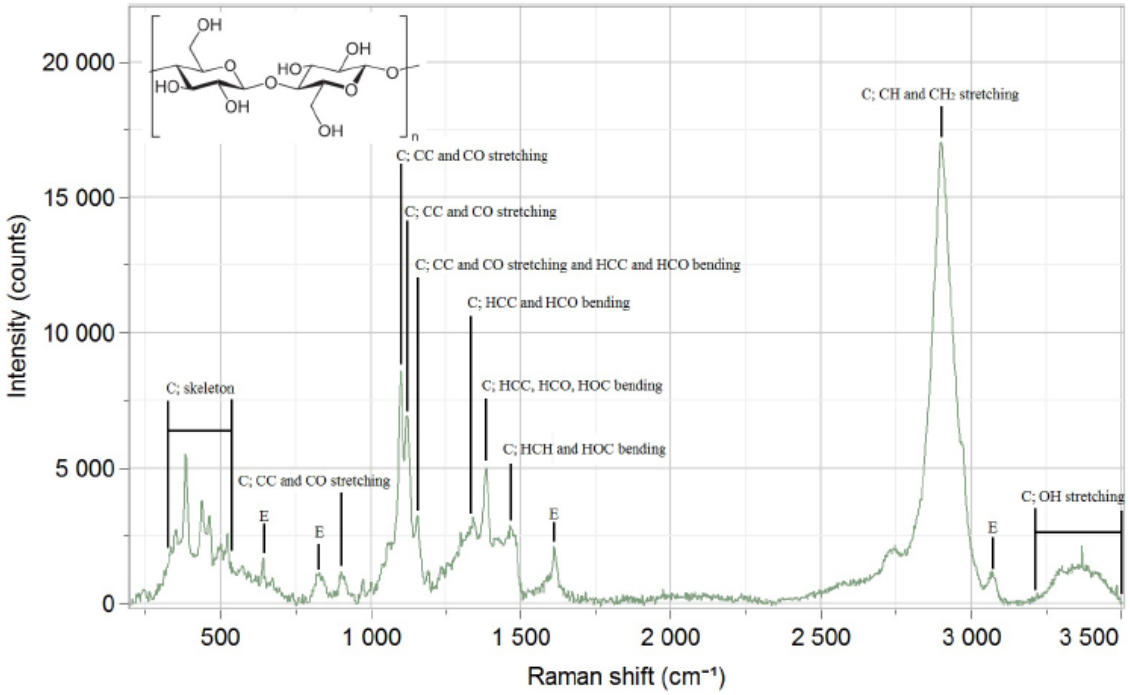

Figure 10: Exemplary Raman spectrum of embedded cellulose with all visible bands assigned. The letter C marks bands originating from the cellulose molecule while E stands for the embedding compound. Reprinted from Ref. [66].

Regarding the experimental setup, usually a laser source is used to generate the monochromatic primary light. Since only the detected shift is plotted in a Raman spectrum, varying laser wavelengths can be employed. Note that the choice affects the overall intensity of scattered light, for there is a dependence on the fourth power of the frequency. Therefore, the collected intensity for red light will be lower than for a blue laser, e.g. the signal strength ratio for excitation with 785 nm compared to 514.5 nm is 0.18 [51]. In an optical setup the laser is focused, often through a microscope objective, onto the sample and the resulting

Raman shifted light is guided through an edge or notch filter into a spectrograph. The edge filter is important and needs to reflect or absorb the primary laser light, while it lets the e.g. red shifted Stokes Raman scattered light pass. The efficiency of such a setup strongly depends on the quality of the filter and the collection efficiency of the scattered light, which is statistically emitted to all spatial directions. Overall, the very low yield of linear Raman scattering (about 1 in 10^6 to 10^8 photons) is the major obstacle to overcome with this spectroscopic method. The vast majority of the photons undergo elastic Rayleigh scattering processes. Further problems in the spectral analysis mostly originate in the high fluorescence background from the sample or the setup itself, which masks the Raman spectrum. Red or near infrared lasers are often used because there are fewer molecules with strong absorptions and fluorescence in these spectral ranges. A drawback is that, as mentioned above, the intensity of scattered light is thereby reduced.

Several new techniques and refinements were developed over the years, trying to improve the efficiency and signal to noise ratio of Raman spectroscopy, some of which will now be mentioned shortly. Resonance Raman spectroscopy enhances the intensity of Raman scattering by choosing the primary photon energy in a way that the virtual level lies nearby an eigenstate of the molecular system. During electronic excitation certain vibrational modes undergo changes manifesting in large increases in polarizability and therefore Raman intensity (up to a factor of 10^4) [51]. Stimulated Raman spectroscopy is about the resonant enhancement of certain transitions by introducing a second laser, providing so-called Stokes photons, besides a high power primary pump laser. When the frequency difference of the primary photon and the Stokes photon is similar to a possible vibrational or rotational transition, this transition is enhanced. By scanning the frequency of the Stokes laser, a Raman spectrum is obtained [67].

A very efficient improvement of the Raman signal up to over six orders of magnitude can be reached by employing surface enhanced Raman spectroscopy (SERS), where the investigated molecules are adsorbed on a metal surface. The exact source of the strong signal amplification with SERS is still a matter of debate, but there are two main mechanisms that are referred to for a thorough explanation. The first one attributes the enhancement to the formation of a charge transfer complex between the adsorbed molecule and the metal. It is bolstered by the fact that molecules with π electron clouds or lone pair electrons show a comparably strong SERS effect [51]. The, more often mentioned and better known, second explanation takes the enhanced electromagnetic field on the metal surface

into account. The incident primary light not only scatters at the molecules, but also excites surface plasmons at the metal surface or localized surface plasmons (LSP) in metallic nanoparticles (cf. Chapter 2.3). Thereby, the electromagnetic field strength enhancement felt by the adsorbed molecules is maximized, when the incoming light is in resonance with the plasmon frequency. Not only the Raman signal is magnified by field enhancement, but also the primary light before it interacts with the molecule. Therefore, the effect contributes twice to the overall signal increase [68]. Several further parameters have a strong influence on the amplification, like the distance from surface to molecule, the orientation of the molecule, and the surface properties. The electronic structure of the employed metal is thus important, as is the morphology of its surface, especially the roughness. As discussed in Chapter 2.3, a structure can be used to efficiently couple incoming light into the metal surface and excite plasmons. Metallic nanoparticles residing on the surface can provide such a structure. Once the nanoparticles become smaller than the wavelength of the irradiating light, LSPs are excited and contribute to the enhancement. Mostly Au and Ag are used as SERS substrates, since their plasmon resonances lie in the visible and near-infrared spectral region.

SERS substrates don't necessarily need to feature large-scale metal surfaces. Nanoparticles are well suited as active substrates on their own even when deposited on non metallic surfaces. Especially conglomerations of nanoparticles give significantly larger Raman signal enhancements, if the individual particles are separated by distances smaller than the wavelength of the primary light. In this configuration so-called hot-spots form, where the transient dipoles of the nanoparticles couple and the enhanced electromagnetic fields interfere coherently. For molecules placed at hot-spots enhancement factors of up to 10^{12} were reported, possibly facilitating single molecule detection [63]. SERS opens up a new variety of applications for sensor systems on the nanoscale, since it allows for a fast and efficient detection and identification of organic molecules.

In the course of this work, it was tried for the first time to employ Ag@Au core@shell nanoparticles, produced with the helium droplet synthesis approach, as substrates for SERS measurements (cf. Chapter 4) [2]. Several samples with different Ag/Au ratios were prepared on fused silica slides, whereby the localized surface plasmon resonance (LSPR) of the nanoparticles was spectrally red-shifted with increasing Au content. For conducting the SERS measurements the samples were functionalized with 4-methylbenzenethiol (4-MBT). A drawing of the chemical structure of 4-MBT is shown in Fig. 11. It is a small and simply built molecule comprising of a benzene ring with a methyl group and a thiol

group in para positions. The Raman fingerprint of 4-MBT is well known, which renders this molecule ideal for proof of principle measurements.

Figure 11: Structural drawing of the Raman active 4-methylbenzenethiol molecule. 4-MBT is used to for the functionalization of nanoparticle substrates for conducting the SERS measurements presented in Chapter 4.

For the acquisition of Raman spectra, together with our partners at FELMI, a LabRam HR 800 spectrometer with a x10 Olympus MplanN objective was used. It allows for automated scanning of the sample and fast switching between three different laser sources, supplying monochromatic light with wavelengths of 473 nm, 532 nm, and 633 nm. The unscaled results for 4-MBT molecules attached to Ag nanoparticles with diameters around 5 nm are presented as an exemplary result in Fig. 12. The other obtained spectra for the SERS measurements on the synthesized nanoparticle substrates can be found in Chapter 4. In Fig. 12 the important bands of 4-MBT were assigned by comparison to available literature. Note that the band at 1080 cm^{-1} corresponds to a combination of three vibrational modes, namely a phenyl breathing mode, the C-H in-plane bending, and the C-S stretching.

In the above mentioned experiment, Raman spectroscopy was combined with optical microscopy, where the substrate can also be viewed through the objective, which is used to focus the laser beam onto the surface. A further improvement, especially for research on small structures and particles, is the combination with an electron microscope. At FELMI a newly available Zeiss Sigma 300 VP SEM system is directly connected with a Witec RISE Raman microscope. The sample holder can be moved from one system to the other, while the exact same position on the substrate surfaces is kept. This allows for a very accurate selection of special sites on the substrates, e.g. hot-spots. Possible future experiments on such a system could give more insight into the quality of nanosized SERS substrates.

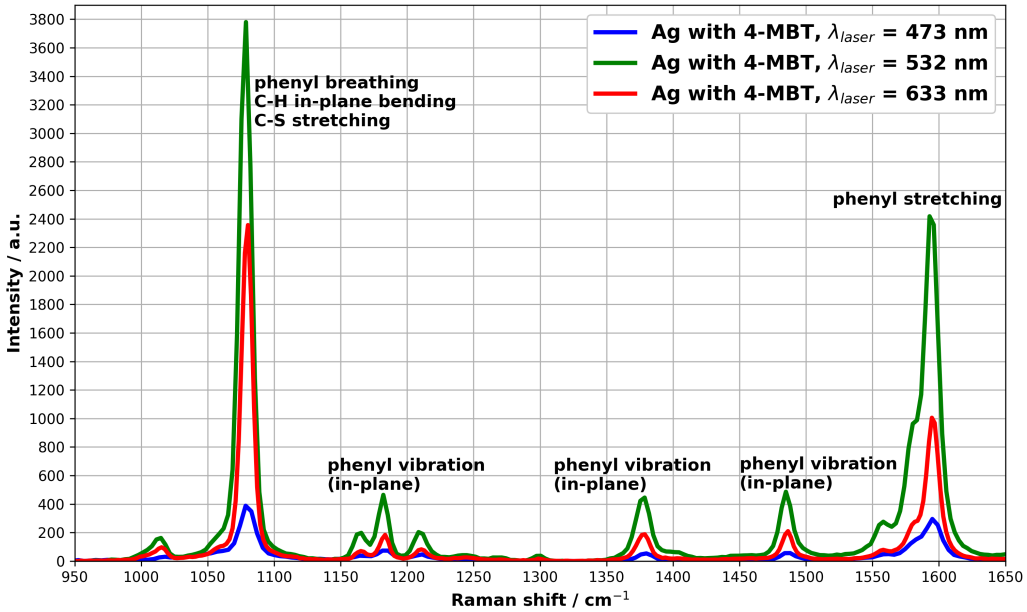

Figure 12: Raman spectrum from a Ag nanoparticle SERS substrate functionalized with 4-MBT. The relevant bands are assigned. Modified from Ref. [2]

2.5 UV/vis absorption spectroscopy

UV/vis absorption spectroscopy is a well established method for the measurement of a sample's absorption in the spectral range from the ultraviolet at around 190 nm up to the end of the visible range at about 780 nm, sometimes into the near infrared above 1000 nm. The absorption is caused by electronic transitions in the sample material. Strong transitions in molecules from non bonding levels n to antibonding σ^* levels $n \rightarrow \sigma^*$ can usually be found in the range from 150 to 250 nm. However, more relevant over a wide spectral range are $n \rightarrow \pi^*$ or $\pi \rightarrow \pi^*$ transitions into the antibonding π^* levels [51]. In solids, band transitions between valence and conduction bands or from bands to localized levels contribute to UV/vis absorption, e.g. band gaps of semiconductors are observable in UV/vis spectra as steep edges in absorption [51]. For metallic nanoparticle samples LSPs can be excited and thus show in the absorption spectra as broad features around their resonance frequency, cf. Chapter 2.3. The excitation of plasmons with visible light is only possible for certain metals including Ag, Au, and Cu.

The general functionality and overall setup of a UV/vis spectrometer is exemplarily shown with the *Shimadzu* UV-1800 spectrophotometer. It was used for all UV/vis measurements in the course of this work, with kind permission from the Institute of Solid State Physics at Graz University of Technology. This system

is built in a double beam configuration with two separate photodiode detectors, allowing for an *in situ* background correction via a simultaneous measurement of the absorption of the sample and a reference. The two light sources are a deuterium lamp for the UV spectral region starting at 190 nm and a tungsten halogen lamp for up to 1100 nm. The switching between both lamps is realized by a rotating mirror and the switching wavelength can be varied in the range from 295 to 364 nm. A blazed holographic grating is used as a monochromator with the ability to scan through the whole wavelength region by varying its angle. In Fig. 13 a schematic of the full optical system and the beam path is presented [69].

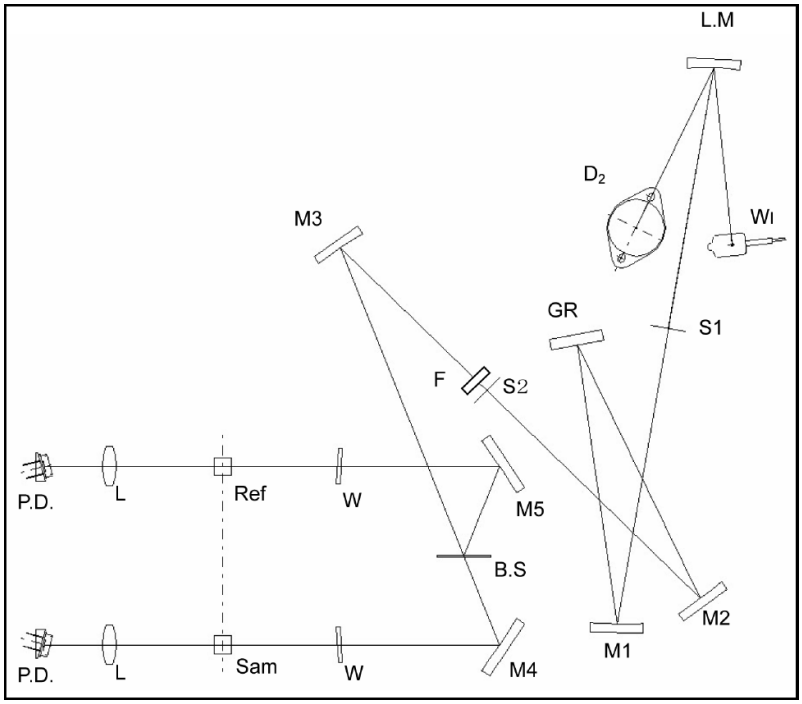

Figure 13: Schematic representation of the optical system in a *Shimadzu* UV-1800 spectrophotometer with the following abbreviations: photodiode (P.D.), lens (L), sample cell (Sam), reference cell (Ref), window plate (W), beam splitter (B.S), mirror (M1-M5), filter (F), grating (GR), entrance slit (S1), exit slit (S2), deuterium lamp (D_2), tungsten halogen lamp (WI), and rotating light source mirror (LM). Reprinted from Ref. [69].

Regarding sample preparation, the analyte is often diluted with a suitable solvent and filled into a phial, which is placed inside the spectrometer. The same solvent in an identical container, but without the analyte, is placed in the reference position of the spectrometer. This allows for an efficient and accurate background subtraction. Dissolved samples have the advantage that they usually provide a high optical density, resulting in pronounced spectra. Also nanoparticles are

usually prepared in the form of a colloidal dispersion, especially when they are produced by wet chemical routes. Upon fabrication with the helium droplet synthesis approach, the nanoparticles can only be deposited on a solid substrate. Since the substrate should be transparent in the whole investigated spectral range, Corning 7980 fused silica with a thickness of 1 mm is employed. For obtaining reliable results, it is necessary to keep the surface coverage in the sub-monolayer regime to prevent conglomeration.

Figure 14 shows an exemplary set of UV/vis absorption spectra obtained with the above mentioned *Shimadzu* UV-1800 spectrophotometer. Ag and Au nanoparticles of about 5 nm in diameter were synthesized with the helium droplet approach and deposited on a fused silica slide to serve as SERS substrates [2]. Thereby, the obtained surface coverage for a deposition time of four hours was around 20%. The according experiment is described in detail in Chapter 4. A fused silica slide from the same batch was used as reference and the presented spectral data is background corrected.

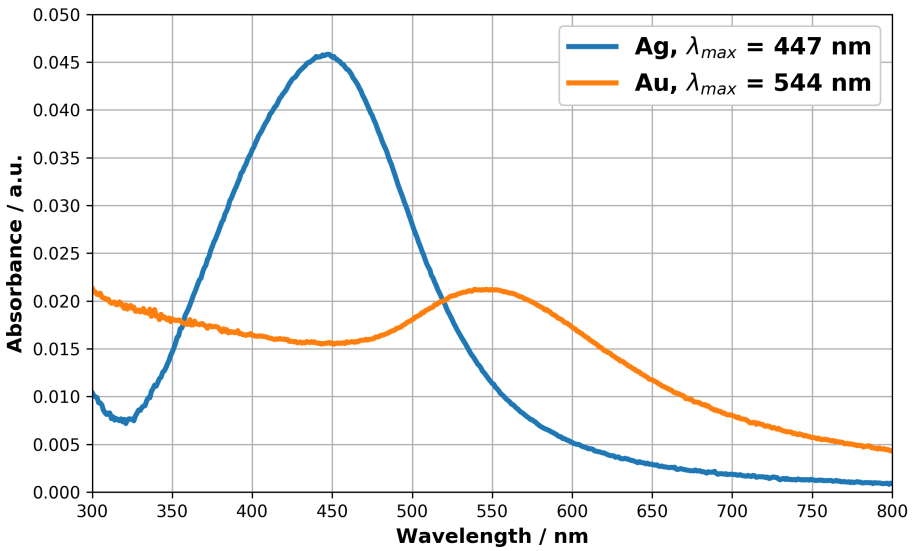

Figure 14: UV/vis absorption spectra of Ag and Au nanoparticles with diameters around 5 nm deposited on fused silica slides. The broad peak in each spectrum corresponds to the according LSPR. The maxima of the peaks are situated at 447 nm for Ag and 544 nm for Au. Modified from Ref. [2].

The blue and orange lines represent the spectra of the Ag and Au nanoparticles. The peak maxima at 447 nm for Ag and 544 nm for Au are attributed to the LSPRs of the particles. The relatively broad peak structure indicates a certain size distribution of the nanoparticles, since the spectral position of the LSPR is size and shape depended. The particle size distribution is inherent to the helium

droplet approach (cf. Chapter 2.1) and because the deposition is of statistical nature, also agglomerations on the substrate are likely to happen, even for a low surface coverage. At close examination, the Au peak appears less symmetric with a more pronounced tail towards longer wavelengths. This difference probably originates from the empirically determined effect that for the used synthesis parameters Ag tends to form very regular spheres. Au, on the other hand, has a tendency to favor deviations from the perfect spherical shape towards an elongated axis. Furthermore, though the particle density is the same, the LSPR peak is more intense for Ag. Silver particles are thus used more often in sensing applications, although, Au is less susceptible to environmental influences, especially on the nanoscale.

2.6 Photoemission electron microscopy

The NanoESCA energy-filtered photoemession electron microscope (EF-PEEM) from *Scienta Omicron* and *Focus GmbH* is a new and recently acquired analytical apparatus at the Institute of Experimental Physics. Together with colleagues the author was intensively involved in the setup of the new laboratory facility and the implementation of the NanoESCA system. Within this chapter the measurement concept, the employed technology, and the most relevant measurement modes and strategies will be summarized. A more detailed description and a series of measurement results can be found in the Master's Thesis of Thomas Jauk [61].

As the name already suggests, a PEEM serves as a microscope system, which forms images by means of collecting electrons that were emitted from a sample surface upon irradiation with a light source. A spatial contrast is obtained by local differences in the electron quantity produced by the photoelectric effect. Such differences arise due to variations in e.g. material, phase, crystal orientation, or other properties that affect the electronic structure of the sample surface. The choice of light source depends on the sample and the analytical technique, as discussed later on. The photoemission process can be more intuitively explained by breaking it down to three steps. The first step is the photo-excitation, where an electron is transferred from an occupied initial energy state of the electronic system to a final state above the vacuum level via an optical transition. The probability of a photon to excite an electron is described by the photo-ionization cross section of the initial state. After photo-excitation the electron can move freely in the solid and is, in a second step, with a certain probability transported towards the surface. On the way it can undergo both elastic and inelastic scattering processes, e.g. on other electrons or defects in the crystal, and change its trajectory.

Thereby, it makes a difference regarding the obtained photoelectron spectra (cf. Chapter 2.6.1), if the electron looses energy upon undergoing inelastic scattering events and contributes to the background signal, or if it is not or elastically scattered and contributes to a sharp emission line. The intensity I_0 of the latter type of excited electrons is exponentially damped as a function of the depth of excitation within the solid d, the inelastic mean free path $\lambda(E_{kin})$ in dependence on the kinetic energy, and the emission angle α with respect to the surface normal. Eq. 10 shows the relation to the obtained intensity I [70].

$$I = I_0 \cdot \exp\left(-\frac{t}{\lambda(E_{kin}) \cdot \cos(\alpha)}\right) \tag{10}$$

The energy dependence of λ is, in a good estimation, described by a universal curve for all materials [71]. In the relevant energy range around 10 to 20 eV the inelastic mean free path of an electron is roughly in between 0.1 and 2 nm. In a third and final step, the electron needs to leave the solid by overcoming the surface potential barrier, which depends not only on the material, but also on surface adsorbates and external electrical fields. Electrons with insufficient energy cannot leave the solid resulting in a sharp work function edge in the obtained spectrum [61,70]. Since the whole NanoESCA system is kept at UHV conditions ($\approx 3 \times 10^{-11}$ mbar), unwanted contributions by adsorbates are minimized.

The concept of the NanoESCA system was introduced by *Focus GmbH* together with university partners in 2005 [72]. The already known PEEM technology was extended by the addition of the imaging double energy analyzer (IDEA). A schematic of the NanoESCA with the electrostatic lens system and the IDEA is shown in Fig. 15 in a simplified representation [73]. The basic measuring concept is explained by means of the three different operating modes available with this instrument. The explanations in the following paragraphs are based on Refs. [61,70,73,74]

In PEEM mode, marked with the number 1 in Fig. 15, the system works like any state-of-the-art photoemission electron microscope. The sample is part of the objective and pinned to a fixed potential. To allow for that, the sample holder as well as the sample itself need to be conducting. The emitted electrons from the sample surface are guided towards the microscope column by an applied voltage (usually 12 kV) between the sample and the subsequently positioned extractor. To avoid tip effects that could damage the imaging unit because of high electron intensities (leak current), the sample should also be reasonably flat and clean. The objective, which includes several more electrostatic lenses, is used together with the projection lenses (P12) to set the magnification. In the back focal plane of

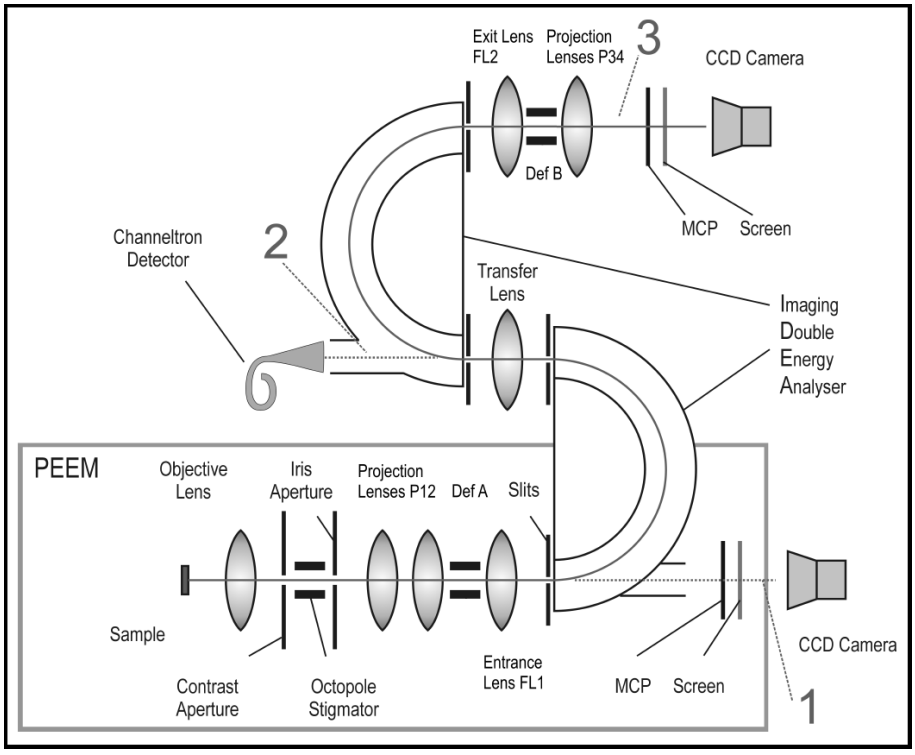

Figure 15: Schematic of the NanoESCA EF-PEEM, showing the electrostatic lens system and the double hemispherical energy analyzer. The three marked operating modes are: (1) PEEM mode (without energy filtering), (2) spectroscopy mode (with energy filtering), and (3) EF-PEEM mode (with energy filtering). Reprinted from Ref. [73].

the objective lens there is a contrast aperture, which allows for a limitation of the angular spread of the collected photoelectrons. By closing the contrast aperture, the spatial resolution can be improved at cost of the overall signal intensity due to the reduced transmission. Because of its position in the back focal plane of the objective lens, the contrast aperture can also be used to select the field of view in momentum space, as discussed later on. The iris aperture, on the other hand, is used to select the effective field of view in real space, e.g. if only a restricted area of the sample should be analyzed. Between the two apertures, an electrostatic octopole stigmator is placed to compensate for lens aberrations like axial astigmatism. An integrated deflection unit allows for the alignment of the optical axis. In PEEM mode P12 projects the final image directly onto the imaging unit, consisting of a multichannel plate (MCP), an array of close packed electron multipliers, and a fluorescent screen, which converts the incoming electrons into a light signal. The produced light is finally detected by the charged coupled device (CCD) sensor of an attached camera and directly sent to the operating software.

For using the spectroscopy mode, number 2 in Fig. 15, the photoelectrons need to be filtered by their kinetic energies. Therefore, they have to enter the first of the two analyzers of the IDEA system. In the energy filtered mode, the P12 lenses are used to retard the electrons towards the analyzer's pass energy (usually around 50 eV) and a deflector (Def A) is used to guide the electrons towards the entrance slit. The entrance lens (FL1), part of the IDEA coupling lens system, forms a reciprocal image at the entrance slit of the first hemisphere, where the electrons are forced on a circular path and separated according to their kinetic energy. Scanning through the kinetic energies is enabled by changing the sample voltage, which directly influences the electron energies. The reachable energy resolution ΔE, shown in Eq. 11, is fixed during the scan since the pass energy of the analyzer E_{pass} is kept constant [72]. It depends on the adjustable width of the entrance slit d, the maximum entrance angle of the electrons with respect to the optical axis α, and the mean radius of the analyzer R.

$$\Delta E = E_{pass} \cdot \left(\frac{d}{2 \cdot R} + \alpha^2 \right) \tag{11}$$

The transfer lens, after the first part of the IDEA, focuses the energy filtered photoelectrons into the channeltron (CT) detector, where they are counted. This allows for the acquisition of spectra presenting the electron intensity as a function of their kinetic energy.

For the EF-PEEM mode, number 3 in Fig. 15, the energy filtering works identical to the spectroscopy mode. Only, the transfer lens now images the electrons on the entrance slit of the second part of the IDEA. This second hemispherical analyzer compensates for dispersive imaging errors of the first analyzer to avoid chromatic aberrations in the final image. Its presence allows for high resolution imaging. After the photoelectrons exit the IDEA, the image is transferred back into real space by the exit lens (FL2), restoring their spatial information. Another deflector (Def B) is used to align the beam and the projection lenses (P34) project it onto the second imaging unit, which is identically built as the first one. As a final result, spatially resolved microscopy images for the adjusted electron energy are obtained.

Because of the two hemispherical analyzers in the IDEA system, the NanoESCA reaches an improved spatial resolutions of down to 30 nm. Though, the operation close to this limit is challenging, it is possible to image nanosized structures and particles. The strongly decreased electron yield at high magnifications is the main problem, since the adjustment of the optical systems is only possible with increased integration times. Even with a well adjusted setup, it is

not possible to directly image the sub 10 nm sized particles synthesized with the helium droplet approach. Still, the NanoESCA can provide valuable information with its integrative spectroscopy techniques, where larger areas on a surface decorated with nanoparticles are measured. In the following, some results obtained from measurements at the NanoESCA are explained in more detail. They are categorized with respect to the employed light sources and operation modes.

2.6.1 Ultraviolet photoelectron spectroscopy

In order to perform ultraviolet photoelectron spectroscopy (UPS) a suitable light source needs to provide photon energies of above 10 eV in the so-called vacuum ultraviolet (VUV). Because for VUV the absorption in air is too strong, the light source is directly connected to the UHV chamber. In the case of the NanoESCA, a helium discharge lamp is used, which provides monochromatic light at two different energies depending on the gas pressure and the applied discharge current: He I at 21.22. eV and He II at 40.81 eV [75]. For the following experiments a photon energy of 21.22 eV is sufficient and the He I mode was used. For UPS, the NanoESCA is operated in the spectroscopy mode, where the photoelectrons are discriminated only by their kinetic energy, but not by their spatial information. The overall electron intensity is detected and evaluated.

In Fig. 16 an exemplary UPS spectrum of a Cu(110) surface is shown, from which the most important features can be deduced. The electron intensity is plotted over the binding energy E_{bind} to ease interpretability. By default, the spectra are recorded with $E - E_F$ on the abscissa, an energy scale relative to the Fermi energy E_F. The spectrum holds a wide range of valuable information on the electronic properties of the sample. The dominating background structure, which includes the broad peak at around -15 eV, is attributed to secondary electrons. As mentioned above, those electrons lost energy by undergoing at least one inelastic scattering event on their way to the sample surface. It is obvious that the secondary electron peak has a steep onset, the so-called low energy cut-off, at about -17 eV. From the photoemission onset the work function of the sample can be estimated by drawing a tangent through the point of maximum incline and intersecting it with the abscissa. Since E_{bind} is plotted, the photon energy of 21.22 eV needs to be added to derive a work function of $\Phi = (4.4 \pm 0.2)$ eV, in good agreement with literature [61, 76]. At the other side of the spectrum around $E_{bind} = 0$ eV a sudden drop in energy associated with the Fermi cut-off is visible. It represents the electrons which are emitted from the Fermi level of the sample and is a sign for its metallic character. Superimposed on the background signal

characteristic features, originating from the valence band of the sample, appear and serve as a fingerprint for the material. The most prominent feature, between binding energies of -2 and -5 eV, is attributed to the 3d band of Cu(110). The less pronounced artifacts between -6 and -11 eV are likely associated with adsorbed species on the surface, like CO or water.

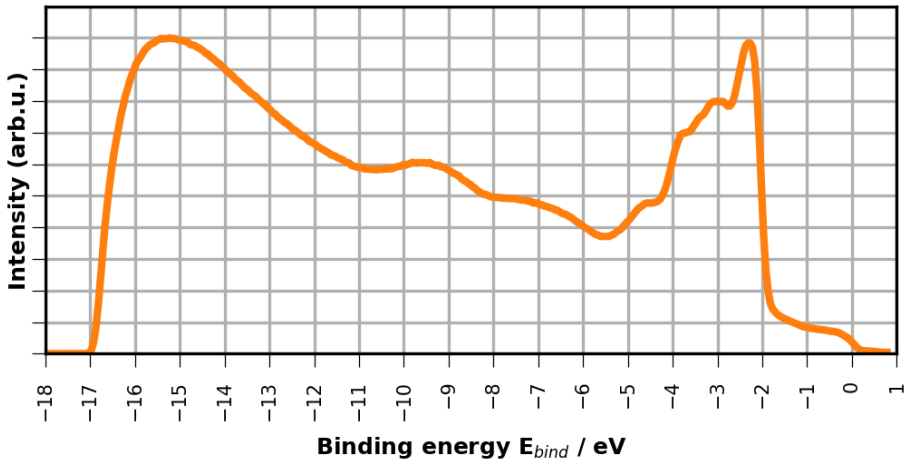

Figure 16: UPS spectrum of a Cu(110) surface obtained with a photon energy of 21.22 eV. The metallic character of the sample is indicated by the pronounced Fermi cut-off. The 3d band at binding energies between -2 and -5 eV can be identified.

Such UPS measurements can also be conducted on nanoparticle samples as shown in Chapter 5, where the Zn 3d levels of Ag@ZnO core@shell particles were investigated and the work function was estimated from the UPS data [3]. There is the obvious drawback that only averaged data over a wider area can be obtained. Especially the work function is expected to vary from particle to particle and even on a single particle's surface, depending on the curvature and size. Still, UPS can give valuable insight and is a promising complementary measurement technique for nanoparticle substrates.

2.6.2 Two-photon photoelectron spectroscopy

Two-photon photoelectron (2PPE) spectroscopy becomes increasingly important in surface science since tunable and pulsed laser system are widely available. It differs from UPS by the choice of light source. Photons with less energy can be utilized and there is no need for UV sources, since the electron must not overcome the vacuum level upon initial excitation. The schematic in Fig. 17 gives an overview of the different pathways leading to the final photoelectron state $|p\rangle$ [77]. The overall absorbed energy of the electron is divided into a contribution

from the pump photon $\hbar\omega_1$ and the probe photon $\hbar\omega_2$. In the direct two-photon ionization process in Fig. 17 (b) the electron absorbs a pump and a probe photon coherently and is directly promoted to the final state $|p\rangle$. A further possible path for the creation of a photoelectron via an intermediate state $|j\rangle$ is shown in Fig. 17 (a). A pump photon can excite an electron directly from the initial state $|i\rangle$ into $|j\rangle$ or, in an indirect way, a photo-excited electron from the bulk continuum can be promoted to the intermediate state [77]. In the latter case, momentum transfer is required e.g. by scattering with a phonon. During the temporal population of $|j\rangle$ a probe photon can be absorbed by the electron and excite it into the final $|p\rangle$ state above the vacuum level. Here, the photoelectron can be collected by the PEEM optics and contributes to the obtained spectrum. Intriguingly, the temporal population of an intermediate state can be investigated by utilizing ultra-fast pump and probe laser pulses in the femtosecond regime. By varying the time delay between pump and probe pulse with an interferometric setup, the temporal evolution of the population in such a state can be deduced. This leads to the experimental field of time resolved 2PPE (TR-2PPE) spectroscopy [77,78].

In the course of this work, 2PPE spectroscopy was used for measurements demonstrating the plasmonic activity of the Ag cores in Ag@ZnO core@shell nanoparticles [3]. The according spectra are presented in Fig. 41 in Chapter 5. In this experiment the second harmonic of the Indigo-S Ti:Sapphire laser from *Coherent* at 410 nm with a pulse duration of 30 ns and a repetition rate of 5 kHz was used as a source for both pump and probe photons. Thereby, a maximum energy of 6.04 eV was provided to the electrons in a two-photon ionization process.

In the future, time-resolved 2PPE and time-resolved PEEM will probably be possible in the upgraded NanoESCA laboratory, where a laser system with pulse durations of only several femtoseconds will be available. This would enable studies on charge carrier dynamics in the samples [79]. Investigations could be conducted e.g. on the dynamics of localized surface plasmons or exciton creation in bulk metals and metallic nanoparticles.

2.6.3 Real and momentum space microscopy

Besides the spectroscopic mode the NanoESCA provides a powerful energy-filtered imaging mode, which allows for a fast switching between real space and momentum space, also called k-space. In k-space mode the lateral angular distribution of the photoelectrons, which is imaged in the back focal plane of the objective lens, is projected onto the screen. To achieve that, the objective lens is focused to infinity and an additional transfer lens is activated in between the objective lens and the projective lenses [74]. The field of view in k-space is regu-

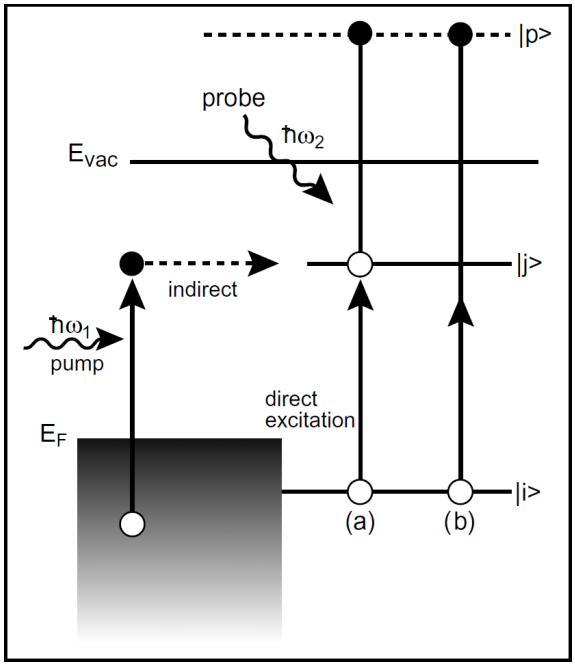

Figure 17: Schematic of different pathways for 2PPE excitation. (a) In a stepwise process an electron can be indirectly excited into an intermediate state $|j\rangle$ from the bulk continuum, which requires a momentum transfer, or directly from an initial state $|i\rangle$ by a pump photon and then further into the final photoelectron state $|p\rangle$ above the vacuum level by a probe photon. (b) An electron is promoted to $|p\rangle$ by direct two-photon ionization without the use of an intermediate state. Reprinted from Ref. [77], with permission from Elsevier.

lated by the size of the contrast aperture, situated in the back focal plane of the objective lens. By closing it, the passing of electrons, which were emitted under higher angles from the surface, is prohibited and the imaged area in k-space is reduced. The iris aperture on the other hand acts as a contrast aperture in k-space enabling higher resolution, while reducing overall transmission.

The presented experimental data in this section provides examples for the potential of the NanoESCA imaging modes and are more thoroughly evaluated in Ref. [61]. Since the visualization of sub 10 nm particles is not possible, there is no direct connection to the scientific articles presented in this thesis. Still, EF-PEEM is an interesting imaging method and once the particles become bigger, it delivers convincing results. This is shown in an acquired image of Ag particles on a polished p-type Si wafer in Fig. 18. The HIS, with a photon energy of 21.22 eV, served as a light source and the energy filter was set to $E - E_F = 4.1$ eV, close to the work function of Ag. Silver was deposited in vast amounts with the

helium droplet approach at source conditions of 20 bar and 4 K for 44 min, which results in big wire-like structures with lengths up to several 100 nm. Intriguingly, after the sample was stored under UHV conditions at room temperature for five days the observed Ag particles were shaped spherically and very evenly distributed on the substrate. This change in shape was attributed to the high mobility of noble metals on the very uniform and flat Si wafer surface and the known tendency of Ag nanowires to break up and change shape already at room temperature [30, 80]. As a result, a mean diameter for the conglomerated bigger nanoparticles of about 110 nm was measured with a wide distribution from 50 nm up to 200 nm [61]. Because of the high contrast to the substrate in the background, the Ag nanoparticles are clearly identifiable in Fig. 18, proving the ability of the NanoESCA to image nanosized structures.

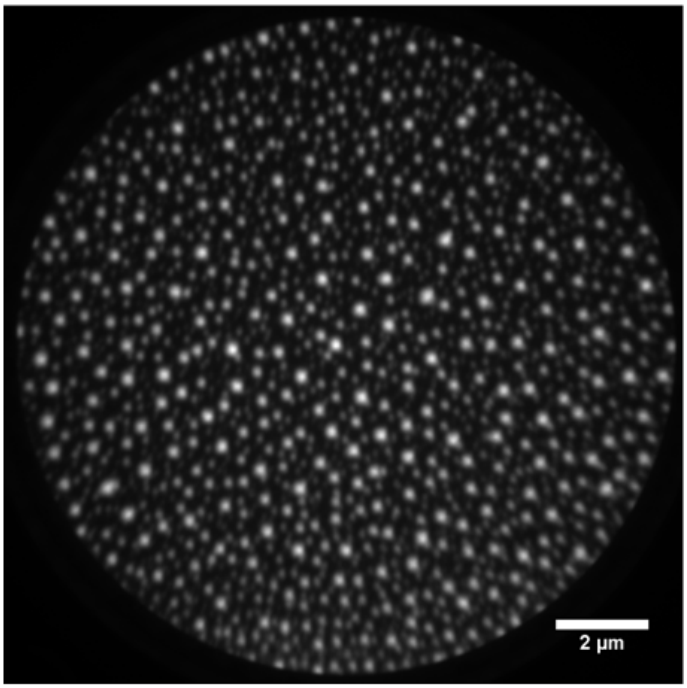

Figure 18: Spherical Ag nanoparticles with diameters between 50 and 200 nm, formed upon breakup of Ag nanowires, on a p-type Si-wafer. The HIS (21.22 eV) was used as photon source with the energy filter at $E - E_F = 4.1$ eV, close to the work function, allowing for a high contrast to the p-Si background.

To show the potential of k-space mode, a Cu(110) crystal was measured to visualize its electronic band structure. This is usually done by angular resolved photoemission spectroscopy (ARPES), where the sample is rotated and a spectrum is acquired for every emission angle. In an EF-PEEM electrons emitted under all accessible emission angles are detected simultaneously. This is a great advantage, since the whole momentum landscape is accessible at once. To obtain spectral

information of the Cu(110) 3d band the energy filter was used to scan $E - E_F$ from 16.00 eV to 19.50 eV in 0.05 eV steps with an acquisition time of 50 s per image. For each energy a whole k-space image was acquired. Afterwards, they were stacked together to form the picture presented in Fig. 19, with a quarter of it removed on the front side to show the 3d band of Cu(110). Further details on the generation of the 3D plot can be found in Ref. [61].

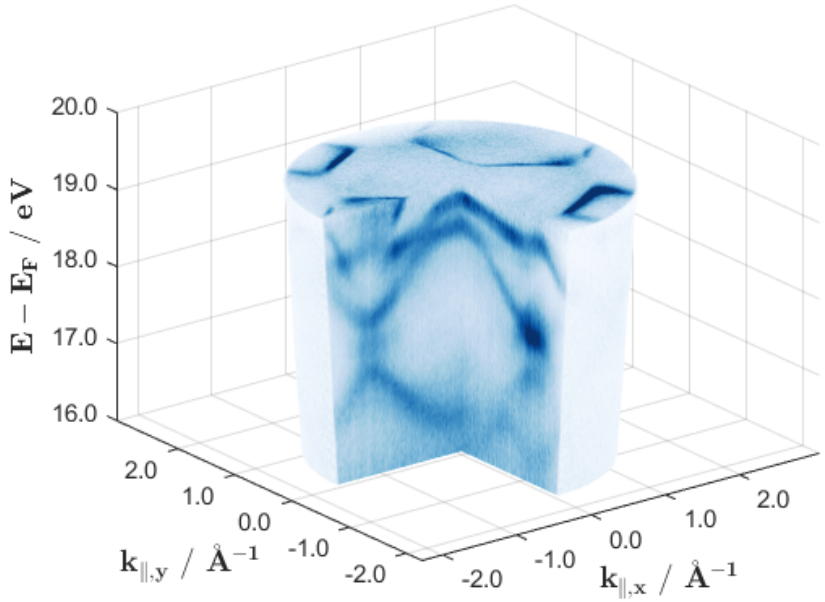

Figure 19: Stacked k-space images showing the Cu(110) 3d band at $E - E_F$ from 16.00 eV to 19.50 eV in 0.05 eV steps. 21.22 eV photons were provided by the HIS and images were acquired for 50 s each with the 1750 μm contrast aperture inserted. Reprinted from Ref. [61].

It should be noted that measurements on nanoparticle samples would not give interpretable results. Because of their arbitrary orientation, an electronic band structure would not be observable in an integrative measurement. Observing single nanoparticles, on the other hand, is not feasible because of the limited resolution and the low intensity. Therefore, also in future experiments k-space imaging will be mostly conducted on metallic surfaces and adsorbed organic molecules. To allow for such experiments, the NanoESCA laboratory is now being equipped with a UHV sample preparation chamber including several evaporation cells for the production of thin metal films and the deposition of molecules onto surfaces. Several analytical methods are also implemented in the new chamber, including low-energy electron diffraction (LEED), quadrupole mass spectrometry (QMS), and X-ray photoelectron spectroscopy. This is a joint project with the

Surface Science Group at the Institute of Physics at Karl Franzens University in Graz. The availability of those additional methods will open up a wide range of new possibilities for experiments at the NanoESCA.

2.7 XUV absorption spectroscopy

The basic principle of absorption spectroscopy was already explained for visible and UV light in Chapter 2.5. When the photon energies are further increased the spectral range of extreme ultraviolet (XUV) is reached. The region of XUV spans from 10 to 124 eV, corresponding to wavelengths of 124 to 10 nm, and is directly followed by the soft X-ray regime from 124 eV to about 10 keV. X-ray and XUV photons posses enough energy to access electronic transitions from core levels of atoms and allow for the study and characterization of the electronic structure of atoms, molecules, or solids.

With the rise of the number of femtosecond laser systems over the past decade, XUV sources are now widely available on the laboratory scale. XUV and soft X-ray pulses can be generated by utilizing the concept of high-harmonic generation (HHG) [81, 82] with the additional advantage that their properties, like pulse duration or polarization state, can be directly controlled via the driving laser. Furthermore, the XUV pulses can be generated with pulse durations down to the attosecond regime, leading to new experimental techniques like transient absorption spectroscopy [83]. Therefore, HHG sources have attracted considerable interest in the scientific community in recent years. The concept of HHG, a nonlinear optical process, will be explained in more detail in this paragraph, based on Refs. [81, 82]. A strong-field laser pulse, typically produced with a near infrared Ti:Sapphire femtosecond laser system, is focused in a gas phase target, e.g. neon. The HHG process is typically described by the three-step model [84], as illustrated in Fig. 20 in a set of schematics [82].

As the laser pulse arrives at a gas atom (schematic 1) the high peak field strength bends its ionization potential and, thereby, enables tunnel ionization. The electron is freed from the atom and accelerated away from it by the laser field during the first half cycle. As the photon propagates further, the acceleration is reversed once the electron feels the second half cycle of the laser pulse and the potential is tilted the other way (schematic 2). If the timing between the laser field and the electron ejection is favorable, a fraction of the accelerated electrons finally collide and recombine with their parent atoms in a so-called rescattering event. Upon recombination the electron releases its excess energy, which equals the ionization energy of the target gas plus an additional amount

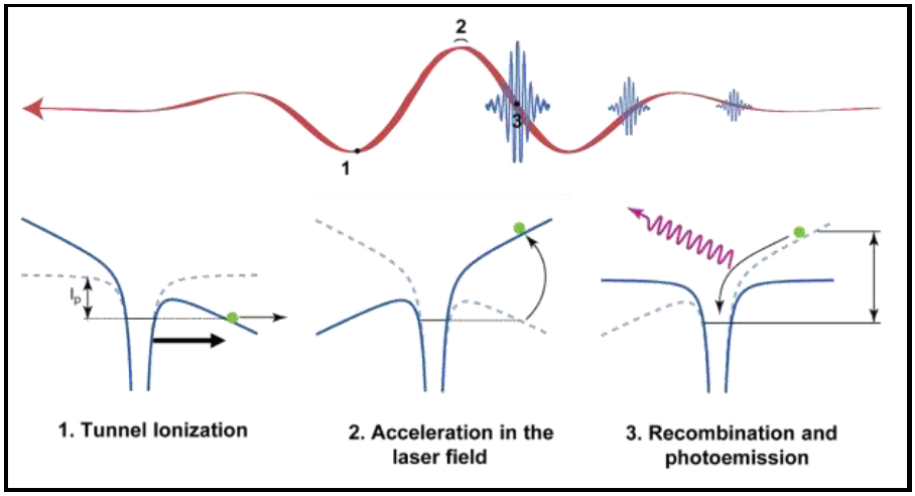

Figure 20: Schematic representation of the three essential steps for high-harmonic generation in a gas phase target. On top, the incident laser field (red) and the generated high energy light (blue) is depicted. In the lower row the processes occuring at the three marked positions are explained in detail. The green circle represents the electron, while the distorted nuclear potential is drawn in blue. Reprinted from Ref. [82].

of kinetic energy obtained from the laser pulse during acceleration (schematic 3). For this additional amount of kinetic energy E_{kin} a maximum value, shown in Eq. 12, was found [81].

$$E_{kin} \leq 3.17 \cdot U_P \tag{12}$$

The factor 3.17 was empirically determined and U_P is the ponderomotive energy, which is the cycle averaged quiver energy of a free electron in an applied electromagnetic field. In Eq. 13 U_P is deduced from the elemental charge e, the field amplitude E_0, the electron mass m_e, and the field frequency ω_0 [82].

$$U_P = \frac{e^2 \cdot E_0^2}{4 \cdot m_e \cdot \omega_0^2} \tag{13}$$

Because of the high ionization energy and the additional kinetic energy, the recombining electrons emit bursts of XUV radiation with very short pulse duration, reaching down into the attosecond regime. Since the whole HHG process is temporally and spatially linked to the phase of the fundamental laser, it results in a coherent laser-like beam. The major drawback of HHG sources is the very low conversion efficiency of about 10^{-5}.

XUV generation by means of HHG has the obvious advantage of providing a convenient table top radiation source, which enables laboratory scale experiments. The schematic of a setup for transient XUV absorption spectroscopy at the Lawrence Berkeley National Laboratory in California is shown in Fig. 21 and explained according to Ref. [85]. The 775 nm NIR laser pulses, produced by a commercial Ti:Sapphire femtosecond laser system, are split by a 50/50 beam splitter. One of the resulting beams is serving as the pump laser and guided through a delay stage and over a recombination mirror to the sample, a cell filled with gaseous Xe. The second part of the beam reaches the HHG cell filled with Ne gas, where the XUV spectrum of overlapping harmonics with energies from 48 to 72 eV is generated. Residual light from the driving laser is suppressed by the Al filter. The XUV probe pulse is overlapped with the NIR pump pulse in the target Xe cell to enable pump-probe measurements. For transient absorption spectroscopy a time delay can be introduced between the pulses by adjusting the delay stage accordingly. For the acquisition of a spectrum the energy selection is achieved through dispersion by a grating and the signal is recorded by the detection unit. The obtained transmitted intensity is a function of the XUV photon energy, as well as of the time delay. Transient absorption experiments on the described setup, were, e.g., conducted on Xe [85], bromoform ($CHBr_3$) [86], 1,2-dibromoethane [87], selenophene (C_4H_4Se) [88], or ferrocene [89].

An ongoing cooperation with the Chemical Dynamics Group at the Lawrence Berkeley National Laboratory in California made it possible to conduct absorption spectroscopy experiments with ultrashort XUV pulses on oxidized cobalt nanowires produced with the helium droplet approach in Graz [4]. The measurements were performed at the described experiment with several changes to the setup. Since no time dependence was investigated, a pump probe setup was not necessary and only the XUV pulses were guided through the sample. The target is usually available in its gas phase, but the CoO nanoparticles were deposited on 10 nm thick Si_3N_4 substrates. Therefore, the system was accordingly adapted, but further improvements can certainly be thought of for future measurements. The results obtained from the CoO particles showed, for the first time, conclusively that the experimental technique is feasible for sub-monolayer nanoparticle samples on thin solid substrates. More detailed information on the experiment can be found in Chapter 6, where the recorded spectra are depicted in Fig. 49.

2.8 SQUID magnetometry

The above mentioned analytical methods mostly concentrate on finding out about the shape, morphology, or chemical composition of the nanoparticles. Yet another

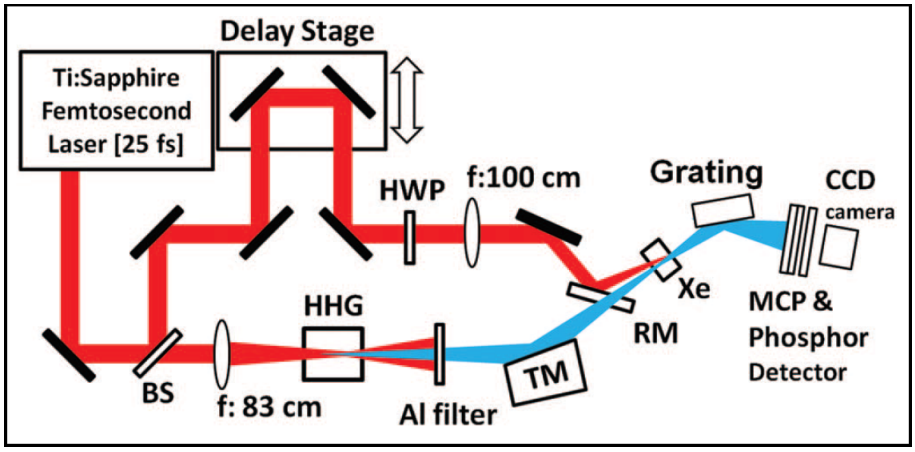

Figure 21: Schematic representation of an XUV transient absorption experiment on Xenon (Xe). The red beam represents the incident NIR femtosecond pulse laser at 775 nm, the blue one the generated XUV light. The setup contains a beam splitter (BS), a delay stage, a half wave plate (HWP), a high-harmonic generation cell (HHG), an Al filter, a toroidal mirror (TM), a recombination mirror (RM), several lenses, and a grating. The detection unit comprises a microchannel plate (MCP), a phosphor detector, and a charge-coupled device (CCD) camera. Reprinted from Ref. [85], with the permission of AIP Publishing.

interesting aspect are magnetic properties of those species. In some preliminary experiments the application of a superconducting quantum interference device (SQUID) magnetometer was tested to cover this aspect. Measurement data from SQUID magnetometry experiments are not part of the publications that form the main body of this work, but are of interest beyond the scope of this thesis and were part of the author's work on nanoparticle analysis. Therefore, a summary on the method and first results of measurements on nanoparticles are presented in the following.

A SQUID magnetometer is a highly sensitive measurement device for magnetic fields invented in the 1960s [90]. The measurement method depends on the predicted Josephson effect [91] and its experimental realization in a so-called Josephson junction [92], both published only a couple of years prior. The Josephson junction is a particularly interesting example of the tunneling effect. If two superconductors are separated by a thin isolating barrier only a tunnel current can flow. This current is based on Cooper pairs [93], which originate in a quantum effect, pairing electrons because of an elastic distortion of the ion lattice in a metal by a passing electron, as is schematically shown in Fig. 22. In a simple picture, the resulting accumulation of positive charge forms a dip in the potential and,

thereby, attracts a second electron. The two electrons pair up in a weak and long range interaction with an extent in the range of hundreds of nm, allowing for the previously addressed tunneling through a thin barrier [56]. Since the interaction energy is in the meV regime, a significant number of Cooper pairs may only exist at low temperatures.

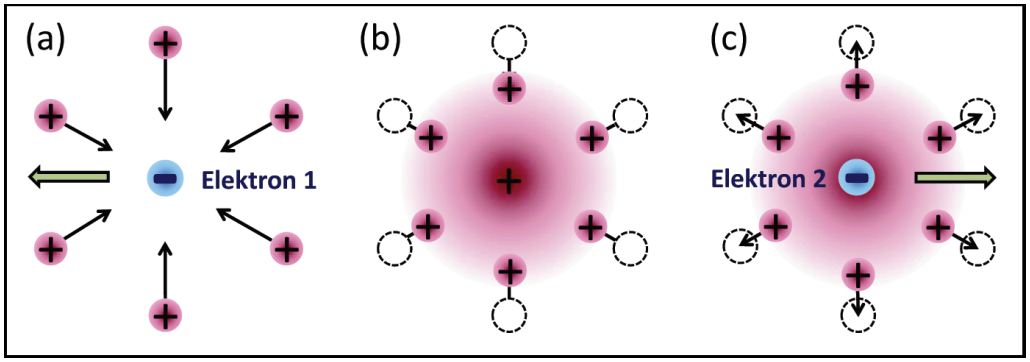

Figure 22: The schematic shows in three steps how a Cooper pair forms. (a) The ion lattice is distorted by the passing electron 1 and the positive ions are moving towards the center. (b) After the electron already moved through, the positive space charge in the center persists, since the ions react on a longer time scale. (c) Due to this potential dip a second passing electron is attracted and paired in a weak and long range interaction with electron 1. Reprinted from Ref. [56].

The following information on the composition and working principle of a radio-frequency rf-SQUID magnetometer is based on Refs. [56, 94]. A SQUID basically consists of a superconducting ring with a Josephson junction, which needs to be cooled below the critical temperature of the superconductor, e.g. with liquid helium. Quantum effects allow only for a quantized magnetic flux within the ring. If the external magnetic fields change, the superconducting current through the ring varies to compensate for these changes. Thereby, the high frequency impedance of the system changes as well. This is read out via inductive coupling to a resonant tank circuit at frequencies of several 10 MHz. A feedback system compensates the external flux variations by producing a magnetic field itself. The measured quantity is the current through the compensation coil. Note that only changes of the magnetic field through the superconducting ring can be recorded. Therefore, the magnetic sample needs to be moved through the ring, which is done with a constant velocity.

In a cooperation with the Institute of Materials Physics (IMP) at Graz University of Technology a MPMS-XL-7 magnetometer (*Quantum Design Inc.*) was accessible for conducting SQUID magnetometry measurements on NiO nanopar-

ticles. For a proof-of-concept measurement, synthesis conditions with the helium droplet approach were optimized for high mass output at a temperature of 10 K and a helium pressure of 60 bar. Since the goal for this experiment was a high surface coverage and not that the particles are distinguishable, a deposition time of 6 hours was chosen. A cleaned strip of a silicon wafer with a length of 90 mm and a width of 6 mm was used as substrate. It is of importance that the substrate is not cut or worked with metallic tools, since already very small residues of metal can mask the magnetic signal from the sample. Also the length of the substrate is important because it should not leave the measurement region of the SQUID, when it is moved through the apparatus. To cope with a 90 mm sample the transfer system had to be adapted accordingly. Before the nanoparticle deposition, the empty substrate was measured to allow for a subsequent background correction. After the deposition the sample was transported to the SQUID laboratory and, thereby, exposed to ambient air, allowing for an oxidation of the Ni. Though the IMP has experience with measurements on nanoparticles or monolayers of metals [95, 96], usually there are bigger particles or more material at hand. An estimation of the deposited mass of Ni for this experiment yields approximately 0.5 μg in total. The measurement data was evaluated by Markus Gößler from the IMP, who provided the plot of the magnetic moment over temperature shown in Fig. 23.

It should be mentioned that results from SQUID magnetometry measurements are mostly given in Gaussian units. The conversions are as follows: 1 Oe equals 79.58 A/m for the magnetic field H and 1 emu equals 10^{-3} Am^2 for the magnetic moment m. The main conclusion from Fig. 23 is that measurements of the magnetic properties of nanoparticles with a SQUID magnetometer are feasible. Still, the obtained magnetic moments between 5 and 8 $\times$ 10^{-6} emu are close to the resolution limit of the SQUID magnetometer. Thus, the measurement data behind this representation is rather noisy and further evaluation, e.g. the generation of hysteresis plots, is hardly possible. To discuss the plotted data in more detail, the black points show the magnetic moment as function of temperature for zero field cooling (ZFC). In this measurement mode no magnetic field is applied during the cooling of the sample from room temperature down to 4 K, then the magnetic field of 500 Oe is switched on and the sample is measured while it is heated. Afterwards, the sample is measured while being cooled down again with the magnetic field still applied, resulting in the red data points of the field cooling (FC) mode. The trend of the FC points at low temperatures, before a maximum is reached around 30 K, suggests a small antiferromagnetic contribution from the sample. This is probable, since at least the outer shell of the nanoparticles consists of NiO, which is antiferromagnetic. Further information, that was not

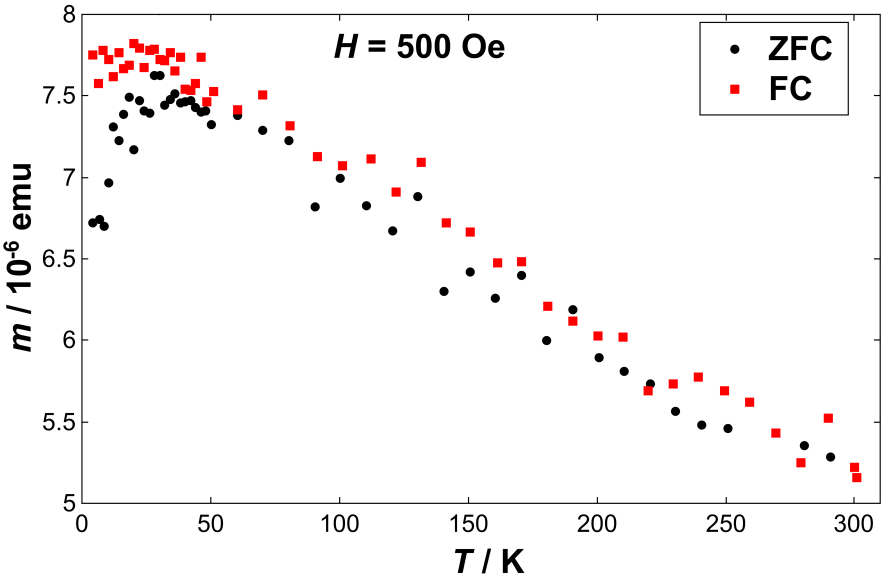

Figure 23: Background corrected temperature dependent magnetic moment measurements of a sub-monolayer of NiO nanoparticles on a silicon wafer at a magnetic field of 500 Oe. The black data points correspond to the zero field cooling (ZFC) and the red ones to the field cooling (FC) measurement scheme. The overall magnetic moment lies in between 5 and 8 $\times$ 10^{-6} emu, close to the resolution limit of the SQUID magnetometer. Provided by Markus Gößler from the IMP.

extracted for this measurement, but is principally accessible, concerns the size distribution of the nanoparticles. An estimation on their diameters can be made from the position of the maximum in the ZFC data.

The magnetic measurements will be continued in future experiments, but a focus needs to be put on an improvement of the signal to noise ratio. To achieve that, there are two possible routes: An increase in deposited mass would certainly help, but the closer the nanoparticles are situated on the substrate surface, the more likely it becomes for them to agglomerate or merge. In a next step, the second route will be tried by choosing a material with a higher magnetic moment than Ni. A promising candidate is Co, which was already used in the helium droplet apparatus in past experiments [4,97].

3 Ultra-thin h-BN Substrates for Nanoscale Plasmon Spectroscopy

The content of this chapter corresponds to the following peer reviewed and published scientific paper:

> "Ultra-thin h-BN substrates for nanoscale plasmon spectroscopy" by **Alexander Schiffmann**[1], Daniel Knez[2], Florian Lackner[1], Maximilian Lasserus[1], Roman Messner[1], Martin Schnedlitz[1], Gerald Kothleitner[2], Ferdinand Hofer[2], and Wolfgang E. Ernst[1] in *Journal of Applied Physics* **125**, 023104 (2019).
> https://doi.org/10.1063/1.5064529

The author of this doctoral thesis contributed to the publication in the following ways:

- Design and execution of the experiment
- Preparation of the substrate
- Synthesis of the nanoparticles
- Assistance in recording of the electron microscopy data
- Evaluation and interpretation of the data obtained by electron microscopy
- Literature research
- Authorship of the manuscript

All co-authors were engaged in the preparation and publication process of this paper. Their affiliations and a short recapitulation of their major contributions are given below:

Daniel Knez:
Experimental design, substrate preparation, recording of the electron microscopy data, and editing of the manuscript.

Florian Lackner:
Scientific advice, assistance with the experiments, funding, and editing of the manuscript.

[1]Institute of Experimental Physics, Graz University of Technology, Petersgasse 16, A-8010 Graz, Austria

[2]Institute of Electron Microscopy and Nanoanalysis & Graz Centre for Electron Microscopy, Graz University of Technology, Steyrergasse 17, A-8010 Graz, Austria

Maximilian Lasserus:
Assistance with the experiments.

Roman Messner:
Assistance with the experiments.

Martin Schnedlitz:
Assistance with the experiments.

Gerald Kothleitner:
Supervision and funding for electron microscopy.

Ferdinand Hofer:
Supervision and funding for electron microscopy.

Wolfgang E. Ernst:
Scientific advice, supervision, funding, and editing of the manuscript.

The authors of this publication gratefully acknowledge additional support provided by the Austrian Science Fund (FWF) under Grant No. P30940-N36 and NAWI Graz.

Reproduced from: "Ultra-thin h-BN substrates for nanoscale plasmon spectroscopy" by Alexander Schiffmann, Daniel Knez, Florian Lackner, Maximilian Lasserus, Roman Messner, Martin Schnedlitz, Gerald Kothleitner, Ferdinand Hofer, and Wolfgang E. Ernst. *Journal of Applied Physics* **125**, 023104 (2019), with the permission of AIP Publishing.

3.1 Abstract

Probing plasmonic properties of surface deposited nanoparticles with high spatial resolution requires the use of a low absorption support. In this work, ultra-thin hexagonal boron nitride (h-BN) flakes are employed as substrates for scanning transmission electron microscopy (STEM). The thickness of only a few atomic layers, the flat surface, and the large bandgap provide a unique set of properties, which makes h-BN ideally suited for high resolution plasmon spectroscopy by means of electron energy loss spectroscopy (EELS), especially for small nanoparticles. A facile fabrication process allows the production of h-BN substrates with a thickness of only a few atomic layers. The advantages of h-BN, especially for the low-loss energy region of EEL spectra, are shown in a direct comparison with a silicon nitride (SiN_X) substrate. Furthermore, results of the investigation of localized surface plasmon resonances (LSPR) of Ag and Ag@Au core@shell nanoparticles in the sub-20 nm size regime are presented, confirming the advantages of the fabricated substrate for LSPR mapping. The plasmonic nanoparticles were assembled utilizing the helium nanodroplet synthesis approach, which allows for a very soft deposition and the preservation of the integrity of the ultra-thin substrate. Moreover, it provides a completely solvent and surfactant free environment for the assembly of tailored nanoparticles.

3.2 Introduction

The advent of 2D materials is opening up exciting new prospects in a broad diversity of fields. Besides graphene, hexagonal boron nitride (h-BN) represents a particularly interesting material, which has already been used for applications in optics [98, 99], catalysis [100, 101], and microelectronics [102–104]. Here we demonstrate that ultra-thin h-BN can be utilized for localized surface plasmon (LSP) spectroscopy on the nanoscale by exploiting its electronic properties and the flat, two-dimensional structure [105]. We present results from the fabrication of h-BN substrates and their application for high resolution LSP spectroscopy, performed inside a scanning transmission electron microscope (STEM) by means of monochromated electron energy loss spectroscopy (EELS).

In recent years the field of plasmonics was greatly influenced by the appearance of new imaging methods based on EELS, providing access to spatially resolved localized surface plasmon resonance (LSPR) maps, which led to insights into the dependency of LSPRs on e.g. particle size, particle shape and inter-particle distance [106–112].

A LSP emerges in metal particles with sizes smaller than the wavelength

of the incident light, where the surface plasmon (SP), a coherent oscillation of the conduction band electrons in the metal, is confined to the small volume of the nanoparticles [113]. At the right excitation frequency the oscillation of the electrons is in resonance with the incoming light leading to strongly enhanced fields in the vicinity of the particle surface [114]. The possibility to image and directly assign LSPRs to certain sites on nanoparticles, in combination with the improved resolution of state-of-the-art STEMs, is an essential contribution towards a better understanding of plasmonic properties on the nanoscale. The increasing interest into imaging methods for LSPRs of nanostructures goes hand in hand with a rising attention for the field of plasmonics. A well established application exploiting the localized field enhancement is surface-enhanced Raman spectroscopy (SERS), where the Raman signal is strongly increased, if the molecule under investigation is situated on a plasmonic particle and the Raman laser is tuned to the LSPR of the functionalized particle [115]. There is a wide range of further promising applications for nanoparticles and nanostructures with plasmonic properties [116], e.g. in sensor technology, especially in medicine and molecular biology [117], and in catalysis and photocatalysis [118].

In the present work we show that by using a h-BN substrate for EELS measurements the background signal for the acquisition of LSPR maps in the low-loss energy region close to the zero-loss peak (ZLP) is lowered significantly compared to commercially available silicon nitride (SiN_X) substrates. The advantage of h-BN arises from its intrinsic property of being an indirect bandgap semiconductor with a bandgap of 5.955 eV for the bulk [119] and 6.07 eV for a single atomic layer [105], providing high transparency in this energy range. Furthermore, the fabricated h-BN flakes exhibit thicknesses down to only a few atomic layers ($\approx$ 0.32 nm per atomic layer [105]), which is responsible for the low background signal in the acquired EEL spectra. To demonstrate the applicability of the h-BN substrates, EEL spectra were recorded for Ag and Ag@Au core@shell particles and further processed to extract spatially resolved LSPR maps.

For the fabrication of plasmonic nanoparticles we employed the helium nanodroplet synthesis method, which is based on the formation of particles in the solvent and surfactant free environment of liquid helium droplets. Additionally, it has been shown that the cold environment (0.37 K) [17, 18] allows for the production of tailored core@shell particles [50]. For the present study we produced Ag and Ag@Au nanoparticles, however, due to the characteristics of the synthesis approach an unprecedented variety of elements in various combinations can, in principle, be utilized for the nanoparticle preparation. A further unique feature of the helium droplet approach, providing interesting opportunities for future experiments, is the possibility to synthesize nanowires by simply adjusting the helium

temperature and thereby forming larger droplets containing vortices [80,120,121].

3.3 Experimental

3.3.1 Preparation of the h-BN substrates

The h-BN STEM substrates were fabricated using a commercially available single-layer h-BN film grown on both sides of a 20 μm thick copper foil (Graphene Supermarket) by means of chemical vapor deposition (CVD) [105, 122]. As support for the h-BN film commercially available holey carbon STEM support grids (Quantifoil R2/1, 200 mesh) with a gold mesh were chosen. For the transfer of the h-BN film onto the grids a facile and reproducible approach was employed.

A part of the Cu foil containing the h-BN film matching the size of the support grid was cut off with a razor blade. The grid was carefully positioned on top of the Cu foil with the holey carbon facing the h-BN. A pair of self-locking tweezers were used to fixate the assembly, which was subsequently immersed into a solution of 4 g ammonium peroxydisulphate (APS) (Carl Roth GmbH, purity $\geq$ 98%) in 50 ml of deionized water. The solution was heated to 50°C and constantly stirred. After thirty minutes in the solution, the Cu foil was completely dissolved and the h-BN film was adhesively conjoined to the support grid. The tweezers were carefully extracted from the solution, the grid with the h-BN substrate was rinsed with deionized water and dried over a hot plate at 50°C.

Concerning this preparation approach several critical points are influencing the quality of the obtained h-BN substrates. During the extraction of the grids from the APS solution and the rinsing, the fragile holey carbon layer of the support can be damaged easily. The process allows for good reproducibility and yields thin h-BN flakes, which partially cover the STEM support grid. Note that there are differences in flatness and thickness of the h-BN flakes. The areas with highest quality should be used for STEM and EELS experiments and are best selected *in situ*.

3.3.2 Nanoparticle synthesis

The employed Ag and Ag@Au nanoparticles were fabricated employing superfluid helium nanodroplets (He_N) as an inert synthesis environment [25,28,123]. Details of the helium droplet apparatus may be found elsewhere [124]. In short, gaseous helium with a purity of 99.9999% at a stagnation pressure of 20 bar is cooled down to temperatures of only a few Kelvin using a closed-cycle refrigeration unit (Sumitomo, RDK-408D2) and expanded into high vacuum (base pressure

$\approx 10^{-5}$ mbar) through a 5 μm diameter nozzle. The adiabatic expansion results in a beam of superfluid He_N with an internal temperature of 0.37 K and droplet sizes that can be controlled by the temperature of the gaseous helium [17, 18]. For the experiments discussed here, the helium was cooled to 6.7 K, leading to He_N diameters of around 130 nm with a mean number N of about 5×10^7 He atoms [125]. The collimated beam is passing through a second chamber (base pressure $\approx 10^{-7}$ mbar) where high purity metals are evaporated in two resistively heated pickup cells composed of aluminium oxide coated tungsten baskets. Upon contact, the He_N are doped with the evaporated atoms, which agglomerate inside the droplets and form clusters. The released binding energy is dissipated by the evaporation of He atoms, thereby decreasing the droplet size and attenuating the He_N beam [27]. The setup with two consecutive pickup cells enables the fabrication of core@shell clusters by sequential doping with two materials [6]. For this work plain Ag and Ag@Au nanoparticles were produced. At the above mentioned conditions the particles are composed of several thousand atoms and are forming Ag ellipsoids with diameters of 10 to 15 nm and Ag@Au rods with a width of 7 nm and a length up to 20 nm.

The He_N beam is finally terminated on the h-BN STEM substrate inside a third chamber at UHV conditions (base pressure $\approx 5 \times 10^{-10}$ mbar). Upon impact the clusters are cushioned by the surrounding helium and keep their shape due to the soft landing conditions [33–35]. During the transfer to the STEM the samples are exposed to ambient air for a short period of time.

3.3.3 EELS and EDS acquisition

The analysis of the h-BN substrate and the nanoparticles was conducted with a probe-corrected FEI Titan^3 60-300 STEM with an X-FEG field emission source operated at a beam energy of 60 keV. The microscope is equipped with a Gatan Quantum imaging filter (GIF) for the acquisition of EEL spectra and a FEI Super-X four-quadrant detector for energy dispersive X-ray spectroscopy (EDS). The energy spread of the ZLP was optimized to a full width at half maximum (FWHM) of 180 meV, the collection semi-angle was adjusted to 16.1 mrad and the convergence semi-angle to 15.6 mrad. The operating voltage of 60 kV was chosen to prevent both the very thin substrate and the nanoparticles from damage by the electron beam. Higher beam energies have the disadvantage of inducing movement and even structural changes [5]. While the operation at 60 kV effectively increases the scattering cross-section and therefore enhances the EEL signal, it has the drawback of decreased resolution. The dwell time per pixel was set to 2.4 μs for high-angle annular dark field (HAADF) images and to 2 ms for all EEL

spectra, whereas the size of the spectrum images was adapted for each individual acquisition.

3.3.4 EELS data processing

The spatially resolved raw data collected by EELS measurements in the STEM is processed with an algorithm programed in Python 3.6.1 and containing the HyperSpy 1.3 multi dimensional data analysis toolkit [126]. The background modeling of the ZLP aligned spectra is realized in an empiric way by integrating a greater number of spectra from the recorded background and further smoothing by applying a Savitzky-Golay moving average filter [127]. The acquired background data is subsequently subtracted from the measured data. This course of action is chosen in order to improve the quality of the evaluation of the low-loss energy region in close proximity to the ZLP. Note that in the case of nanoparticles the yield of electrons interacting with the sample is typically very low. The processed data is smoothed employing a Savitzky-Golay filter [127] and depicted in maps showing the LSPRs of the nanoparticles spatially resolved. The energy resolution for those maps is determined by the FWHM of the corresponding ZLPs.

3.4 Results and Discussion

3.4.1 Properties of the h-BN substrate

Figure 24 (a) shows a HAADF image of a h-BN flake on top of the holey carbon support grid with the synthesized nanoparticles on the surface. The h-BN flake appears to be uniform over the whole imaged area with only some variations in the thickness visible as bright bands in the image. These areas originate from the preparation process when layers of h-BN fold over each other, however, since they are locally contained they do not pose a problem for the applied analytical methods. In Figure 24 (b) a detail of the substrate is depicted where the different species of nanoparticles are visible. The He_N synthesis conditions were chosen such that the deposited Ag@Au core@shell particles have an elongated, rod-like shape. The Ag particles, on the other hand, tend to constrict and form spheres and ellipsoids after they are deposited on the substrate [80]. This peculiarity allows for a clear distinction between the produced species even without analytical methods.

Figure 25 (a) shows an EEL spectrum demonstrating that the substrate consists of boron nitride. The spectrum was obtained by summing up the individual EEL spectra from the region marked by the green frame in Figure 24. The vertical

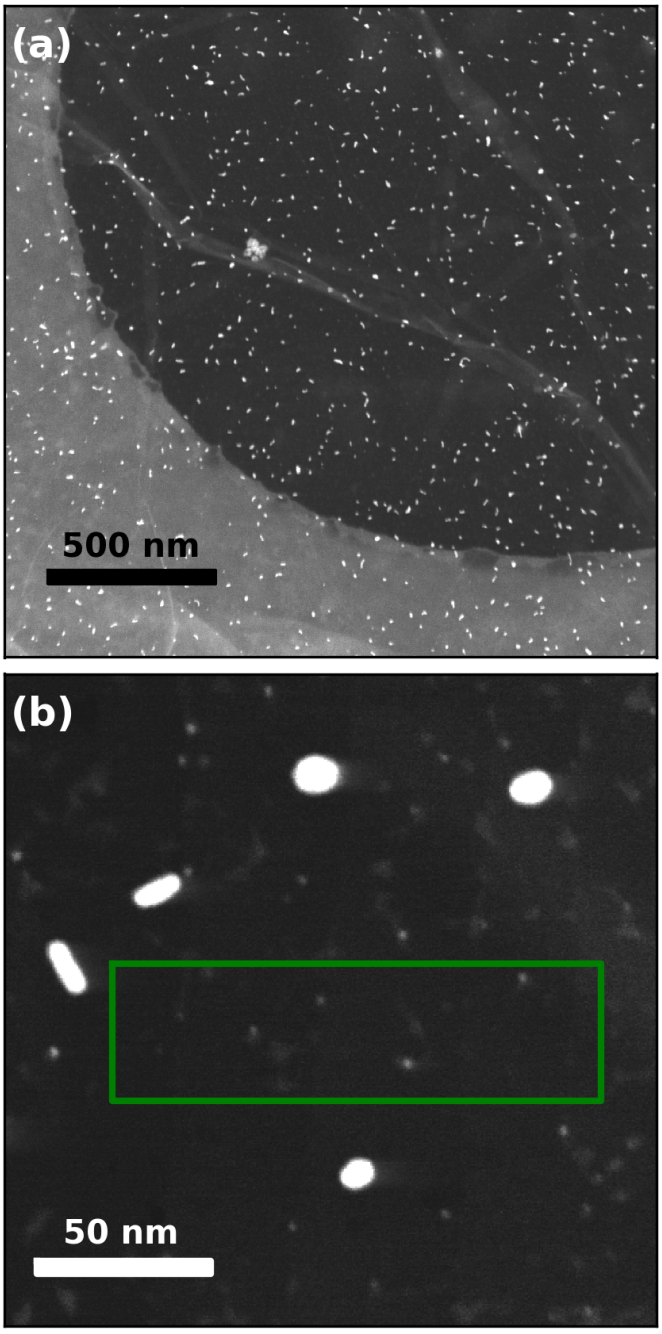

Figure 24: (a) HAADF image of the h-BN substrate situated on the holey carbon support covered with Ag and Ag@Au nanoclusters produced with the He nanodroplet synthesis approach and (b) a closer view on the substrate with nanoparticles showing ellipsoidal (Ag) and rod-like (Ag@Au) shapes. The green frame marks the area from which the spectra in Figure 25 and Figure 26 were obtained.

axis shows the number of electrons arriving at the detector after having lost the amount of energy displayed on the horizontal axis by interacting with the sample. From the shape of the spectrum conclusions on the composition of the sample can be drawn. The high-loss region of the integrated, ZLP position corrected spectrum displays the characteristic edge structure of h-BN with the boron K-edge at 188 eV and the nitrogen K-edge at 401 eV [128]. Strikingly, the spectrum shows no evidence for the occurrence of carbon (K-edge at 284 eV) on the sample, which is beneficial for the acquisition of EEL spectra from nanosized samples. The lack of carbon and therefore of hydrocarbons and other organic residues indicates that the h-BN transfer process, though being quite facile, produces very clean substrates. Furthermore, it demonstrates the quality of the He_N synthesis approach, which provides a solvent and surfactant free way for the deposition of tailored nanoparticles.

However, the main reason for using h-BN as substrate for plasmon spectroscopy on the nanoscale is its characteristics in the low-loss energy region. In Figure 25 (a) the low-loss region up to 7 eV of electron energy loss is depicted. It shows only a low background signal originating from the substrate between the outskirts of the ZLP and the bandgap energy of h-BN, which is marked with a vertical orange line at 6.07 eV [105]. The electronic structure of h-BN with its wide bandgap allows for an increased permeability for electrons in a spectral region where LSPRs of metallic nanoparticles are typically occurring. An important aspect that further contributes to the low background is that the h-BN substrate is very thin, consisting of only a few atomic layers. For thin substrates there is only little interaction with the electron beam and the signal originating from phonon scattering is reduced, leading to a narrowing of the ZLP. Even though the ZLP width is positively influenced by the h-BN substrate, it is still one of the major challenges in the analysis to properly account for its impact on the EELS low-loss signal. The spectrum indicates that the tail of the ZLP still affects the background in the depicted low-loss region. Nevertheless the lowering of the background signal by using ultra-thin h-BN substrates provides a great improvement for the detectability of plasmon signals from nanosized particles.

In Figure 25 (b) the h-BN spectrum is directly compared to an EEL spectrum of a commercially available 5 nm thick SiN_X substrate (Plano GmbH, silicon nitride membrane 5 nm + C, prod.no. NTUS100A05L) shown in magenta. The spectra were obtained under the same acquisition conditions and the SiN_X spectrum was scaled to the ZLP height of the h-BN spectrum to enable a comparison. It can be seen that almost over the whole depicted range from 1.5 eV to 30 eV the SiN_X signal rises above the h-BN signal. In a narrow section below 2.5 eV, close to the ZLP, the SiN_X gives a lower background signal, however, in the bandgap region

of h-BN below 6 eV the h-BN signal clearly shows fewer electron counts. This energy window is most important for plasmon spectroscopy, since nanoparticles made of e.g. Ag, Au, Pt, Pd, Cu, W, Ti, Cr, Rh, In, Mg or Ga feature plasmon peaks in between 2 eV and 6 eV [129]. Therefore, the fabricated h-BN substrates are excellently suited for an application in plasmon spectroscopy. The subsequent broad peak in the h-BN spectrum at around 7.2 eV can be assigned to the π plasmon of h-BN [130] and dominates the region between 6 eV and 9 eV. For the rest of the spectrum between 9 eV and 30 eV the SiN_X signal is defined by the very broad feature around 22.5 eV representing the bulk plasmon of SiN_X, which peaks between 20 eV and 25 eV depending on the nitrogen content of the material [131, 132]. In this whole region h-BN provides a lower background signal, especially between 9 eV and 15 eV before the h-BN $\sigma + \pi$ plasmon with a double peak at around 18 eV and 23 eV [130] leads to another increase in the h-BN signal. Nevertheless, the background signal generated by h-BN at these higher energies is still superior compared to the SiN_X signal and the far reach of the advantageous low background opens up other possible applications besides the employment as substrate for plasmonic nanoparticles: Several chemical elements, which are usually identified by their edge structure in the high-loss region, also have less pronounced major edges at lower loss energies such as the $M_{2,3}$-edges of K at 18 eV and Ca at 25 eV, the $N_{2,3}$-edges of Y at 26 eV and Zr at 29 eV or the $O_{2,3}$-edges of Ba at 15 eV and Nd at 21 eV. h-BN substrates would provide an exceptional advantage for the highly sensitive detection of these species. Moreover, a wide range of other materials feature interband transitions in the considered energy range, which can also be accessed by EELS [133, 134]. The detection and classification of both, low-loss edges and interband transitions, could be facilitated by the use of low background substrates.

To exploit all the advantages of h-BN substrates for EEL spectroscopy it is necessary to produce very thin substrates containing, in the best case, even single layered areas. It is inherent to the presented transfer process of the commercially available h-BN film onto the STEM support that the atomic structure is not fully conserved. Parts of the film overlay during the treatment, stick together and form multi-layer structures. Though not intended, it improves the stability of the substrate and prevents it from tearing and breaking once placed on the holey carbon support. For taking high resolution spectral images it is good practice to first find the thinnest areas on the grid, which are present in a sufficient quantity.

Figure 26 (a) shows the extracted signal of the boron K-edge and the nitrogen K-edge from an EEL spectrum image (SI) of the green framed area in Figure 24 (b). It can be seen that the area is subdivided into five parts with varying brightness, which directly relates to the thickness of the substrate. The brighter

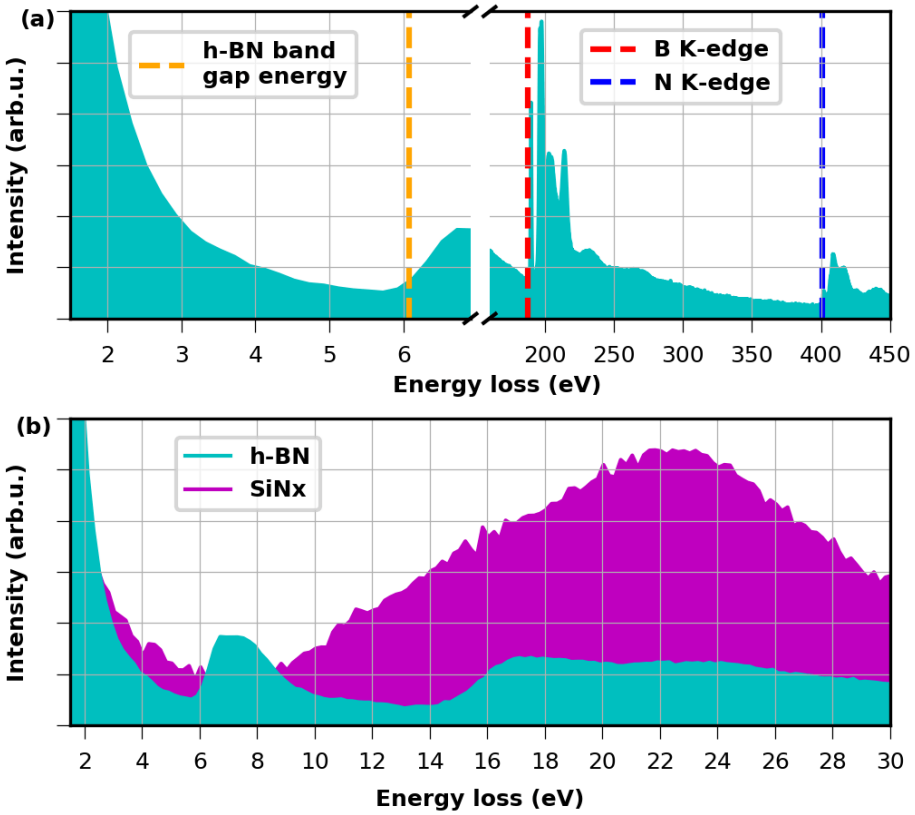

Figure 25: (a) EEL spectrum of the fabricated substrate acquired by integration over the green framed area in Figure 24 demonstrating that it consists of h-BN without any organic contamination. In the low-loss region the bandgap energy of monolayer h-BN at 6.07 eV [105] is marked with a vertical orange line. In the high-loss region of the same spectrum the boron K-edge at 188 eV and the nitrogen K-edge at 401 eV are marked by red and blue vertical lines, respectively. (b) A wider range in the low-loss region of the h-BN spectrum (cyan) in comparison to the EEL spectrum of a 5 nm thick SiN_X substrate (magenta) obtained under the same acquisition conditions.

a pixel appears, the higher the amount of electrons which interacted with the sample on their way through it and therefore the thicker the sample is. This means that there is a decrease in thickness from the cyan frame on the right side of the image to the green frame on the left side. From each of the five fractions with different brightness an equally sized area was chosen and the corresponding EEL spectra around the boron K-edge are plotted in Figure 26 (b). The spectra are associated with the framed areas in the SI by their color. The boron K-edge as well as the nitrogen K-edge (not displayed in the spectrum) show a very regular increase in intensity from one probed area to the next, which can be attributed to a thickness increase of a single atomic layer of h-BN. Due to the fact that this constant increment equals half the intensity of the thinnest examined area (green spectrum), it is concluded that in this region the substrate consists of bilayer h-BN. The thickness of the substrate in the depicted region in Figure 26 (a) therefore varies from two up to six atomic layers corresponding to about 0.7 nm to 2.1 nm. Furthermore, a comparison of the low-loss signature of the h-BN spectrum in Figure 25 (b) with measurements and simulations conducted by Nicholls *et al.* [135] and Pan *et al.* [136] confirms the conclusions stated above. We decided to use STEM EELS for the thickness determination instead of conventional STEM imaging because the results from EELS are particularly element specific and the signal at the boron and nitrogen edges can be analyzed directly. Furthermore, through the comparison of the low-loss signal with literature [135, 136] we can make an estimation on the thickness of the sample.

On one hand it is highly desirable to make the h-BN as thin as possible for LSP spectroscopy, however on the other hand this complicates the deposition of nanoparticles by conventional methods as an ultra-thin substrate is also very fragile and prone to damage upon exposure to mechanical stress. In this regard, the helium droplet approach provides a superior route for the decoration of fragile structures with nanoparticles under soft landing conditions [33].

3.4.2 LSPR mapping

The fabricated h-BN STEM grids were employed for high resolution EELS measurements on nanoparticles assembled and deposited utilizing the helium nanodroplet synthesis approach. Figure 27 (a) shows the HAADF image of a Ag particle, which is elliptically shaped. The major axis is 14 nm and the minor axis is 10 nm long. The entire area of the image was used for EELS data acquisition and the integrated and processed spectrum is plotted in Figure 27 (b). The spectrum shows a distinct feature between 2.5 eV and 4.0 eV with a maximum intensity around 3.2 eV, which represents the LSPR of the Ag particle. Two sections of the

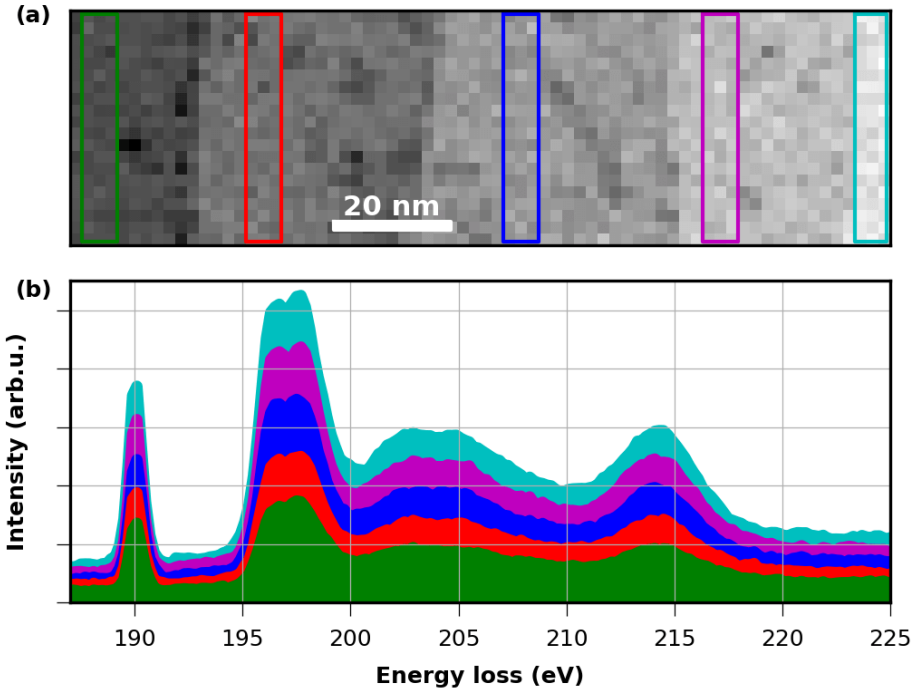

Figure 26: (a) The spatial representation of the boron K-edge and the nitrogen K-edge signal extracted from an EEL spectrum image (SI) of the green framed area in Figure 24 clearly shows regions with differing brightness indicating a thickness variation of the h-BN substrate. (b) A comparison of the EEL spectra of the framed regions in the SI shows the decrease in electron counts around the boron K-edge at 188 eV, corresponding to a decrease in thickness from the cyan towards the green spectrum. The colors of the spectra correspond to the frame colors in the SI.

spectrum around 2.8 eV and 3.2 eV are displayed in spatially resolved EELS maps in Figure 27 (c) and (d), respectively. The corresponding energy loss intervals are marked by frames centered at those energies with a width of 0.18 eV, corresponding to the full width at half maximum (FWHM) of the ZLP, which determines the spectral resolution. The LSPR map in Figure 27 (c) at (2.80 ± 0.09) eV of energy loss, marked by the red frame in the spectrum, shows two areas with high intensity, representing a high probability of electron energy loss, around the poles of the particle on the major axis. The maxima in energy loss correspond to the excitation of a longitudinal mode of the LSP of the Ag particle arising from the deviation of its shape from a perfect sphere. The second LSPR map in Figure 27 (d) shows the energy window at (3.20 ± 0.09) eV marked with a green frame in the spectrum. Here, at a slightly higher loss energy, a ring like shape of high intensity encircles the Ag particle. Presumably in this case the longitudinal mode is overlaid with the transverse mode of the LSP. The overall spectral position of the LSPR is comparable to results from Scholl *et al.* [137] or Raza *et al.* [138] even though their investigated particles were more spherical. Besides the impact of differences in particle shape, deviations from results available in literature are further attributed to the employed synthesis methods. Note that compared to chemically synthesized particles, nanoparticles produces by the He_N approach have the advantage of being solvent and surfactant free.

The second examined particle is a Ag@Au core@shell nanorod produced by utilizing a sequential pick-up scheme (cf. Methods). The HAADF image in Figure 28 (a) shows an elongated nanorod with a length of 20 nm and a diameter of 7 nm (aspect ratio of ≈ 2.9). To demonstrate the composition of the particle an elemental map is depicted in Figure 28 (b) showing in gold and silver colors the corresponding elements. To create the energy dispersive X-ray spectroscopy (EDS) map the event counts around the M_α peak of Au at 2.120 keV and the L_{α_1} peak of Ag at 2.984 keV were extracted from the EDS data and plotted spatially resolved. The Ag core has an elongated shape and is completely enclosed by the Au shell, which is thickest at the caps of the nanorod. The integrated EEL spectrum for the whole area in Figure 28 (c) contains a distinct LSPR peak around a loss energy of 1.95 eV. From the red framed interval covering an energy range of (1.95 ± 0.09) eV, a LSPR map was extracted, shown in Figure 28 (d). It can be seen that two maxima in electron energy loss are situated around the poles of the Ag@Au nanorod, representing an excitation of a longitudinal LSPR mode. The LSPR peak position for a nanorod is difficult to compare to literature not only due to differences in the synthesis approach but also because of the shift with a varying aspect ratio of the particle [139, 140]. Koh *et al.* [141] and N'Gom *et al.* [142] obtained comparable results by examining elongated Au particles with

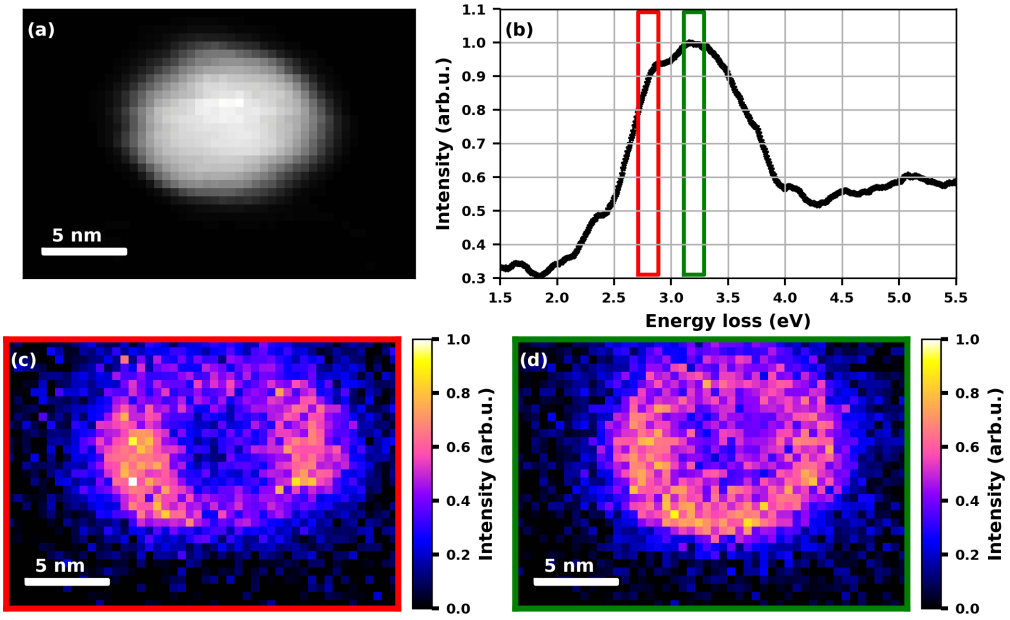

Figure 27: (a) HAADF image of an elliptically shaped Ag nanoparticle with (b) a plot of the processed EELS data integrated over the entire image. The framed sections in the spectrum are displayed as spatially resolved EELS maps.(c) A LSPR map at (2.80 ± 0.09) eV (red frame) and (d) a LSPR map at (3.20 ± 0.09) eV (green frame).

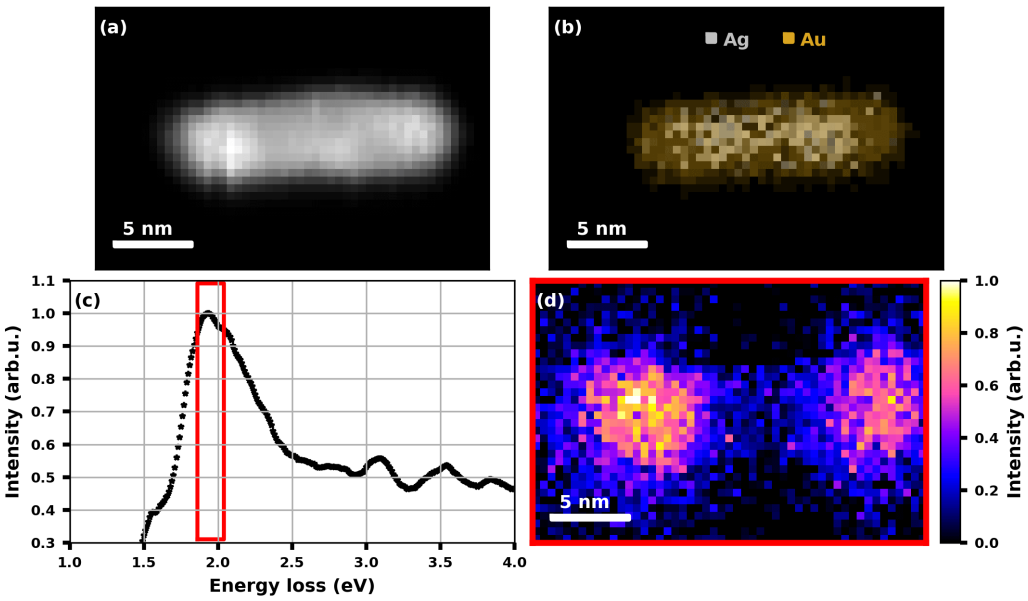

Figure 28: (a) HAADF image of a Ag@Au core@shell nanorod with (b) an elemental map extracted from the EDS data showing the Ag core and Au shell structure. (c) A plot of the processed EELS data integrated over the whole image area where the red framed section is used for (d) a plasmon resonance map at (1.95 ± 0.09) eV.

similar aspect ratios. Major effects on the LSPR peak by the Ag core are not observable, presumably because the shell is already thick enough such that the plasmonic properties of Au dominate the spectrum.

3.5 Conclusion

In conclusion, we successfully showed a way to use a very thin h-BN film for the fabrication of STEM substrates, which are ideal for high resolution studies of nanosized metal particles by means of EELS. We presented the crafting of the h-BN substrates, resulting in uniform flakes of h-BN on top of the holey carbon support grids with thicknesses of down to only a few atomic layers. The obtained substrates exhibit excellent characteristics, which can highly improve the quality of the information gained from the low-loss region of EEL spectra. The increased transmittance for electrons in the energy range below 6 eV is an inherent property of h-BN due to its wide bandgap, and the thinness and cleanliness of the substrates further contribute to a diminished background signal. A direct comparison between the h-BN substrate and a commercially available SiN_X substrate shows that h-BN provides a lower background signal over a wide energy range up to 30 eV. The primary application for the h-BN substrates can be found in the field of plasmonics, where the experimental analysis of LSPRs on the nanoscale and also the depiction in spatially resolved maps is attracting great interest. We demonstrate the applicability of the substrates for such measurements on two exemplary nanoparticles, namely a Ag and a Ag@Au core@shell particle, for which the acquisition of spectral features originating from LSPRs was feasible and the collected data is in good agreement with literature. The Ag and Ag@Au particles were fabricated employing the helium nanodroplet synthesis approach, which allows, in principle, due to its unique pickup and cluster formation method, the direct combination of a large variety of materials. Thus, we anticipate that the soft, helium cushioned deposition of particles on the substrate together with the potential for the creation of new plasmonic materials may open up exciting possibilities for the field of plasmonics.

4 Tunable Localized Surface Plasmon Resonance of Ag@Au Nanoparticles

The content of this chapter corresponds to the following peer reviewed and published scientific paper:

> "Helium nanodroplet assisted synthesis of bimetallic Ag@Au nanoparticles with tunable localized surface plasmon resonance" by Florian Lackner[3], **Alexander Schiffmann**[3], Maximilian Lasserus[3], Roman Messner[3], Martin Schnedlitz[3], Harald Fitzek[4], Peter Pölt[4], Daniel Knez[4], Gerald Kothleitner[4], and Wolfgang E. Ernst[3] in *The European Physical Journal D* **73**, 104 (2019).
> https://doi.org/10.1140/epjd/e2019-90696-8

The author of this doctoral thesis contributed to the publication in the following ways:

- Assistance with the design and execution of the experiment
- Literature research
- Conduction of preliminary experiments
- Synthesis of the nanoparticles
- Assistance in recording of the electron microscopy data
- Assistance with the evaluation and interpretation of the obtained experimental data
- Editing of the manuscript

All co-authors were engaged in the preparation and publication process of this paper. Their affiliations and a short recapitulation of their major contributions are given below:

Florian Lackner:
Design of the experiment and assistance with the execution, evaluation and interpretation of the measurement data, funding, and authorship of the manuscript.

[3]Institute of Experimental Physics, Graz University of Technology, Petersgasse 16, A-8010 Graz, Austria

[4]Institute of Electron Microscopy and Nanoanalysis & Graz Centre for Electron Microscopy, Graz University of Technology, Steyrergasse 17, A-8010 Graz, Austria

Maximilian Lasserus:
Assistance with the experiments.

Roman Messner:
Assistance with the experiments.

Martin Schnedlitz:
Assistance with the experiments.

Harald Fitzek:
Raman measurements, assistance with the evaluation of the obtained spectroscopic data, and editing of the manuscript.

Peter Pölt:
Supervision and funding for electron microscopy and Raman spectroscopy.

Daniel Knez:
Recording of the electron microscopy data, assistance with the evaluation, and editing of the manuscript.

Gerald Kothleitner:
Supervision and funding for electron microscopy.

Wolfgang E. Ernst:
Scientific advice, supervision, funding, and editing of the manuscript.

The authors of this publication gratefully acknowledge additional support provided by the Austrian Science Fund (FWF) under Grant No. P30940-N36 and NAWI Graz. Furthermore, they thank Thomas Jauk for contributions to the UV/vis spectrophotometer measurements and the Institute of Solid State Physics at Graz University of Technology for providing access to the UV/vis spectrophotometer.

Material from: "Helium nanodroplet assisted synthesis of bimetallic Ag@Au nanoparticles with tunable localized surface plasmon resonance" by Florian Lackner, Alexander Schiffmann, Maximilian Lasserus, Roman Messner, Martin Schnedlitz, Harald Fitzek, Peter Pölt, Daniel Knez, Gerald Kothleitner, and Wolfgang E. Ernst. *The European Physical Journal D* **73**, 104 (2019), Springer Nature.

4.1 Abstract

Nanoparticles with tunable localized surface plasmon resonance have been prepared by synthesis in helium nanodroplets. Subsequent surface deposition allows for the formation of substrates which can be employed for surface-enhanced Raman spectroscopy (SERS). The assembly of Ag@Au core@shell clusters of about 5 nm diameter in helium droplets with different Ag:Au ratio allows to tune the surface plasmon resonance between the plain Ag resonance at 447 nm and the Au resonance at 555 nm. For the fabricated substrates only a single plasmon resonance is observed in the UV/vis absorption spectra. The prepared nanostructures have been functionalized with 4-methylbenzenethiol (4-MBT) molecules and SERS spectra have been recorded. The results demonstrate the potential of the helium droplet synthesis approach, opening up a new route to the formation of tailored plasmonic nanoparticles and functional nanostructures.

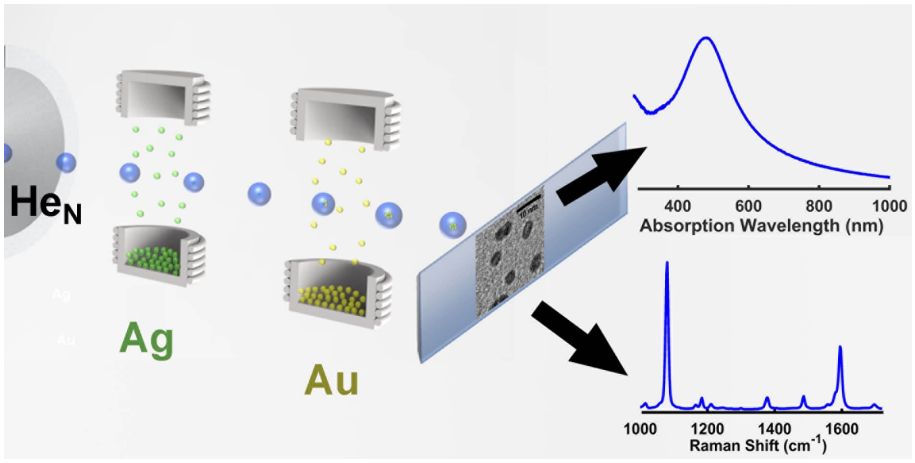

Figure 29: Graphical TOC - Surface enhanced Raman and UV/vis measurements conducted on Ag@Au core@shell nanoparticles with tunable localized surface plasmon resonance synthesized with the helium nanodroplet synthesis approach.

4.2 Introduction

Nano-sized particles have paved the way for exciting new research and applications in science and technology. Today, nanoparticles are ubiquitous and found application in catalysis [143] and photovoltaics [144] as well as in chemistry [145], biology [115] and medicine [146]. Hybrid nanoparticles, in particular, play an important role for emerging applications as they allow to tailor particle characteristics by deliberately combining materials with desired magnetic, optical or chemical properties [147]. The great potential of such nanoparticles and nanos-

tructures assembled thereof is calling for novel synthesis methods capable to rapidly explore a large variety of different material combinations. Here, we introduce the helium nanodroplet synthesis method as a novel approach for the production of functional hybrid nanoparticles with tailored plasmonic properties.

The advantages that come with the helium droplet approach are the (i) intrinsic inertness of the synthesis environment (liquid helium) that does not involve any solvents, surfactants or other chemicals, (ii) the large variety of dopants that can be combined and (iii) the cold environment (0.37 K) [17,18] that enables the production of nanoparticles with a core@shell configuration independent of the thermodynamically favored structure [50]. In the present study, we chose the Ag@Au system in order to demonstrate the controlled formation of plasmonic nanoparticles and nanostructures by helium droplet synthesis. However, in general the approach allows to select nanoparticle constituents from a large variety of materials.

Many of the outstanding optical properties of plasmonic materials are related to surface plasmon resonances or, in the case of coinage metal nanoparticles smaller than the wavelengths of visible light, localized surface plasmon resonances (LSPR). These plasmons can be understood as collective oscillations of electrons within the nanoparticle. The spectral position of a LSPR thereby depends strongly on the structure, shape and size of the particle [147]. The resonant interaction between an electromagnetic field and the surface plasmon causes a concentration of electromagnetic radiation close by the nanoparticle surface, an effect which forms the foundation of surface-enhanced Raman scattering (SERS): When a Raman active molecule is attached to the surface of a metal nanoparticle and exposed to electromagnetic radiation resonant with the LSPR it experiences a strongly enhanced field, which can boost the Raman signal by orders of magnitude [115].

Typically, Au or Ag nanostructures are used as SERS substrates, however, hybrid nanoparticles pose very promising building blocks for the preparation of novel SERS substrates for emerging and future applications [147, 148]. A well characterized material combination in this context is represented by Ag-Au hybrid nanoparticles [149], which we chose to demonstrate the capabilities of our synthesis approach. Previous studies on core@shell nanoparticles, with diameters larger than 10 nm, have shown that for a Ag@Au as well as a Au@Ag configuration typically two separate plasmon resonances are observed, one close to the original Ag LSPR and the other close to the Au LSPR peak, their respective intensities depending on the Ag:Au ratio [150–155]. In the alloyed form, however, nanoparticles exhibit only a single plasmon resonance and its position depends on the Ag:Au ratio [151,153,155,156]. It has been shown that both structures are

suitable for the preparation of SERS substrates [149, 152, 157].

With the helium droplet synthesis approach nanoparticles are formed when the droplets pass a pickup region, typically a cell in which a resistively heated oven establishes an increased vapor pressure of the desired dopant material. The subsequent arrangement of two of such pickup cells allows for the doping with two different materials. Under such conditions core@shell nanoparticles can be formed, where the material introduced first forms the core and the second the shell [6, 49]. Subsequently, the particles can be deposited on any desired substrate, thereby the surrounding helium acts as a cushion that is stripped off upon impact, dissipating the released energy and resulting in a very soft deposition [33, 158].

In the recent years helium droplets have evolved from a pure spectroscopic matrix [17, 18] to a synthesis method for nanoparticles [35, 121, 123, 159, 160]. However, the vast majority of works dealing with nanoparticle synthesis is focused on the investigation of particle size, structure and morphology. Here, we expand the helium droplet synthesis approach into the field of plasmonics by presenting a new tool for the production of bimetallic plasmonic nanoparticles and nanostructures.

4.3 Experimental

4.3.1 Nanoparticle synthesis

The employed helium droplet apparatus has been described in Ref. 124. Bimetallic nanoparticles are formed by guiding a helium droplet beam through two independent pickup zones at which enclosed, heated crucibles establish an increased vapor pressure of the desired dopant material. The employed helium droplets have a mean diameter of about 40 nm, obtained by using a nozzle temperature of 8 K, a stagnation pressure of 20 bar and a 5 μm diameter nozzle [125]. Upon passing the first pickup zone, loaded with Ag, the dopant atoms agglomerate inside the helium droplets. When passing the second pickup zone, loaded with Au, the agglomerated Ag clusters are covered by a Au shell [120]. Pure Ag and Au clusters are formed by heating only one crucible. After formation the nanoparticles are deposited on the desired substrates under UHV conditions in a subsequent chamber. Several substrates can be interchanged inside the apparatus without breaking the vacuum.

When metal atoms agglomerate, binding energy is released into the droplet, which is dissipated by the evaporation of He atoms. This process goes along with a decrease of the ^{4}He yield in the quadrupole mass spectrometer at the end of the machine [125], which, thus, provides a convenient way to monitor

the doping level. However, when applying this method to multiple dopants added subsequently to the droplets, differences in the binding energies have to be accounted for, which can be estimated by the bulk cohesive energies. In the case of Ag and Au clusters these energies correspond to 2.95 eV and 3.81 eV, respectively [161]. Thus, the depletion caused by Ag clusters formed in helium droplets is about 23% lower than for Au clusters. Consequently, the three selected compositions obtained by setting the attenuation of the droplet beam flux to 30% Ag / 20% Au, 20% Ag / 30% Au and 15% Ag / 35% Au correspond to a corrected Ag:Au composition ratio in terms of number of atoms of approximately 1.94, 0.86, and 0.55, respectively. However, for the sake of convenience we refer to these compositions as 2:1, 1:1 and 1:2 in the following. The estimated average total number of atoms (sum of Ag and Au atoms) introduced into the helium droplet remains fairly constant for different Ag:Au ratios and corresponds to about 2800 atoms per nanoparticle.

4.3.2 UV/vis absorption spectroscopy

UV/vis absorption spectra were recorded employing a Shimadzu UV-1800 spectrophotometer. The nanoparticles were deposited by introducing a fused silica microscope slide (Corning 7980, fused silica, 1 mm thickness) into the beam. The slide is subsequently taken out of the vacuum and placed into the spectrophotometer to acquire the spectra shown in Figure 33, using a second fused silica slide as reference.

4.3.3 Transmission electron microscopy (TEM)

For TEM experiments the clusters are deposited on TEM grids (Ted Pella, Inc., Prod. No. 01824), covered with an amorphous carbon film with a thickness of 3 nm. The TEM images shown in Figure 30 are recorded with a 120 kV LaB_6 FEI Tecnai 12 transmission electron microscope, equipped with a Bio Scan Camera (Gatan, Model 792). High-resolution scanning transmission electron microscopy (HR-STEM) is performed using a probe-corrected FEI Titan^3 G2 60-300 instrument. The STEM images shown in Figure 32 have been acquired using a high-angular annular dark-field (HAADF) imaging detector. Note that during transport from the helium droplet apparatus to the TEM instrument the samples are exposed to air for a short period of time, which should have no effect on the deposited Ag and Au materials.

4.3.4 Raman spectroscopy

After recording the absorption spectra of nanoparticles deposited on the fused silica glass slides, the substrates were functionalized with 4-methylbenzenethiol (4-MBT) molecules. The functionalization is done by immersing the substrate in a 0.1 mM solution of 4-MBT in DI water for 1 h. Excess 4-MBT is removed by subsequent immersion in ethanol. Raman spectra were acquired employing a LabRam HR 800 spectrometer. The used laser wavelengths (and powers) are 473 nm (12.5 mW), 532 nm (12.5 mW) and 633 nm (15 mW). A x10 Olympus MplanN (N.A. 0.25) objective was used to focus the laser onto the sample. For every substrate 64 spectra were measured across an area of 500 x 500 μm with an acquisition time of 8 seconds (and 2 accumulations) per spectra. The shown Raman spectra in Figure 34 and 35 correspond to the average of these 64 spectra. Enhancement factors EF were determined according to the definition and procedure provided by Le Ru *et al.* [162]:

$$EF = \frac{I_{SERS} \cdot N_{Ref}}{I_{Ref} \cdot N_{SERS}} = \frac{I_{SERS} \cdot c_{Ref} \cdot H_{eff}}{I_{Ref} \cdot A \cdot \mu_S} \tag{14}$$

All band intensities (I_{SERS}, I_{Ref}) were determined using the peak fit routine of the LabSpec 6 software. Reference measurements were done for two different solutions (ethanol and isopropanol; molar concentration $c_{Ref} = 0.5$ M) in order to obtain reference intensities for all bands without interference from the solvent. The effective height of the scattering volume $H_{eff} = 174\,\mu$m was determined as described in the supplementary information of Le Ru *et al.* [162]. The surface density μ_S of 4-MBT is taken from Camargo *et al.* [163] ($\mu_S = 5.3\,\text{nm}^{-2}$). From the TEM images, which show a projection of the deposited nanoparticles, the ratio of the surface area of the metallic nanoparticles to the total substrate area is estimated as $A = 0.58$ by assuming spherical particles.

4.4 Results and Discussion

Figure 30 shows a survey of bright-field (BF) images of the prepared bimetallic Ag@Au core@shell particles with Ag:Au ratios adjusted to 2:1 (red frame, a.), 1:1 (green frame, b.) and 1:2 (blue frame, c.), recorded by transmission electron microscopy (TEM). Note that the ratio refers to the estimated ratio of the number of atoms, which can be easily controlled by adjusting the temperatures of the pickup-ovens [120].

The nanoparticles were deposited on standard amorphous carbon TEM grids immediately after deposition on fused silica substrates at the same helium droplet

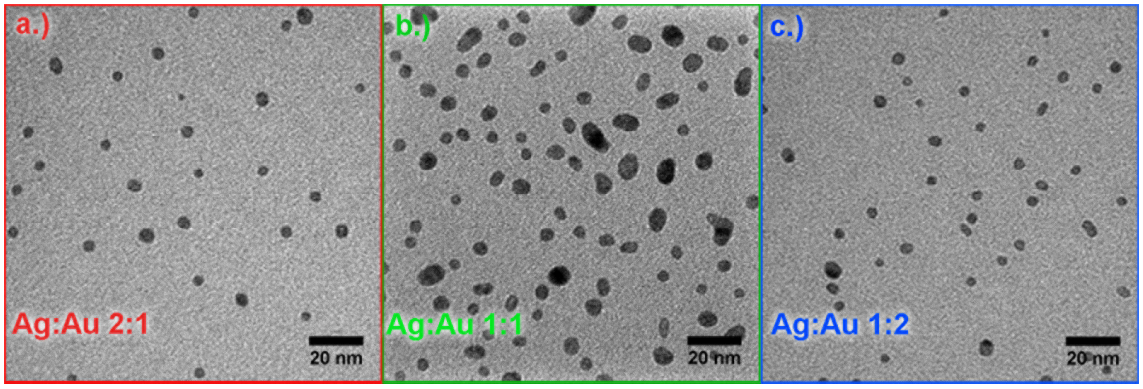

Figure 30: Bright-field (BF) transmission electron microscopy (TEM) images of the produced nanoparticles with Ag:Au ratios of 2:1 (red frame, a.), 1:1 (green frame b.) and 1:2 (blue frame, c.). Particles have been deposited for 30 min (2:1), 4 hours (1:1) and 30 min (1:2). The images show an overview of the deposited particles (scale bar 20 nm). Coagulation of a fraction of the particles is observed for long deposition times (middle image).

Table 1: Summary of the determined surface coverage (sc) per hour and the mean particle diameter d estimated by assuming spherical particles for nanoparticles with Ag:Au ratios of 2:1, 1:1 and 1:2, obtained from the recorded TEM images. In addition, the full width at half maximum (FWHM) of the particle size distribution for each Ag:Au ratio, shown in Figure 31, is listed.

Ag:Au ratio	sc per hour	d (nm)	FWHM
2:1	$(4.7 \pm 0.6)\%$	4.7	2.0
1:1	$(3.6 \pm 0.2)\%$	6.5	4.9
1:2	$(4.7 \pm 0.4)\%$	4.4	2.2

source conditions in order to reveal insight into the surface coverage, particle size and structure. The intensity in the shown BF images depends on the atomic number (Z), i.e. bright areas correspond to Ag rich zones whereas dark regions indicate Au rich zones. Note that only image b.) has been obtained upon deposition for four hours, similar to the samples used in the optical experiments. Nanoparticles in images a.) and c.) have been deposited for 30 min on the TEM grids. The comparison of particles prepared with different deposition times reveals insight into coagulation processes that can proceed upon deposition: While for low surface coverage nearly all particles remain separated, upon 4 hours of continuous deposition the surface coverage is high enough that a fraction of the particles coagulates and form larger structures.

The obtained surface coverages (sc) and mean particle diameters d (estimated

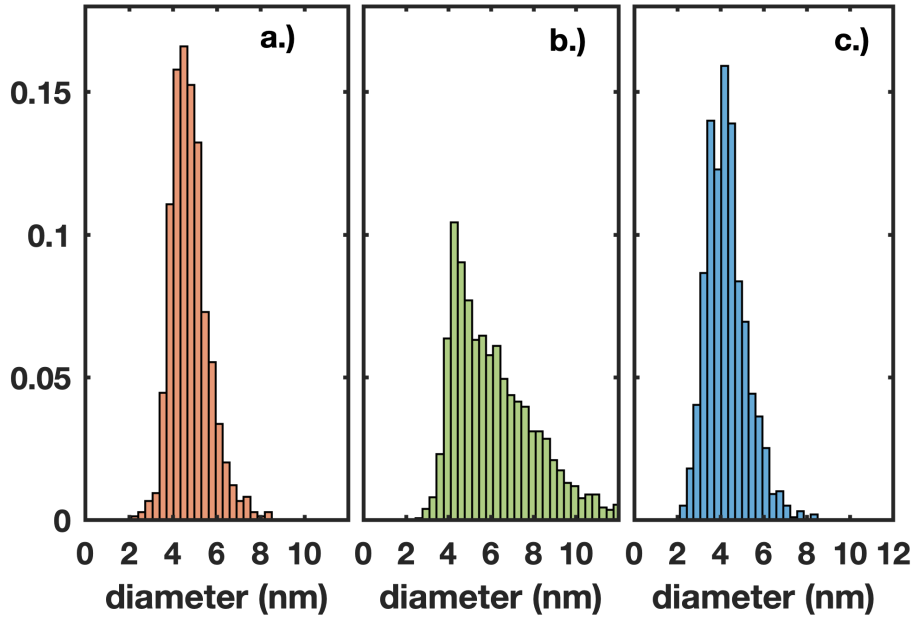

Figure 31: Size distributions for particles with an Ag:Au ratio of 2:1 (a.), 1:1 (b.) and 1:2 (c.). Note that, while panel a.) and c.) shows a distribution of particles deposited for 30 min, panel b.) shows the distribution of particles deposited for 4 hours, similar to the TEM images in Figure 30.

by assuming spherical particles) are listed in Table 1. Note that in order to ease a comparison, the surface coverages have been scaled to one hour of deposition, neglecting the statistic nature of the process, i.e. particles may be deposited on top of each other. It can be seen that coagulation, which becomes relevant in case of the longer deposition time for the 1:1 ratio particles, manifests in an increase of the estimated mean particle diameter and, to some extent, also in a decrease of the surface coverage.

The particle size distributions are shown in Figure 31, the corresponding full width at half maximum (FWHM) of each distribution is listed in Table 1. Here, the effect of particle coagulation becomes obvious by comparing the distributions in panel a.) and c.), where particles have been deposited for 30 min, to the distribution in panel b.) for which the particles have been deposited for 4 hours. Coagulation leads to a significant broadening of the distribution towards larger particle sizes. We note that the coagulation process may differ between the amorphous carbon TEM grid substrate and the fused silica glass slides. However, it has to be considered in the interpretation of the UV/vis absorption spectra that a fraction of larger particles, which may not retain a core@shell structure, can contribute to the signal.

While the images in Figure 30 allow a characterization of the particle sizes

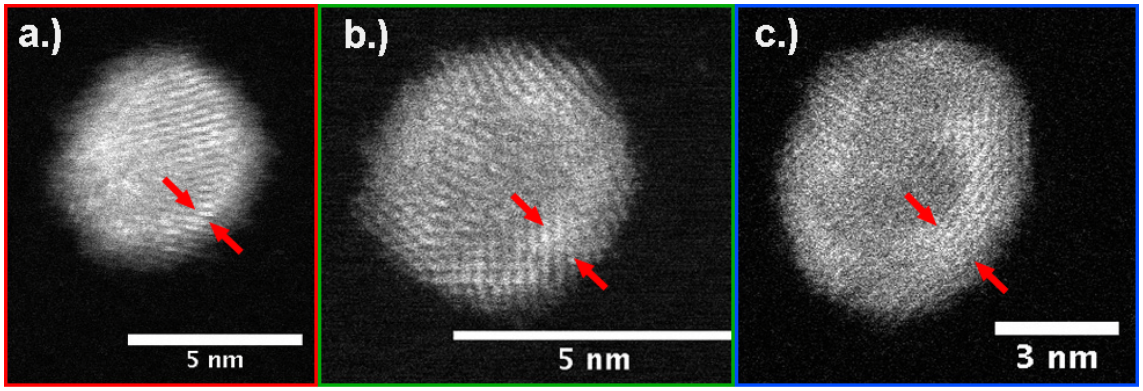

Figure 32: High-angle annular dark-field (HAADF) images of representative core@shell nanoparticles from a separate series of experiments, recorded by a high-resolution scanning transmission electron microscope (HR-STEM). The Ag:Au ratios correspond to 2:1 (red frame, a.), 1:1 (green frame, b.) and 1:2 (blue frame, c.). The Au shell layer is marked by red arrows.

and surface coverages, the resolution is too low in order to reveal insight into structural details, in particular, the core@shell structure of the particles. In order to provide further insight into the structure of nanoparticles in the 5 nm size regime formed by helium droplet synthesis we present selected high-resolution images in Figure 32. The shown particles have been produced in a previous series of experiments under similar helium droplet source conditions, however, the size of the shown particles and, in particular, the Ag:Au composition is the same as in the present study. Further details about the structure of nanoparticles comprising a Ag:Au ratio of 1:1 can be found in Ref. 49 (and the Supplementary Information of Ref. 49). The shown images in Figure 32 correspond to high-angle annular dark-field (HAADF) images recorded by a high-resolution scanning transmission electron microscope (HR-STEM). The Ag:Au ratios of the prepared nanoparticles corresponds to 2:1 (red frame, a.), 1:1 (green frame, b.) and 1:2 (blue frame, c.). The HAADF image intensity is proportional to the square of the atomic number (Z^2) [164]. Consequently, the image contrast within an individual nanoparticle represents zones that are rich of Ag (dark) or Au (bright).

It can be seen from the images in Figure 32 that even for the lowest Au doping level (Ag:Au of 2:1) a faint bright Au layer is visible at the surface (marked by red arrows). Consequently, it is concluded that even in the sub 5 nm size regime the helium droplet synthesis allows for the deposition of nanoparticles with a core@shell structure with extremely thin shell layers.

The optical properties of the prepared nanoparticles, deposited for 4 hours each onto fused silica substrates, have been characterized employing UV/vis absorption spectros-copy. The recorded spectra are shown in Figure 33. Plain

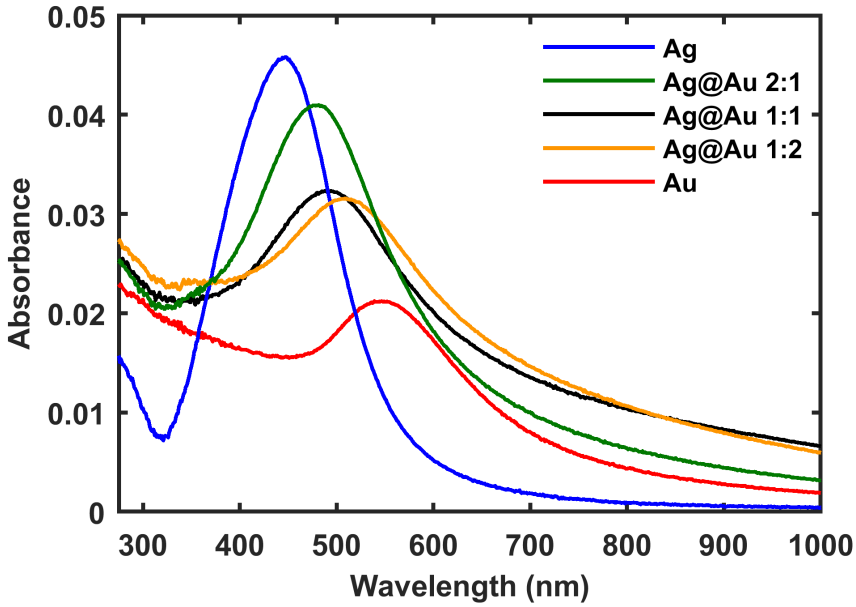

Figure 33: UV/vis absorption spectra of the prepared Ag, Au and Ag@Au core@shell nanoparticles deposited for 4 hours on fused silica substrates. The Ag:Au ratios have been adjusted to 1:2 (orange), 1:1 (black) and 2:1 (green). Spectra of bare Ag and Au particles are shown in blue and red, respectively. The LSPR peak maximum shifts from 447 nm (Ag) to 555 nm (Au) with increasing Au content, accompanied by an intensity decrease.

Ag (blue) and Au (red) nanoparticles serve as a reference, both exhibiting the characteristic LSPR of small, spherical nanoparticles on fused silica [149, 165] peaking at 447 nm for Ag and 555 nm for Au. The figure also features spectra of deposited core@shell nanoparticles with Ag:Au ratios adjusted to 1:2 (orange), 1:1 (black) and 2:1 (green). Only a single LSPR peak is observed, which becomes increasingly red-shifted with increasing Au content, accompanied by decreasing intensity. For high Ag concentration (Ag:Au of 2:1) the LSPR feature resembles the Ag resonance, red-shifted to 484 nm. For medium (1:1) and high Au content (1:2) the red-shift is stronger and the LSPR peak maxima are found at 499 nm and 518 nm, respectively.

Previous studies on bimetallic Ag-Au nanoparticles relied on different preparation processes such as coating of the core metal using radiation chemistry [151], laser ablation [154], or solution phase synthesis [153, 155, 156]. Measured absorption spectra indicated that core@shell nanoparticles exhibit two plasmon resonances, one close to the resonance of the pure Au particle and one close to the resonance of the pure Ag particle. It required the transformation into an alloy state to obtain continuous shifts of the then single resonance between the pure Au and Ag absorption wavelength, the shift depending on the Au/Ag molar ratios.

The size of the nanoparticles in these previous studies was of 15 nm diameter or larger [150,151,153,154]. As the different absorption behavior for bimetallic core@shell versus alloy nanoparticles was even used as diagnostic tool to distinguish the two states, Kuzma et al. [166] discuss optical properties of binary compound plasmonic nanoparticles (see also Ref. 167). They found that optical absorption spectra alone are not sufficient to predict structural arrangements.

In the case of helium droplet synthesis it is known that the nanoparticles that are formed in the droplet and subsequently deposited are of core@shell structure [49, 50, 120], which becomes also evident from Figure 32. However, as suggested by the particle size distribution in Figure 31, the optical spectrum does not only originate from the initially deposited core@shell particles but may also contain a contribution from larger, coagulated particles. The sum of both contributions leads to the relatively broad single plasmon resonance feature that is observed in the absorption spectrum. Furthermore, at a surface coverage of about 15% the coupling of LSPR modes between individual particles becomes important [168], the corresponding features may contribute to the spectrum in the red part of the spectra in Figure 33 at longer wavelength [169].

Here, single particle plasmon spectroscopy based on electron energy loss spectroscopy (EELS) [1,137] could reveal more insight into the plasmonic properties of individual particles as UV/vis absorption spectroscopy can only probe the average spectrum of a large number of particles. In particular, helium droplet synthesis would allow for the study of particles with very thin shell layers, such as shown in Figure 32 a.).

The prepared particles have a size of only $\sim$5 nm, corresponding to about 2800 atoms on average, and, thus, the increased surface to volume ratio becomes important. Considering a Mackay icosahedron structure [170], a cluster with 10 closed shells consisting of 2869 has 812 surface atoms, which corresponds to a surface to volume ratio of about 1:2.5. Thus, in this idealized scenario a Ag@Au core@shell particle consisting of 2869 atoms in total with a Ag:Au ratio of 2.5:1 could be surrounded only by one atomic monolayer of Au. From this estimation it becomes evident that at lowest Au doping levels the shell layer is extremely thin, in agreement with the nanoparticle shown in Figure 32 a.). This represents an interesting situation, where common theoretical models for the calculation of plasmon resonances that predict two disjunct peaks in the spectrum for core@shell nanoparticles [166,171] may cease to be valid as properties such as surface roughness, surface diffusion and atomic interdiffusion processes become important [172]. Furthermore, at around 5 nm various different cluster structures and morphologies become possible [159], which deviate from the idealized models.

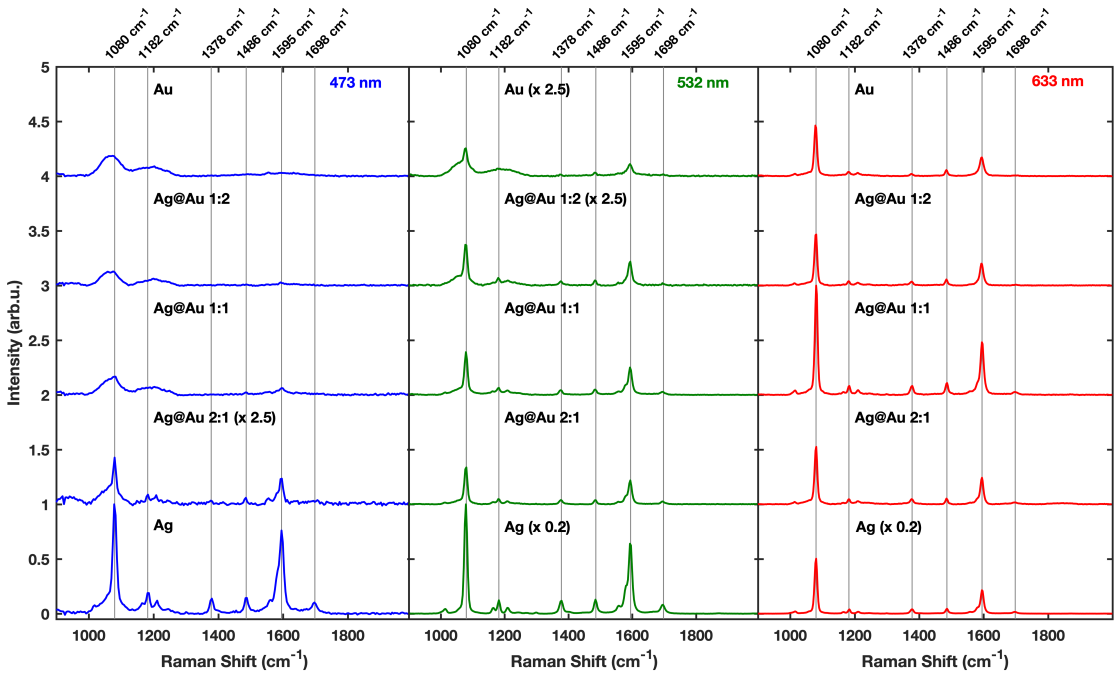

Figure 34: Raman spectra recorded for the different nanoparticles functionalized with 4-methylbenzenethiol (4-MBT) molecules obtained by employing three different Raman laser wavelengths of 473 nm (blue), 532 nm (green) and 633 nm (red). The Raman spectrum obtained from 4-MBT attached to core@shell nanoparticle substrates with Ag:Au ratios of 2:1, 1:1 and 1:2 are shown together with spectra obtained from substrates consisting of plain Au and Ag particles.

Table 2: Enhancement factors determined for the Raman mode at 1080 cm^{-1} for nanoparticle substrates comprising Ag:Au ratios of 2:1, 1:1 and 1:2 as well as for the plain Ag and Au nanoparticle substrates.

Ag:Au	473 nm	532 nm	633 nm
1:0	1800	24000	30000
2:1	≈ 200	2100	6300
1:1	≈ 70	1700	12000
1:2	bld*	≈ 800	5800
0:1	bld*	≈ 300	5500

*bld: below limit of detection

Having characterized the nanoparticles and their optical properties, we can now proceed to analyze their capabilities as substrates for surface-enhanced Raman spectroscopy (SERS). Therefore, the nanoparticles deposited on fused silica substrates were functionalized with 4-methyl-benzenethiol (4-MBT). The Raman spectra obtained for plain Ag and Au nanoparticle substrates as well as for bimetallic particles are shown in Figure 34 for three different Raman laser wavelengths. Note that the Ag spectra for 532 nm and 633 nm in Figure 34 have been scaled by x 0.2 and the 532 nm Au an Ag@Au 1:2 as well as the 473 nm Ag@Au 2:1 spectra have been scaled by x 2.5.

From near-edge X-ray absorption fine structure (NEXAFS) spectroscopy it is known that the sulfur atom, situated at one end of the molecule, binds to the surface (in the ideal case of a planar Au(111) surface the benzene ring is tilted by 33° with respect to the surface) [173, 174]. Furthermore, 4-MBT is known to form self-assembled monolayers on both Ag and Au surfaces [175].

The Raman spectrum in Figure 34 can be readily assigned based on comparison to literature [163, 176]. The most intense peak at 1080 cm^{-1} corresponds to a combination of a phenyl breathing mode, a CH in-plane bending and CS stretching (7a vibrational mode). The intense peak at 1595 cm^{-1} corresponds to a phenyl ring stretching mode (8a vibrational mode). The three peaks in between these two intense features at 1182 cm^{-1}, 1378 cm^{-1}, and 1486 cm^{-1} as well as the peak at 1698 cm^{-1} are assigned to in-plane phenyl ring vibrations. The broad structures observed in the left panel (473 nm) of Figure 34 for the three top most spectra and for the top spectrum in the middle (532 nm) panel correspond to residuals from the fused silica substrate, only the sharp lines are associated with signals from molecules.

Enhancement factors have been determined for the strongest Raman mode at

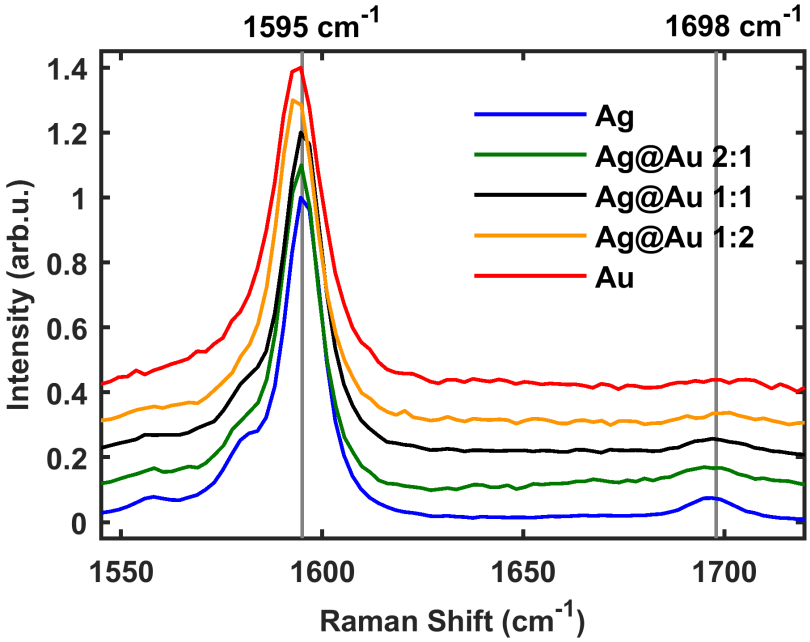

Figure 35: Zoom into the (normalized) Raman spectrum obtained with the 532 nm laser in the region of the 1595 cm^{-1} and 1698 cm^{-1} modes, which are sensitive to the substrate. It can be seen that the spectra gradually change their character from the case of molecules bound to plain Ag towards plain Au nanoparticles with increasing Au shell thickness.

1080 cm^{-1} and are listed in Table 2. Note that the Raman enhancement factors have been determined by averaging over a 500 μm x 500 μm area. Considering that the particles are close enough to coagulate, hot-spots between nearby nanoparticles are, presumably, present on the substrate, boosting the observed enhancement factors. It can be seen that the Ag nanoparticle substrate, which also exhibits the most intense LSPR, shows the highest enhancement. In general, the enhancement factors are lowest for the blue laser (473 nm) and highest for the red laser (633 nm). The enhancement factors for the bimetallic substrates are situated in between the pure Ag and Au nanoparticle substrates, where the Ag@Au nanoparticles comprising a 1:1 Ag:Au ratio show the next highest enhancement after the pure Ag nanoparticles. Note that the position of the LSPR maximum (which may be affected by the functionalization with 4-MBT [177]) does not necessarily have to coincide with the wavelength for maximum Raman enhancement [178], in particular, for substrates where individual nanoparticles are not completely isolated from each other.

An interesting aspect of the Raman spectra is the dependence of the Raman bands at 1595 cm^{-1} and 1698 cm^{-1} on the nanoparticle substrate, which differ greatly between the case where the molecules are attached to a Au or a Ag surface.

For 4-MBT on Ag it is known that the peak at 1595 cm^{-1} shows a characteristic asymmetry [163]. The origin of this effect is still under debate but it may either be caused by a broadening of the 8a mode or a selective enhancement of the 8b mode, located about 15 cm^{-1} below. However, on Au substrates this effect is absent [176]. Furthermore, the 1698 cm^{-1} mode is only significantly enhanced for the Ag substrate [176]. Figure 35 shows a zoom into the corresponding region. It can be seen that the spectra gradually change their character from plain Ag to plain Au character with increasing Au shell thickness. Only when multiple Au shell layers are present (Ag:Au of 1:2, orange spectrum) the spectrum resembles the one obtained for molecules attached to plain Au nanoparticles. This indicates that even if coagulated, larger particles are formed on the glass substrate and contribute to the signal, in the case of nanoparticles with an Ag:Au ratio of 1:2 they are still covered by a fully closed Au shell.

4.5 Conclusion

The present work demonstrates the capabilities of the helium droplet synthesis approach for the production of small plasmonic nanostructures. It is shown that for deposited Ag@Au core@shell nanoparticles, with diameters of about 5 nm, the spectral position of the localized surface plasmon resonance can be controlled by the Ag:Au ratio, which has been adjusted to 2:1, 1:1 and 1:2. Furthermore, upon functionalization with 4-MBT molecules, the nanostructures prepared from these nanoparticles are shown to be suitable substrates for surface-enhanced Raman spectroscopy (SERS). Raman enhancement factors determined for the 1080 cm^{-1} mode are on the order of 10^3-10^4. The Raman spectroscopy results further reveal that only particles with highest Au concentration (Ag:Au of 1:2) exhibit the signature of a plain Au shell.

In the present work we demonstrate the helium droplet synthesis approach for the production of plasmonic nanoparticles and nanosubstrates with the standard plasmonic materials, Au and Ag as well as bimetallic Ag@Au particles. However, in general the pickup technique allows choosing from a large variety of possible dopant materials. Moreover, the production method allows to produce small core@shell clusters without any chemistry involved, while the 5 nm size does not even represent a lower limit. The approach can be easily employed to explore novel material combinations for applications in plasmonics [179]. A particularly interesting field for which the approach seems well suited is the production of SERS active substrates composed of nanoparticles with plasmon resonances in the UV, such as aluminum [180], due to the inert synthesis environment and the possibility to protect core materials from oxidation by suitable shell materials [50].

As the helium synthesis approach has recently been employed for the production of nanoparticles interesting for catalysis [50, 181], the approach may also enable the production of systems that combine plasmonic with catalytic properties [182].

5 Synthesis and Characterization of Plasmonic Ag@ZnO Nanoparticles

The content of this chapter corresponds to the following peer reviewed and published scientific paper:

> "Helium droplet assisted synthesis of plasmonic Ag@ZnO core@shell nanoparticles" by **Alexander Schiffmann**[5], Thomas Jauk[5], Daniel Knez[6], Harald Fitzek[6], Ferdinand Hofer[6], Florian Lackner[5], and Wolfgang E. Ernst[5] in *Nano Research* **13**, 2979–2986 (2020).
> `https://doi.org/10.1007/s12274-020-2961-z`

The author of this doctoral thesis contributed to the publication in the following ways:

- Design and execution of the experiment
- Synthesis of the nanoparticles
- Assistance in recording of the electron microscopy data
- Evaluation and interpretation of the data obtained by electron microscopy
- Recording of the photoelectron spectroscopy data
- Evaluation and interpretation of the data obtained by photoelectron spectroscopy
- Literature research
- Authorship of the manuscript

All co-authors were engaged in the preparation and publication process of this paper. Their affiliations and a short recapitulation of their major contributions are given below:

Thomas Jauk:
Assistance with the experiments and data evaluation, operation of the NanoESCA and the laser system (during his Master's Thesis), literature research, and editing of the manuscript.

[5]Institute of Experimental Physics, Graz University of Technology, Petersgasse 16, A-8010 Graz, Austria

[6]Institute of Electron Microscopy and Nanoanalysis & Graz Centre for Electron Microscopy, Graz University of Technology, Steyrergasse 17, A-8010 Graz, Austria

Daniel Knez:
Recording of the electron microscopy data (STEM) and editing of the manuscript.

Harald Fitzek:
Recording of the electron microscopy data (SEM) and editing of the manuscript.

Ferdinand Hofer:
Supervision and funding for electron microscopy.

Florian Lackner:
Scientific advice, assistance with the experiments and data interpretation, funding, and editing of the manuscript.

Wolfgang E. Ernst:
Scientific advice, supervision, funding, and editing of the manuscript.

The authors of this publication gratefully acknowledge additional support provided by the Austrian Science Fund (FWF) under Grant No. P30940-N36, NAWI Graz, and the European Union's Horizon 2020 research program under Grand Agreement No. 823717-ESTEEM3. Open access funding was provided by Graz University of Technology.

5.1 Abstract

Plasmonic Ag@ZnO core@shell nanoparticles are formed by synthesis inside helium droplets with subsequent deposition and controlled oxidation. The particle size and shape can be controlled from spherical sub-10 nm particles to larger elongated structures. An advantage of the method is the complete absence of solvents, precursors, and other chemical agents. The obtained particle morphology and elemental composition have been analyzed by scanning transmission electron microscopy (STEM) and energy dispersive X-ray spectroscopy (EDS). The results reveal that the produced particles form a closed and homogeneous ZnO layer around a 2 - 3 nm Ag core with a uniform thickness of (1.33 ± 0.15) nm and (1.63 ± 0.31) nm for spherical and wire-like particles, respectively. The results are supported by ultraviolet photoelectron spectroscopy (UPS), which indicates a fully oxidized shell layer for the particles studied by STEM. The plasmonic properties of the produced spherical Ag@ZnO core@shell particles are investigated by two-photon photoelectron (2PPE) spectroscopy. Upon excitation of the localized surface plasmon resonance in Ag at around 3 eV, plasmonic enhancement leads to the liberation of electrons with high kinetic energy. This is observed for both Ag and Ag@ZnO particles, showing that even if a Ag cluster is covered by the ZnO layer, a plasmonic enhancement can be observed by photoelectron spectroscopy.

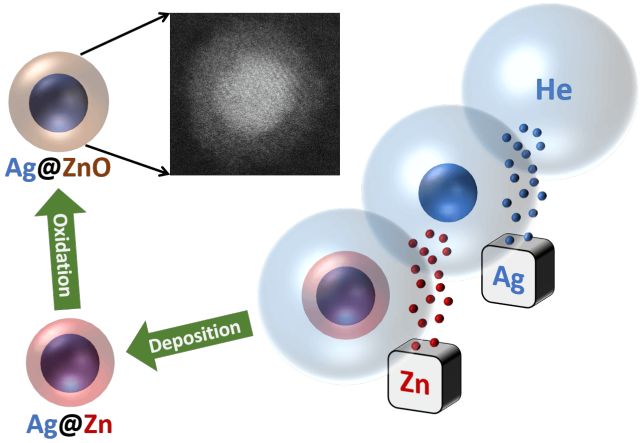

Figure 36: Graphical TOC - Plasmonic Ag@Zn core@shell nanoparticles are formed in a unique way inside a pristine environment employing the helium droplet synthesis approach. After subsequent oxidation the Ag@ZnO nanoparticles are investigated by several analysis techniques including scanning transmission electron microscopy, ultraviolet photoelectron spectroscopy, and two-photon photoelectron spectroscopy.

5.2 Introduction

Zinc oxide has become one of the most popular materials for applications in the fields of photocatalysis and optoelectronics due to its intriguing properties. ZnO is a non toxic n-type semiconductor with a wide direct band gap of 3.37 eV, very similar to TiO_2 but with a higher absorption efficiency under solar irradiation and a large exciton binding energy of about 60 meV [183]. As a photocatalyst it shows high potential in degradation processes of organic pollutants via the generation of reactive oxygen species and also exhibits antibacterial properties, especially when scaled down to the nano regime [184]. Due to its photoconductivity and photoluminescence characteristics, applications of ZnO in optoelectronics are possible, for example, in ultraviolet (UV) detectors, solar cells, lasers, and various sensing devices [185, 186].

In recent years, miniaturization and engineering of material properties on the nanometer scale have strongly influenced the research on ZnO. Starting with needles and other structures in the micrometer size regime [187], by now the synthesis of ZnO nanoparticles is an important branch of research. An increasing amount of one-, two-, and three-dimensional structures have been synthesized in shapes ranging from nanoparticles, -rods, and -ribbons over nanoplates to exotic flower or snowflake structures [188]. The formation of ZnO based composite materials opens up further possibilities for the tuning of properties, which permit the addition of new functionalities and, consequently, the doping of ZnO receives increasing attention. Different material groups can be used as dopants, for example, to produce p-type ZnO, enable applications in spintronics, or to improve optical and electrical properties [189]. A modification with Ag can significantly enhance the photocatalytic activity of ZnO [190] because the electron-hole pair concentration is increased by the strong local fields induced by the excitation of the localized surface plasmon in Ag [191].

Most of the synthesis routes for pure or doped nanosized ZnO have in common that they are based on multi-step chemical processes involving solvents or precursors. Though those techniques are well controlled and documented, it is possible that residues from chemical agents or surfactants remain at the particle surface or even at the core-shell interface.

In this study, the helium nanodroplet synthesis approach is employed as a pristine and facile technique for the synthesis of Ag@ZnO core@shell nanoparticles. This process bears the advantage of dispensing no chemicals, additives, or other additional agents besides the high purity metals, which are doped into the superfluid helium droplets where they agglomerate to nanoparticles. Since the whole procedure is conducted under ultra-high vacuum (UHV) conditions, a

contamination of the sample and other influences from environmental sources are excluded. Due to the dependence of the particle size and shape solely on a few well defined and accurately adjustable experimental parameters the approach allows for a high reproducibility. The range of accessible shapes spans from smaller spherical to longer wire-like nanoparticles, as shown in the course of this study. The obtained particle size and shape depends on the helium droplet source conditions, with which the helium droplet size can be controlled [125]. Small helium droplets lead to the formation of spherical nanoparticles, typically with a diameter below 5 nm. As a consequence of their superfluidity, large droplets host quantum vortices [192], along which dopants preferentially agglomerate enabling the formation of wire-like nanoparticles. Even though the scalability of the production is limited because only a few 100 ng per hour can be produced, the method allows for an investigation of fundamental particle properties. Furthermore, for future experiments the synthesis of core@shell species with a wide range of material combinations is accessible with one experimental setup simply by exchanging the dopant metal sources. Electron microscopy has been used to probe the size distribution, morphology, and composition of the deposited nanoparticles, revealing that the Ag cores are covered by a uniformly shaped wurtzite ZnO shell. Further investigations on the oxidation state of the ZnO shell have been conducted by ultraviolet photoelectron spectroscopy and two-photon photoelectron spectroscopy was employed to demonstrate the plasmonic activity of the ZnO covered Ag core.

5.3 Experimental

5.3.1 Nanoparticle synthesis

The ZnO and Ag@ZnO core@shell nanoparticles investigated in this work were produced utilizing the helium nanodroplet approach. This technique employs superfluid helium droplets (He_N) as an inert environment for the synthesis of nanosized metallic particles [28, 123, 159]. Details about the experimental design of the He_N apparatus can be found in Ref. [124]. In summary, a closed cycle refrigeration unit (Sumitomo RDK-408D2) is used to cool gaseous helium (99.9999% purity) at a stagnation pressure of 20-60 bar down to only a few Kelvin. The helium is then adiabatically expanded into high vacuum ($\approx 10^{-5}$ mbar) through a 5 μm diameter nozzle resulting in a beam of superfluid He_N. The internal temperature of the He_N, thereby, drops to 0.37 K [17, 18]. The droplet sizes can be controlled by the temperature and the stagnation pressure of the helium gas. For this work a setup with a pressure of 20 bar at 8 K was used

for the synthesis of spherical nanoparticles resulting in a He droplet diameter of about 70 nm with a mean number of about 5×10^6 He atoms. [125] For the larger wire-like particles the parameters were changed to 20 bar and 5 K leading to He_N diameters of around 1 ¯m, consisting of about 2×10^{10} He atoms [125]. Subsequently, the collimated He_N beam passes through another chamber ($\approx 10^{-7}$ mbar) where resistively heated tungsten baskets coated with aluminium oxide are used as pickup cells for the evaporation of high purity metals. While passing through the metal vapor, the He_N are doped with the evaporated atoms.

The superfluidity of the He_N matrix enables an unobstructed and frictionless roaming of dopant atoms. Upon statistical collisions within the He_N, the dopants accumulate and start to form clusters [25,26]. Initially, these clusters are grown as multicenters inside a droplet before they further agglomerate to larger structures. The final size of the nanoparticles depends on the doping rate and on the initial He_N size, since both affect the average time between collisions and, thereby, the growth rate [27]. The synthesis of wire-like nanoparticles is enabled by the presence of vortices in larger He droplets with diameters of several hundred nanometers. These vortices form due to the angular momentum acquired by the superfluid droplets during the expansion of the helium through the nozzle into vacuum [31,192,193]. The dopant metal atoms and grown clusters inside the droplets can agglomerate along such vortices due to a pressure gradient directed towards the vortex core [23]. By adjusting the size of the droplets accordingly and by doping enough material into them, elongated wire-like structures can be formed along the vortices [27,29,30]. As stated above for the two employed parameter settings in this experiment, a change in the helium source conditions directly influences the size of the He_N and allows for a facile switching between the different nanoparticle types. It should be noted that by decreasing the source temperature not only the droplet size is increased, also the total He_N flux and the deposition rate are enhanced. During agglomeration of atoms and clusters, the released binding energy is dissipated by the evaporation of He atoms from the droplet. The attenuation of the He_N beam due to the decrease in droplet size caused by this process is measured in order to monitor the particle growth process [27]. The synthesis of core@shell particles is enabled by the subsequent doping of two different metals in consecutive pickup cells [1,6]. Before entering the second pickup cell holding the shell material, the particle cores have already formed with the metal provided in the first cell. The metal doped to the droplets in the second pickup cell forms a shell layer around the core [120]. The dopant vapor pressure in each cell and, thereby, the metal atom doping rate and the nanoparticle growth are directly controlled by the temperature of the resistively

heated pickup cells. Since the pickup cells are separately controlled, the amount of doped core and shell material can be adjusted independently. This allows for a tailoring of the core diameter and the shell thickness of the synthesized nanoparticles within a certain range, as has been shown for Ag@Au [2] and Fe@Au [194]. For this work, the pickup cells were loaded with Ag and Zn, enabling the formation of pure Ag, Zn and Ag@Zn core@shell particles inside the helium droplets.

After leaving the pickup region, the He_N beam reaches a third chamber at UHV conditions ($\approx 5 \times 10^{-10}$ mbar), where the deposition rate is monitored by termination of the beam on a quartz crystal microbalance. For deposition of the nanoparticles the substrates are inserted into the beam path with a wobblestick transfer system coupled to a vacuum suitcase (Ferrovac GmbH, NexGeneration UHV Suitcase). The suitcase allows for the storage and transport of the samples at UHV conditions ($\approx 1 \times 10^{-10}$ mbar). Due to the different employed analysis methods, support grids for scanning transmission electron microscopy (STEM) (Ted Pella Inc., Ultra-thin Carbon Film on Lacey Carbon Support Film, 300 mesh, Au) as well as glass coverslips coated with indium tin oxide (ITO) (spi Supplies, $30 - 60\,\Omega$, $18 \times 18\,mm^2$, No. 1) were used as substrates. As the He_N beam is terminated at the substrate, the particles are cushioned by the surrounding helium and, therefore, keep their shape upon deposition under soft landing conditions [33, 195] as observed by atomic resolution electron tomography [49]. To start the oxidation of the Zn within the nanoparticles, the vacuum chamber with all the decorated substrates inside, was flushed with pure oxygen up to a pressure of 1×10^{-6} mbar for 1 h. A single carbon substrate has been decorated with both fabricated species, i.e. the spherical and wire-like nanoparticles, for the STEM experiments. During transport to the STEM, this sample was exposed to ambient air for about 1 hour. The spherical particles deposited on the ITO substrates for the UPS and 2PPE experiments have initially not been exposed to ambient air due to the use of the vacuum suitcase for the transport. Only later, in the course of the experiment, these samples have been deliberately exposed to air in order to achieve complete oxidation.

5.4 Scanning transmission electron microscopy

A detailed analysis of the nanoparticle structure and composition was conducted with a probe-corrected FEI Titan^3 60-300 STEM with an X-FEG field emission source operated at a beam energy of 300 keV. The STEM system is equipped with an FEI Super-X four-quadrant detector for energy dispersive X-ray spectroscopy (EDS). For the acquisition of data, the number of channels was set to 1024 with a

dispersion of 10 eV per channel and an exposure time of 100 ms was used. For high-angle annular dark-field (HAADF) images the dwell time per pixel was set to 2.4 μs, while the size of the spectrum images (SI) was adjusted for each individual acquisition.

5.5 Photoemission electron spectroscopy

Photoelectron spectroscopy was conducted with a NanoESCA (FOCUS GmbH & Scienta Omicron) energy filtered photoemission electron microscope (EF-PEEM) at UHV conditions ($\approx 3 \times 10^{-11}$ mbar). A helium discharge lamp (HIS) operated at 21.2 eV and the second harmonic of an Indigo-S Ti:Sapphire laser system (Coherent) tuned to 3.02 eV (410 nm) were used as photon sources for the acquisition of ultraviolet photoelectron spectra (UPS) and two-photon photoelectron (2PPE) spectra, respectively. The pulse duration of the laser was 30 ns with a repetition rate of 5 kHz. The spot size of the HIS on the sample surface was about 330 μm, while the laser was focused to a spot size of about 50 μm (full width at half maximum) at a laser power of 0.5 mW. With the pass energy for the energy filter set to 50 eV and an entrance slit of 1 mm, an energy resolution of 200 meV was reached. An extractor field of 12 kV was applied with a sample distance of 1.63 mm. The energy filtered photoelectrons were collected and counted with a channeltron (CT), the measurement area was restricted to a spot size with (7 ± 1) μm diameter using an iris aperture.

5.6 Results and Discussion

5.6.1 Nanoparticle structure and morphology

For STEM analysis, an amorphous carbon TEM grid was decorated with two different types of nanoparticles in order to give an example of the capabilities of the helium nanodroplet synthesis approach in terms of possible particle shapes. These two selected types encompass small, spherically shaped Ag@ZnO core@shell nanoparticles (source conditions: 20 bar and 8 K) deposited for 40 min, as well as wire-like Ag@ZnO core@shell nanoparticles (source conditions: 20 bar and 5 K) deposited for 3 min. Note that both types of nanoparticles were deposited on a single TEM grid, hence both species can be seen in the images presented in the following. During transport and transfer into the STEM, the sample was exposed to ambient conditions for about 1 h in total, which is enough time for the Zn shell to completely oxidize. This finding is in agreement with previous studies, which found that an oxide layer with a thickness up to 3 nm is formed directly upon exposure to air [196].

Figure 37 (a) shows a selected HAADF image in which the two particle types can be identified. The bright Ag cores within the particles can be clearly distinguished from the surrounding ZnO since the HAADF image intensity is proportional to the square of the atomic number (Z^2) [164]. It can be seen that the synthesis route based on the formation of Ag@Zn particles and subsequent oxidation of the Zn to ZnO results in a very uniform shell around the core, covering the Ag in a ZnO layer of constant thickness. This is true for the smaller spherical particles as well as for the larger wire-like structures as the presented STEM image shows. The measurement and subsequent statistical analysis of a random selection of 110 spherically shaped Ag@ZnO particles yielded a mean shell thickness of (1.33 ± 0.15) nm. The larger, wire-like Ag@ZnO structures were less frequently imaged and 35 were analyzed, resulting in a mean ZnO shell thickness of (1.63 ± 0.31) nm. Further HAADF images with lower magnification are presented in Fig. 42 in the Electronic Supplementary Material (ESM), providing an overview of the particle distribution on the substrate. In Fig. 43 in the ESM another set of detailed high-resolution HAADF images is presented to give a more thorough picture of the particle quality and the regularity of the ZnO shells covering the Ag cores.

A structural analysis of the uniformly grown ZnO within a selected particle is presented in Fig. 37 (b), which shows a detailed STEM HAADF image of the surface of a nanoparticle oriented in [001] direction. The contrast is enhanced and the observable hexagonal structure is highlighted by a red hexagon to guide the eye. The inset plot in Fig. 37 (c) shows the corresponding fast Fourier transform (FFT), which allows conclusions on the crystal structure of the ZnO shell layer. The FFT image yields lattice distances of (0.30 ± 0.02) nm and (0.18 ± 0.01) nm, marked by dashed orange circles. The observed pattern clearly exhibits sixfold symmetry. All visible features are assigned with the corresponding Bravais-Miller indices. The six diffraction spots on the inner circle and the six spots on the outer circle show permutation symmetry among themselves and originate from the $\{100\}$ and $\{2\bar{1}0\}$ planes of wurtzite ZnO, respectively. The obtained distances are in agreement with literature bulk values for the lattice spacing of 0.2814 and 0.1625 nm, taken from the Crystallography Open Database (COD) [197]. Deviations from the tabulated values most likely originate from the fact that the shell is only several atomic layers thick, which can lead to a lattice expansion as reported for several oxides on the nanoscale [198]. In the inset plot Fig. 37 (d) the two periodically occurring lengths found in the FFT image are assigned to the two-dimensional projection of the hexagonal structure of ZnO in [001] direction. Figure 44 in the ESM shows additional evaluated FFT images of Ag@ZnO nanoparticles in varying orientations, confirming the findings from

Fig. 37. Overall, with the obvious sixfold symmetry and the lattice parameters in good agreement with literature, it is concluded that the ZnO shell layer prefers a wurtzite unit cell structure in case of the synthesized nanoparticles.

The chemical composition of the nanoparticles was determined by means of EDS. Figure 38 (a) shows a HAADF image of several spherically shaped core@shell nanoparticles. An EDS map acquired from this area was used to create the spatially resolved elemental maps for Ag, Zn and O, which are shown in Figs. 38 (b)-(d). In particular, the event counts around the $L_{\alpha 1}$ peak of Ag at 2.984 keV, the L_{α} peak of Zn at 1.012 keV, and the K_{α} peak of O at 0.523 keV were extracted from the EDS data and plotted according to their respective position in the image. It is evident that the positions of the bright core structures in the HAADF image are matching those with high abundance of Ag. The same applies for the whole particles including the shell and the respective EDS data for Zn. The slight offsets between particle positions in the HAADF image and the EDS maps may originate from a drift of the sample or a mobilization of the nanoparticles due to the exposure to the electron beam for longer times during the acquisition. These effects can hardly be avoided since the HAADF image and EDS data are acquired in independent scans. Note that the position of oxygen is not as precise as for the metals because it is also present in the background in form of hydrocarbons on the STEM substrate. Nonetheless, there is an increased abundance of O in the background corrected color map at the positions where Zn is also found. In combination with the findings of the structural investigation shown in Fig. 37, it is concluded that the Ag cores are covered by a uniform ZnO shell.

5.6.2 Size distribution and surface coverage

In order to gain information about the size distribution of the deposited particles, the overall diameters and Ag core diameters of 208 spherically shaped nanoparticles (synthesized at 20 bar and 8 K) were individually determined from high-resolution STEM images. Examples for the STEM images can be found in Fig. 43 in the ESM. The results are shown in the histograms in Fig. 39, containing the measured overall diameters of the particles in panel (a) and the core diameters in panel (b). For both datasets the diameters are, in good approximation, normally distributed. A fit yields a mean overall particle diameter of 5.84 nm with a standard deviation of 0.93 nm and a mean core diameter of (3.03 ± 0.64) nm. The width of both size distributions is inherent to the He_N synthesis process and originates from the broad droplet size distribution [159]. Over 100 of the wire-like nanoparticles were measured and 70% of the particles have a length between 20

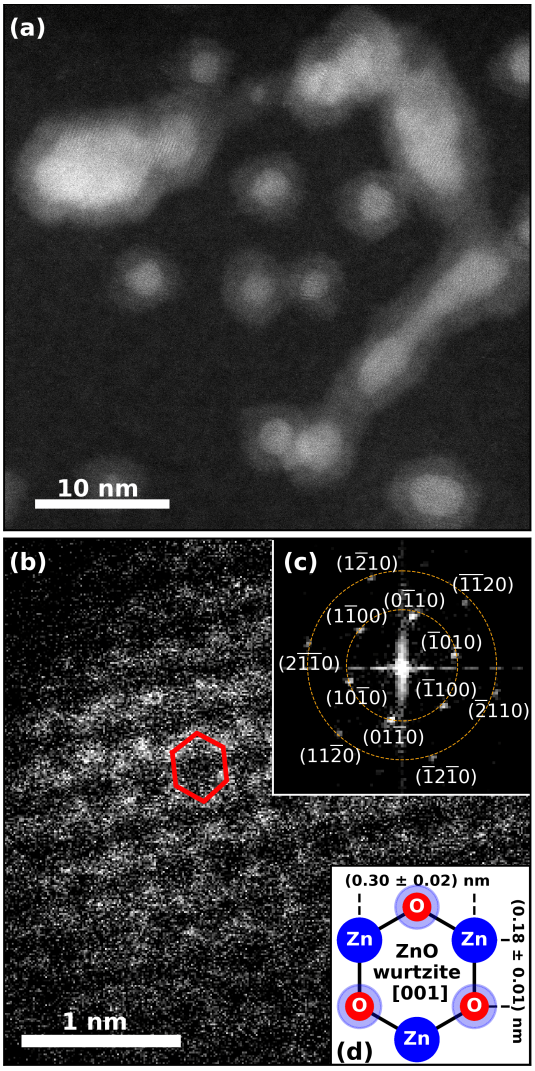

Figure 37: (a) STEM HAADF image of the synthesized Ag@ZnO nanosized particles. Spherically shaped as well as wire-like structures can be identified. The core@shell structure is clearly observable as silver cores appear brighter than zinc oxide shells. The smaller spherical particles and the elongated larger particles were created at different helium droplet beam conditions and were deposited on the same substrate subsequently (cf. chapter 5.3.1). (b) Detailed HAADF image showing ZnO along the [001] axis with the hexagonal structure highlighted in red for a selected unit cell. Inset plot (c) shows the fast Fourier transform (FFT) of the STEM image, yielding periodicities of (0.30 ± 0.02) nm and (0.18 ± 0.01) nm marked by the dashed orange circles. The sixfold symmetry of the FFT pattern is clearly observable and all visible features are assigned. The schematic in inset plot (d) explains the origin of the two observed lengths within the 2D projection of the hexagonal unit cell of wurtzite ZnO in [001] direction.

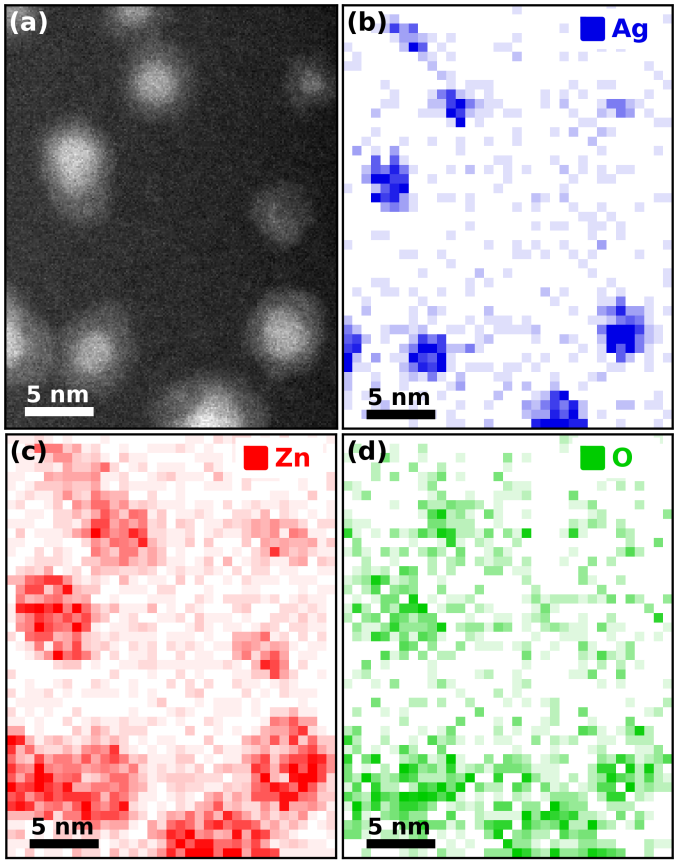

Figure 38: (a) Detailed STEM HAADF image of a selected region with spherically shaped Ag@ZnO core@shell nanoparticles. The spatially resolved EDS maps reveal the spatial distribution of (b) the Ag core material as well as (c) the Zn and (d) the O in the shell of the particles.

and 50 nm. Their diameter ranges from 6 to 8 nm, however, can extend to over 10 nm for agglomerated structures. Note that the diameter can vary over the length of a single particle and that most of them are kinked or branched, which makes an exact characterization of their size difficult.

For the determination of the surface coverage for the deposited nanoparticles the overview STEM images shown in Fig. 42 in the ESM were used. With the ImageJ 1.52p software package [199] it was possible to separately evaluate the spherical (deposition time: 40 min) and wire-like (deposition time: 3 min) particles due to a discrimination in size. This is shown in Fig. 45 in the ESM for one of the STEM images. The evaluation yields an estimation for the obtained surface coverage per hour of about $(9.3 \pm 0.5)\,\frac{\%}{\mathrm{h}}$ for the spherically shaped particles and about $(110 \pm 30)\,\frac{\%}{\mathrm{h}}$ for the elongated structures. The difference can be explained by the different helium droplet source conditions. For colder temperatures and larger droplets the deposition rate is enhanced, but a precise control of the particle

shape is no longer possible and a variety of different shapes is formed.

The determined surface coverage rate for the spherically shaped Ag@ZnO nanoparticles is used to estimate the coverage of the glass coverslips coated with ITO prepared for analysis in the NanoESCA system. All three samples (pure Zn, pure Ag, and Ag@ZnO) were produced under the same experimental conditions (20 bar at 8 K) with a deposition duration of 5 h each, resulting in an estimated surface coverage of about $(45.0 \pm 2.5)\,\%$. Since the decorated ITO substrate cannot be analyzed by STEM, a SEM overview image has been recorded, shown in Fig. 46 in the ESM. It confirms that the particles are distributed uniformly on the surface of the prepared samples, though the nanoparticles appear broadened at the given magnification due to the lower resolution of SEM.

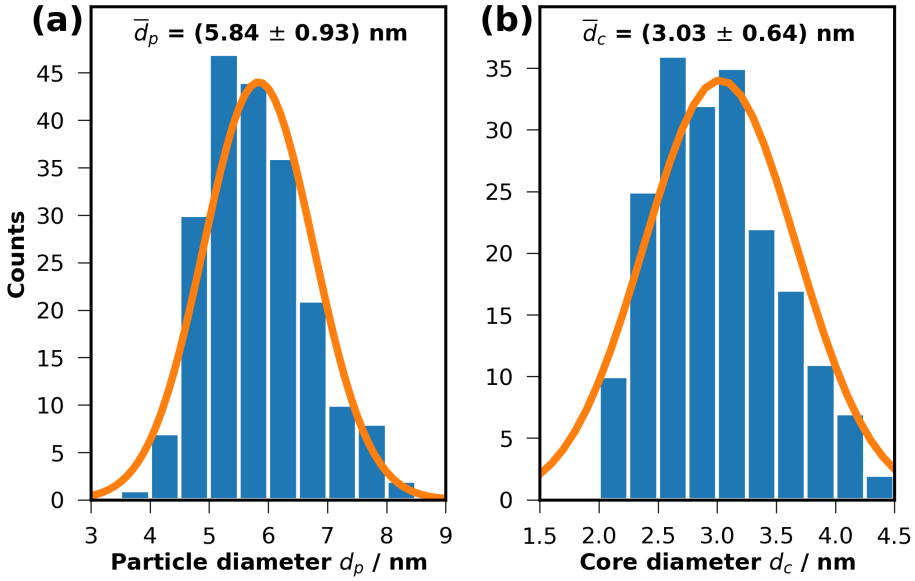

Figure 39: From high-resolution STEM images, the particle and core diameters of 208 spherically shaped Ag@ZnO nanoparticles were measured. (a) Histogram of the measured particle diameters with a fitted normal distribution yielding a mean particle diameter and standard deviation of $\overline{d}_p = (5.84 \pm 0.93)$ nm. (b) Histogram of the measured Ag core diameters with the normal distribution resulting in a mean of $\overline{d}_c = (3.03 \pm 0.64)$ nm.

5.6.3 Ultraviolet photoelectron spectroscopy

For the UPS and the 2PPE spectroscopy experiments with the NanoESCA system three different nanoparticle samples were prepared under the same conditions (20 bar at 8 K for 5 h) to guarantee comparability: pure Ag particles, ZnO particles and Ag@ZnO particles. All three samples are decorated with spherically shaped particles only, since it is of importance for the interpretation of the acquired

spectra that the shape is uniform and the size distribution narrow. The elongated wire-like structures, as shown in Fig. 37 (a), are kinked and exhibit a wider range of lengths and shape. Therefore, they are not further evaluated by the employed spectroscopic methods that yield results integrated over an extended surface area. Furthermore, the spherical Ag particles typically exhibit a localized surface plasmon resonance (LSPR) around 400 nm, which is accessible by the Ti:Sapphire laser system [200]. Glass coverslides coated with ITO, which were also characterized before particle deposition, were used as substrates. The samples were transported to the NanoESCA EF-PEEM under UHV conditions.

Selected regions of the UPS spectra obtained for Ag@ZnO particles on ITO are shown in Fig. 40 as a function of the binding energy E_{bind}. The spectra are normalized to the maxima of the secondary electron peak and the right part of the plot represents a zoom into the region around the Fermi cutoff. The solid lines represent the mean of five measurements at different sample spots, the 2σ confidence intervals are represented by the shaded areas. The blue line in Fig. 40 represents the acquired UPS spectrum of the plain ITO substrate before deposition and the orange line shows the signal of the Ag@ZnO particles after the transfer to the PEEM. The depicted region of interest in the left part of the diagram displays the energy range around the 3d core level peak of Zn. The orange line has a distinct and broad feature situated in this region with a double-peaked shape. A set of two Gaussians was used to evaluate the maxima of the convoluted peak structure. Thereby, the peak position at lower binding energy was found to be at (-9.7 ± 0.1) eV, marked by the vertical red line. The peak is attributed to the 3d level of pristine Zn. The second maximum, marked with a vertical black line, is located at (-10.3 ± 0.1) eV and represents the 3d level of the Zn atom in ZnO. A comparison with literature confirms the drawn conclusions about the origin of the peaks, though there is a certain spread in the published data [201–203]. The peak shift due to the chemical composition allows for a qualitative assessment of the oxidation state of the Zn atoms in the sample [204]. To ensure that the Zn is fully oxidized and the particles are comparable with the ones produced for the acquisition of the STEM data, the sample was exposed to ambient air for 1 h and then transferred back into the UHV chamber of the PEEM. The green line in Fig. 40 shows the UPS spectrum of the Ag@ZnO particles after the exposure to ambient conditions. The double peak structure is not present anymore, instead there is a single peak centered at (-10.8 ± 0.2) eV, which is again attributed to the 3d level of Zn in the oxidized state shifted to higher binding energies by 0.3-0.5 eV. This energy shift is an undesired side effect of the exposure to ambient air and the subsequent photo-hydroxylation of the sample surface driven by the extreme ultraviolet radiation during the acquisition of UPS

data. The observed artifact was investigated in more detail by Gutman *et al* in Ref. [205] for nano-crystalline zinc oxide thin films. Within the uncertainty of the measurement the energy shift found for the ZnO covered nanoparticles in this study is in good agreement with their results. However, the important conclusion is that there is no sign of any metallic Zn left in the shell. The inelastic mean free path of electrons in inorganic compounds, considering the 21.2 eV photon energy provided by the HIS, is at least ~ 1.5 nm [71]. As this value exceeds the shell thickness of the spherically shaped particles with (1.33 ± 0.15) nm, it is concluded that the shell is fully oxidized after the sample has been exposed to ambient air.

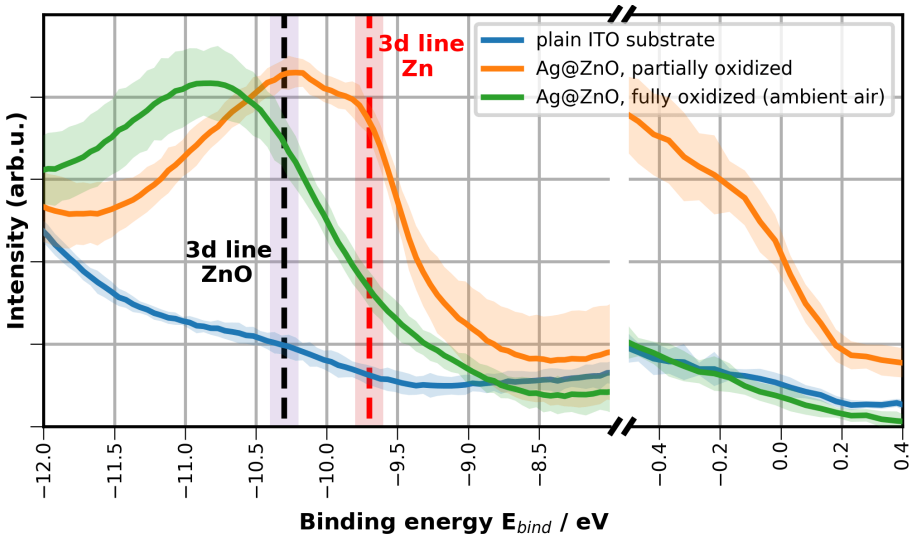

Figure 40: UPS spectra of the plain ITO substrate (blue), the partially oxidized Ag@ZnO nanoparticles after deposition (orange) and the fully oxidized Ag@ZnO particles after exposure to ambient air for 1 h (green). The peak positions for the double peak in the orange spectrum are marked by vertical lines in red at -9.7 eV and black at -10.3 eV and attributed to the 3d level of metallic Zn and of oxidized Zn, respectively. The acquired spectra are averaged over five different spots on the sample and the shaded areas represent the 2σ confidence levels.

The metallic nature of the partially oxidized Ag@ZnO is also reflected by the shape of the spectrum in the region that contains information about the population at the Fermi edge close to $E_{bind} = 0$ eV. A pronounced Fermi cutoff, the spectral signature of a metal, is clearly visible for the corresponding orange spectrum. For the conductive plain ITO substrate the cutoff is barely visible and it seems to be even more suppressed for the Ag@ZnO sample, which has been exposed to air. Considering that at a surface coverage of 45% the recorded spectra correspond to a superposition of both substrate and nanoparticles, the absence of

the Fermi cutoff indicates the fully oxidized, and thus semiconducting, ZnO as the dominant species.

Though this study aimed at the full oxidation of the Zn shell, there are intriguing possibilities for future experiments concerning the synthesis and formation of triple layer Ag@Zn@ZnO core@shell nanoparticles. The addition of a third layer, as already shown in literature, can potentially add new characteristics or improve existent properties of a layered nano-scaled system [206–208]. Furthermore, oxidation and reduction cycles could be applied to switch back and forth between Zn and ZnO as was already done e.g. for the Ni/NiO system [209]. Photoelectron spectroscopy offers a reliable method to discriminate between the metallic and semiconducting state and may be employed in future experiments to explore such systems and processes.

5.6.4 Two-photon photoelectron spectroscopy

2PPE spectroscopy is employed in order to investigate the plasmonic activity of the Ag cores within the Ag@ZnO nanoparticles. The 2PPE experiments are also carried out on ITO substrates covered only with spherically shaped nanoparticles and the conclusions in the following are drawn by comparing 2PPE spectra recorded for pure Ag and ZnO to Ag@ZnO samples. Note that the species containing Zn were already exposed to ambient air such that the shell is fully oxidized. The synthesis of Ag and Ag@ZnO nanoparticles took place at similar conditions ensuring that the plain Ag particles have about the same size as the Ag cores, with diameters in the range of 3-4 nm. For bare Ag nanoparticles in this size regime, it is known that the employed laser with a photon energy of 3.02 eV (410 nm) can excite localized surface plasmons [210, 211]. Note that the exact position of the LSPR also depends on the substrate and is, thus, not exactly known for the prepared particles on ITO. For particles produced by He droplet synthesis on fused silica, however, a relatively broad LSPR was found with a maximum around 450 nm [2].

In photoelectron spectroscopy, the electrons originating from the Ag core have to pass the ZnO shell in order to reach the detector. However, in contrast to the UPS measurements, the inelastic mean free path of the electrons after excitation with the laser beam is up to several tens of nm, which ensures that the acquired data contains information about the core material [71].

In order to compare the kinetic energy of the collected electrons, the work function (Φ) difference between the samples has to be accounted for. Φ was determined by intersecting the abscissa with a tangent through the turning point of the rising edge of the secondary electron peak in the collected spectra. In

addition, the Schottky effect, which emerges due to the presence of the 12 kV extractor field at a sample distance of 1.6 mm, has been considered [212] and introduces a reduction of Φ by $\Delta E = 104$ meV. The obtained work functions correspond to (3.7 ± 0.2) eV for ZnO, (4.2 ± 0.2) eV for Ag, and (4.0 ± 0.2) eV for Ag@ZnO. Since these values exceed the photon energy of the laser, it can be assumed that the spectra plotted as a function of E_{kin} in Fig. 41 correspond to electrons excited in a two-photon process with a maximum overall available energy of 6.04 eV (at the Fermi cutoff). For a comparable graphic presentation the signal intensities are normalized to the maxima of the secondary electron peaks of the spectra.

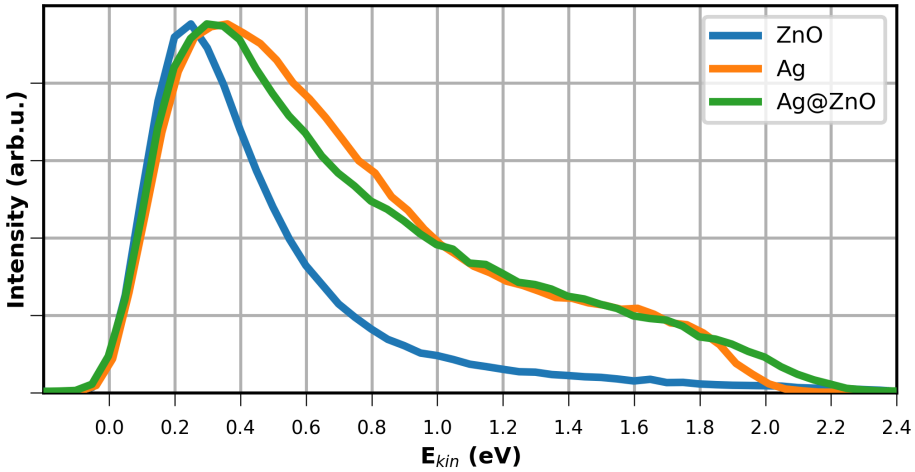

Figure 41: Two-photon photoelectron (2PPE) spectra of ZnO (blue), Ag (orange), and Ag@ZnO (green) nanoparticles on ITO irradiated with 3.02 eV (410 nm) p-polarized laser light. The significant increase of the electron yield at higher kinetic energies is attributed to an enhancement by the excitation of Ag surface plasmons.

In Fig. 41 it can be seen that the 2PPE spectrum of ZnO, depicted in blue, shows a prominent secondary electron peak that decays fast with increasing electron kinetic energy with only a very weak signal intensity towards the Fermi cutoff. However, in the case of the Ag spectrum (orange) a significant enhancement of electron yield at higher kinetic energies is observed. Such an increase in high energy photons has been attributed to an enhancement of the surface electric field by the excitation of plasmons in Ag nanoparticles [200, 213]. Intriguingly, the Ag@ZnO spectrum closely resembles the form of the plain Ag spectrum. Consequently, it is concluded that also in this case a localized surface plasmon is excited. The precise origin of the electrons, however, remains elusive. Plasmon excitation in the Ag core leads to an enhancement of the electric field close by the nanoparticle such that the photoelectrons may either be created in the Ag

or the ZnO shell. Furthermore, in contrast to the plain Ag particles that were kept under UHV conditions, the Ag@ZnO particles were exposed to ambient air. The ZnO shells provide a protective layer preventing a contamination of the Ag cores with water or other hydrocarbons, while still preserving their plasmonic properties.

5.7 Conclusions

In the course of this study, we showed a novel way to produce high quality Ag@ZnO core@shell nanoparticles by employing the helium nanodroplet synthesis approach. Compared to other synthesis routes, this technique has the advantage of utilizing superfluid helium as pristine "nanolabs" in which the particles are grown without the addition of any solvents or other chemical agents. Thorough STEM investigations reveal the uniform and evenly distributed shape of the wurtzite ZnO shells surrounding the Ag cores, not only for spherically shaped particles but also for larger, wire-like core@shell structures. Thereby, the ZnO provides a very stable and reliable protective cover for the plasmonic Ag cores. This is indicated by 2PPE spectroscopy, where a significant plasmon enhancement of the photoelectron yield is observed for plain Ag as well as Ag@ZnO core@shell nanoparticles. Furthermore, the oxidation state of the Zn/ZnO shell system was investigated by accessing the Zn 3d core level with UPS, opening up possible routes for the synthesis and *in situ* monitoring of triple layer Ag@Zn@ZnO core@shell systems on the nanoscale. The stability of the Ag@ZnO nanoparticles and the preservation of important functional features upon exposure to ambient conditions sets the ground for possible future applications outside of the laboratory environment.

5.8 Supplementary Material

5.8.1 Additional STEM images of Ag@ZnO nanoparticles

Additional sets of high-angle annular dark-field (HAADF) scanning transmission electron microscopy (STEM) images in different magnifications are provided to complement the information about sizes, shapes, and distribution of the synthesized nanoparticles on the amorphous carbon support. The four images in Fig. 42 give an overview at lower magnification. Note that in panel (b) the scale differs from the other images. It can be observed, that elongated and kinked wire-like nanoparticles exhibit a broad distribution of sizes and lengths. Some of these larger particles are folded and form broad and massive structures upon

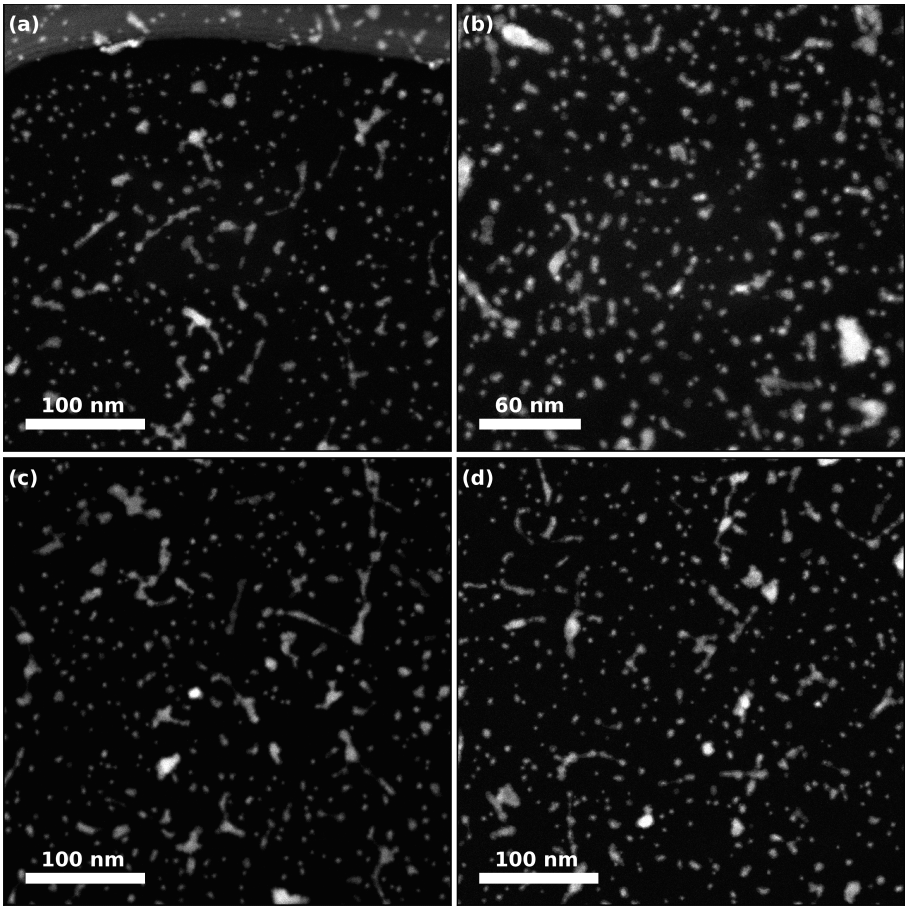

Figure 42: (a)-(d) HAADF STEM overview images of the Ag@ZnO nanoparticles deposited on an amorphous carbon support. Both synthesized particle types are present: smaller spherically shaped and elongated, kinked wire-like nanoparticles. An example for the analysis of the surface coverage using these STEM images is presented in Fig. 45. Contrast and brightness of the images were adjusted for better visibility.

deposition. The smaller spherical nanoparticles, on the other hand, appear very regularly distributed, as discussed in the main manuscript.

In Fig. 43 the nanoparticles are shown in more detail at higher magnifications. Panels (a)-(c) focus on spherically shaped particles, while in panel (d) examples for wire-like structures can be seen. As noted also in the main manuscript, a ZnO shell with uniform thickness is formed around the Ag cores for both particle types.

5.8.2 ZnO structure determination

To support the conclusion that in the synthesized particles the ZnO shell preferably forms in a wurtzite structure, another set of HAADF STEM images, in which

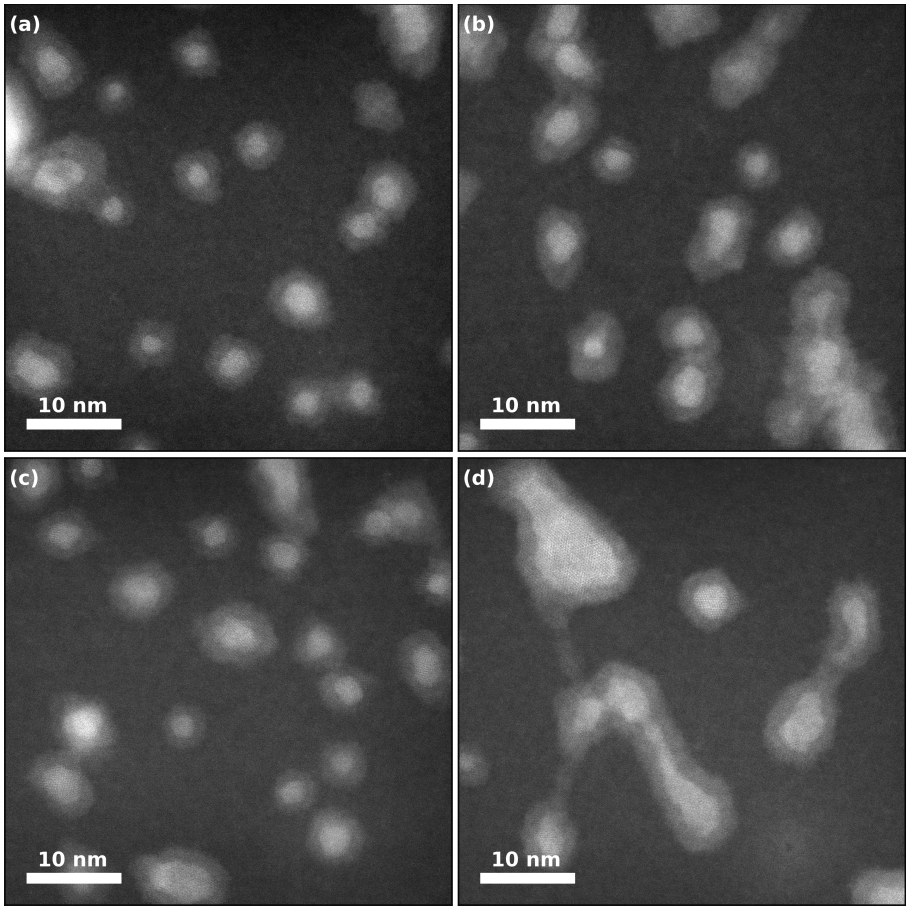

Figure 43: High magnification HAADF STEM images of Ag@ZnO nanoparticles deposited on an amorphous carbon support. (a)-(c) Areas on the sample where mostly spherical nanoparticles are present, which were synthesized at 20 bar and 8 K with a deposition time of 40 min. The particle shape and size are uniformly distributed. As the deposition process is random, some particles are deposited on top of each other or in such proximity that they are connected. (d) Wire-like particles, synthesized at 20 bar and 5 K with a deposition time of 3 min, showing an example of possible sizes and shapes. Note that for both types of nanoparticles the ZnO shell layer is very uniform and completely covers the Ag core. Contrast and brightness of the images were adjusted for better visibility.

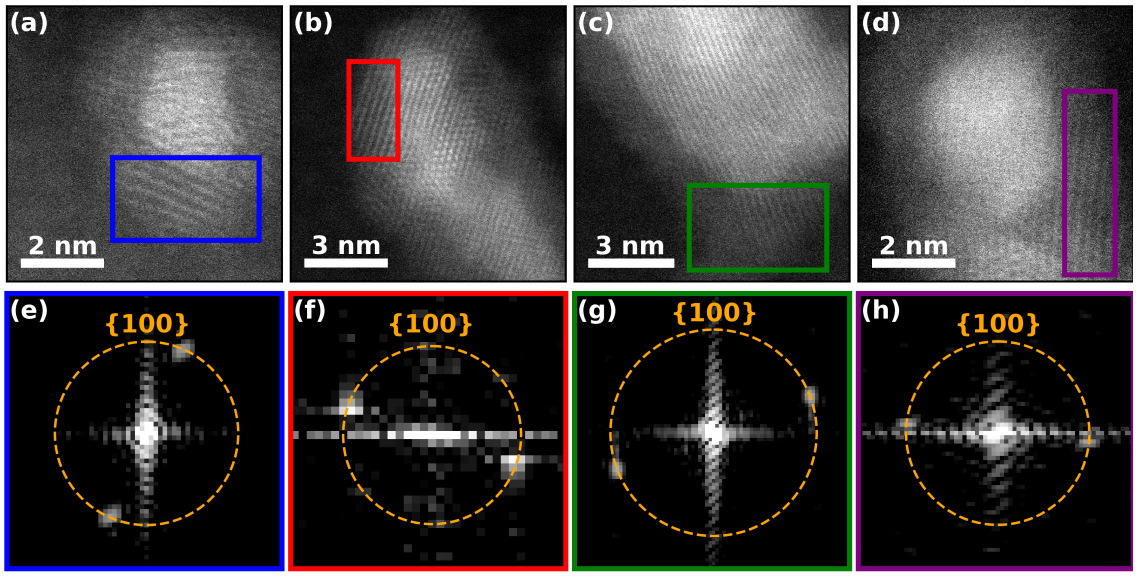

Figure 44: (a)-(d) HAADF STEM images at high magnification showing parts of spherically shaped and wire-like Ag@ZnO nanoparticles. Areas of the ZnO shell, where a lattice structure is clearly visible, are marked as ROIs with colored frames. Contrast and brightness of the images were adjusted for better visibility. (e)-(h) FFT images obtained from the ROIs showing the diffraction patterns. The found lattice distances from left to right are (0.30 ± 0.03) nm, (0.28 ± 0.03) nm, (0.28 ± 0.02) nm, and (0.28 ± 0.03) nm, respectively. They can all be assigned to the {100} planes of wurtzite ZnO as indicated by the annotation of the orange circles.

lattice plans are visible, is presented in Fig. 44 in the top panels (a)-(d). The region of interest (ROI) in every image, where the ZnO lattice is clearly visible, is marked by a colored frame. The respective fast Fourier transform (FFT) images obtained from the ROIs are shown in Fig. 44 in the bottom panels (e)-(h). Only selected areas of the ZnO shells in the STEM images are used for the generation of FFT data to avoid any influence of the Ag cores, which would impact the obtained data and obscure the lattice spacing of ZnO. Note that the FFT images are not at the same scale due to the varying sizes of the ROIs.

The diffraction spots visible in the FFT images correspond to the crystal planes in the ROIs. The obtained lattice spacing is (0.30 ± 0.03) nm for panel (a), (0.28 ± 0.03) nm for panel (b), (0.28 ± 0.02) nm for panel (c), and (0.28 ± 0.03) nm for panel (d). All measured lattice distances can be assigned to the {100} planes of wurtzite ZnO with a reported lattice spacing of 0.2814 nm, obtained from the Crystallography Open Database (COD) [197].

5.8.3 Surface coverage evaluation

The employed procedure for the evaluation of the surface coverage with nanoparticles obtained by synthesis with the helium nanodroplet approach is exemplary shown in Fig. 45. The HAADF STEM image shown in panel (a), serving as starting point, is modified with help of the ImageJ 1.52p software package [199]. From this image a mask plot, as displayed in panel (b), is generated. Discriminating by particle sizes allows for the creation of mask plots containing only smaller spherically shaped nanoparticles, shown in panel (c), or wire-like structures, as presented in panel (d). This procedure was applied to all four overview images shown in Fig. 42 and yielded an estimated average rate for the surface coverage of $(9.3 \pm 0.5)\,\frac{\%}{\mathrm{h}}$ for the spherically shaped particles and about $(110 \pm 30)\,\frac{\%}{\mathrm{h}}$ for the wire-like structures, as stated in the main manuscript. For lower source temperatures and larger helium droplets the deposition rate, which can be achieved by the approach, is strongly enhanced.

5.8.4 SEM imaging of nanoparticle sample

Scanning electron microscopy (SEM) provides an additional imaging method with a resolution in the nm regime. It can be used for substrates that cannot be investigated by STEM because of constraints concerning the sample thickness or size, as, for example, the glass coverslips coated with indium tin oxide (ITO) in this work. Consequently, in order to obtain information on the substrates decorated with spherically shaped nanoparticles (source conditions: 20 bar and 5 K, deposition time: 5 h) for analysis in the NanoESCA system, SEM was used as additional analysis method. Figure 46 shows an overview image of the spherical Ag@ZnO nanoparticles on the ITO surface. The SEM image was taken with a Zeiss Sigma 300 VP scanning electron microscope. The inlens detector for secondary electrons (Inlens SE) and an acceleration voltage of 15 kV at a working distance of 2.3 mm were used for the measurement. It can be seen in Fig. 46, that the nanoparticles are uniformly distributed on the ITO surface. Note that at the given magnification the bright spots associated with the particles appear enlarged.

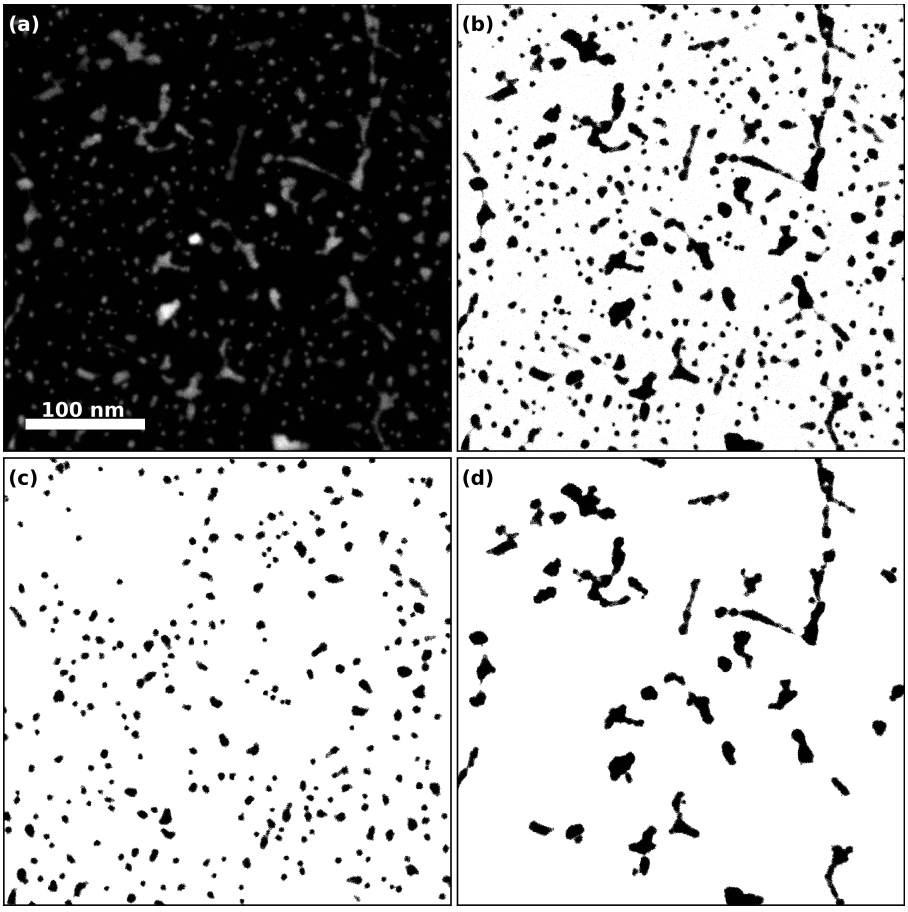

Figure 45: (a) HAADF STEM overview image with both nanoparticle types deposited on amorphous carbon. (b) A mask plot, marking all of the deposited particles, was obtained by introducing a brightness threshold to the STEM image and is further discriminated by particle size. This leads to a mask plot in panel (c), containing only smaller spherically shaped nanoparticles, and yields an estimated rate for the surface coverage of 9 $\frac{\%}{\mathrm{h}}$. (d) A mask plot for the longer wire-like structures yields an estimate for the surface coverage rate of 136 $\frac{\%}{\mathrm{h}}$.

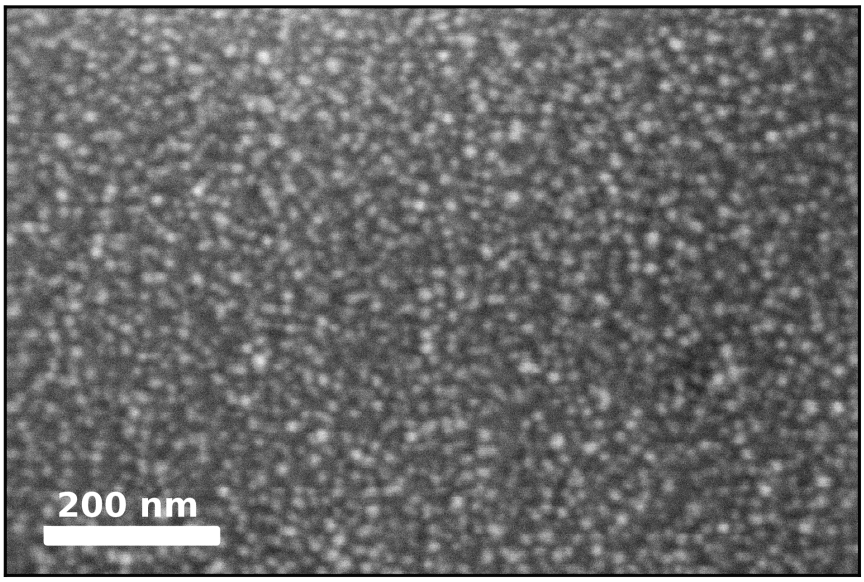

Figure 46: Overview SEM image of Ag@ZnO nanoparticles deposited on an ITO substrate for analysis in the NanoESCA system with a deposition time of 5 h. The sub-monolayer of nanoparticles is uniformly distributed on the surface.

6 Synthesis and Characterization of CoO Nanowires

The content of this chapter corresponds to the following peer reviewed and published scientific paper:

> "Ultrashort XUV pulse absorption spectroscopy of partially oxidized cobalt nanoparticles" by **Alexander Schiffmann**[7], Benjamin W. Toulsen[8], Daniel Knez[9], Roman Messner[7], Martin Schnedlitz[7], Maximilian Lasserus[7], Ferdinand Hofer[9], Wolfgang E. Ernst[7], Oliver Gessner[8], and Florian Lackner[7] in *Journal of Applied Physics* **127**, 184303 (2020).
> `https://doi.org/10.1063/5.0004582`

The author of this doctoral thesis contributed to the publication in the following ways:

- Assistance with the design and execution of the experiment
- Synthesis of the nanoparticles
- Assistance with the evaluation and interpretation of the data obtained by electron microscopy
- Co-authorship and editing of the manuscript

All co-authors were engaged in the preparation and publication process of this paper. Their affiliations and a short recapitulation of their major contributions are given below:

Benjamin W. Toulson:
Conduction of the XUV absorption measurements.

Daniel Knez:
Recording of the electron microscopy data (STEM) and editing of the manuscript.

Roman Messner:
Assistance with the experiments and the interpretation of the acquired data and editing of the manuscript.

[7]Institute of Experimental Physics, Graz University of Technology, Petersgasse 16, A-8010 Graz, Austria

[8]Chemical Sciences Division, Lawrence Berkeley National Laboratory, Berkeley, California 94720, USA

[9]Institute of Electron Microscopy and Nanoanalysis & Graz Centre for Electron Microscopy, Graz University of Technology, Steyrergasse 17, A-8010 Graz, Austria

Martin Schnedlitz:
Assistance with the experiments.

Maximilian Lasserus:
Assistance with the experiments.

Ferdinand Hofer:
Supervision and funding for electron microscopy.

Wolfgang E. Ernst:
Scientific advice, funding, and editing of the manuscript.

Oliver Gessner:
Scientific advice, supervision, and funding for absorption spectroscopy.

Florian Lackner:
Design of the experiment, sample transfer to the Lawrence Berkeley National Laboratory and conduction of the XUV absorption measurements, supervision, funding, and authorship of the manuscript.

The authors of this publication gratefully acknowledge additional support provided by the Austrian Science Fund (FWF) under Grant No. P30940-N36, NAWI Graz, and the Österreichische Forschungsgemeinschaft (ÖFG). BWT and OG are further supported by the U.S. Department of Energy, Office of Science, Office of Basic Energy Sciences, Chemical Sciences, Geosciences and Biosciences Division, through Contract No. DE-AC02- 05CH11231.

6.1 Abstract

High-order harmonic generation (HHG) based transient XUV absorption spectroscopy is an emerging technique to trace photoinduced charge carrier dynamics in condensed phase materials with femtosecond and even attosecond temporal resolution and elemental specificity. However, its application to nanoparticulate samples that are relevant, for example, for novel photocatalytic light harvesting concepts, has been limited. This is in part due to the challenge to produce residual-free samples on ultrathin, XUV-transparent substrates as well as a widespread understanding that sparsely distributed nanoparticles do not provide sufficient contrast for XUV absorption measurements. Here, we present static XUV absorption spectra of partially oxidized Co nanowire-structures with diameters of approximately 4.5 nm and lengths between 10 and 40 nm, recorded with an ultrashort pulse HHG light source. Nanoparticles are synthesized by agglomeration of Co atoms inside superfluid helium droplets, followed by surface deposition and oxidation in ambient air. The method is uniquely suited for residual-free synthesis of transition metal nanowires and their deposition on ultrathin substrates. Analysis by high-resolution transmission electron microscopy reveals the formation of CoO nanowires with regions of unoxidized Co in their interior. The nanoparticle samples are investigated in an HHG-driven ultrafast XUV absorption setup. Despite the low surface coverage of only 23%, the recorded spectrum exhibits a distinct absorption feature at the Co $M_{2,3}$(2p) edge near 60 eV with a peak height of about 40 mOD. The results support the feasibility of table-top ultrafast transient XUV absorption studies of photoinduced dynamics in transition-metal oxide nanoparticles with sub-monolayer surface coverage.

6.2 Introduction

Small nanoparticles possess interesting properties that are very different from their macroscopic bulk counterparts owing to the increased surface-to-volume ratio and quantum confinement effects, which emerge when approaching the 10 nm size regime [214]. In particular, metal and transition-metal nanoparticles consisting of earth-abundant materials bear great potential for photocatalytic and photovoltaic devices, providing a route toward a greener and more sustainable energy infrastructure [215, 216]. The underlying physical and chemical processes are driven by charge carrier dynamics proceeding on extremely fast time-scales, making it challenging to disentangle them by conventional, time-averaged methods. Here, we demonstrate that ultrafast XUV absorption spectroscopy may be used for element-specific probing of partially oxidized Co nanowires. The

nanoparticles are produced by quantum-vortex enabled synthesis in superfluid helium nanodroplets and deposited on ultrathin substrates with sub-monolayer coverage. The results indicate that in future experiments, transient XUV absorption spectroscopy can be used to study ultrafast charge carrier dynamics [217–219] in metal/metal oxide nanoparticles, potentially, with a temporal resolution in the attosecond regime.

The synthesis of CoO nanoparticle catalysts [220] typically involves solvents and surfactants [221,222]. Spherical particles may also be produced using sputtering techniques [223] or laser ablation [220]. Helium droplet assisted nanoparticle synthesis [123,159] provides a means for the residual-free production of nanowire samples, which are particularly well suited for investigation by ultrahigh vacuum techniques such as XUV absorption spectroscopy. In this method, superfluid helium droplets pick up gas-phase Co atoms [17,18], which preferentially agglomerate along the cores of quantum vortices [31,192,193]. The subsequent deposition on the substrate is cushioned by the evaporating helium [33], resulting in very pure particles as no solvents or surfactants are involved in either the synthesis or the deposition. The accessible size regime of the formed nanoparticles ranges from small, spherical clusters with diameters below 5 nm to elongated wires up to a few 100 nm in length [35, 120, 121, 123], depending on the doping rate and droplet size [27]. The stability of such nanowire-structures is governed by surface diffusion processes [30, 80]. Once exposed to air, deposited transition metal particles can undergo oxidation [50, 194]. For Co nanoparticles it has been shown that an initial CoO shell layer (< 1 nm) is formed rapidly around a metallic Co core, the shell thickness increases as the oxidation process proceeds on a time scale of several hours [224, 225].

We synthesize nanowires formed by helium nanodroplet deposition of metallic Co particles on 10 nm thick Si_3N_4 substrates and their subsequent exposure to ambient air. The method is ideal for the decoration of fragile, ultrathin substrates due to the soft landing process [1], and generates new possibilities for ultrafast XUV- and X-ray studies of nanostructured materials. The samples are characterized by high-resolution transmission electron microscopy (HR-TEM) and energy-dispersive X-ray spectroscopy (EDXS). Diffractograms obtained from HR-TEM images allow for an analysis of the sample composition and oxidization state.

High-order harmonic generation (HHG) based techniques are well established for studying ultrafast dynamics in atoms and molecules in the gas-phase, liquids and solids using transient reflection, absorption or photoelectron spectroscopy [83,226]. Small nanoparticles, however, have only very recently been probed with HHG based methods employing photoelectron spectroscopy [227] but have so far

not been studied in absorption. We present a first investigation of nanoparticles with sub-monolayer surface coverage using HHG based static XUV absorption spectroscopy. The results support the feasibility of future experiments to study photoinduced dynamics in metal oxide nanoparticles with femto- or attosecond temporal resolution [217–219].

6.3 Experimental Methods

6.3.1 Nanoparticle synthesis

Cobalt nanoparticles are formed by synthesis in helium nanodroplets, details of the employed apparatus can be found in Ref. 124. In brief, high purity helium gas (99.9999%) is expanded under high pressure (20 bar) through a 5 μm nozzle into vacuum. At a nozzle temperature of 5.4 K, this leads to the generation of helium droplets consisting, on average, of $\approx 1.7 \times 10^{10}$ He atoms, corresponding to a radius of approximately 570 nm [125]. Subsequently, the He droplets enter a pickup chamber where they pass an oven assembly containing a resistively heated Al_2O_3 basket (estimated temperature: $\approx$ 1300°C) filled with metallic Co. After pickup of Co atoms by the droplets, metal nanoparticles are formed through collisions of Co-atoms inside the doped, cold ($\approx$ 0.4 K) helium environment [228]. Rotation of the nanodroplets leads to the emergence of quantum vortices [192], which attract dopant atoms through hydrodynamic forces and enhance agglomeration along the vortex cores [27, 31, 193]. The resulting elongated metal particles [35, 120, 121] are deposited on substrates by placing either a $0.5 \times 0.5\,mm^2$, 10 nm thick Si_3N_4 substrate (Norcada NT050Z) or an amorphous carbon grid into the doped droplet beam.

The Si_3N_4 substrates are used for the XUV absorption experiments whereas carbon grids are employed to characterize the particles by transmission electron microscopy (TEM). Note that even though the carbon grids are thinner ($\approx$ 3 nm) than the Si_3N_4 substrates, they cannot be used for XUV absorption spectroscopy as the ultrathin regions are confined to small areas supported by a thick mesh grid structure. However, carbon grids allow for better contrast in the TEM images, considering the small diameters of the particles and the relatively light elements involved.

The Co vapor pressure is adjusted for maximum pickup- and deposition rate, which is measured with a quartz crystal microbalance inserted into the He droplet beam before and after deposition. The total deposition time per sample was 120 min. Both samples are prepared under the same synthesis and deposition conditions. After deposition, for both substrates the nanoparticles are exposed to

ambient air for about 1 hour, leading to partial oxidation (see below). In principle, the degree of oxidation can be controlled by the exposure time. The Si_3N_4 sample was stored in Ar during transport to the XUV setup.

6.3.2 Transmission electron microscopy

A Tecnai F20 (FEI Company) high-resolution transmission electron microscope (HR-TEM) is used to study the structure and chemical composition of the deposited nanoparticles. Measurements are performed at an acceleration voltage of 200 kV. The microscope is equipped with a high resolution Gatan imaging filter including an UltraScan CCD camera (2048×2048 pixels^2), which is used for the acquisition of the micrographs. For energy-dispersive X-ray spectroscopy (EDXS) an EDAX Sapphire Si(Li) detector is used.

6.3.3 XUV absorption spectroscopy setup

The ultrafast XUV setup has been described elsewhere [85,86]. HHG is performed by focusing 50% of the output of a 785 nm, 3.3 mJ, 3 kHz, 40 fs full-width-at-half-maximum (FWHM) Ti:Sapphire laser system into a semi-infinite gas cell filled with about 150 Torr of neon. A quasi-continuous XUV spectrum consisting of overlapping harmonics is generated, spanning the range from 48 to 72 eV photon energy. Harmonics beyond 72 eV and the remaining light from the IR driving laser are suppressed by Al filters. The XUV beam is focused to a 1/e diameter of about $(23 \pm 5)\,\mu$m (determined by a knife-edge scan) at the sample using a toroidal mirror. After passing through the sample, the XUV beam is spectrally dispersed by a concave spherical variable-line-spacing grating. The XUV spectrum is detected by an X-ray CCD camera.

To record XUV absorption spectra of the nanoparticles, the sample is repeatedly driven in and out of the XUV beam, recording reference spectra (I_{ref}) without the sample and spectra with the sample inserted (I_{sig}) for 30 s each. The recorded spectra are given in units of optical density: $OD = \log(I_{ref}/I_{sig})$. Data presented here correspond to an average over six individually recorded spectra, i.e., a total data acquisition time of 6 minutes.

6.4 Results and Discussion

Representative TEM images of the fabricated cobalt nanoparticles are shown in Figure 47, panel a.) and b.), at two different scales. At the chosen synthesis conditions, the obtained nanostructures are comprised of short nanowires, some of which agglomerated to larger structures or lie on top of each other while some

particles remain separated. After deposition, the nanoparticles can oxidize during exposure to air for about 1 hour.

Images recorded at different positions on the TEM grid are analyzed with the FIJI software package [199], revealing an average surface coverage of about $(23 \pm 6)\%$ (uncertainties refer to 95% confidence intervals). The mean diameter of the nanowire-like particles is estimated from the images to (4.5 ± 1.5) nm, and the length between 10 and 40 nm. A more detailed analysis of particle diameters and lengths can be found in the Supplementary Material.

Energy-dispersive X-ray spectroscopy (EDXS) of areas containing complexes of fused deposited nanoparticles reveals the presence of both cobalt as well as oxygen. A representative EDXS spectrum is shown in the inset in Figure 47 a.). Consequently, the nanowires in the TEM images are interpreted as oxidized cobalt nanoparticles. The dark spots in the particles may be caused by an increased sample thickness in regions where nanoparticles are deposited on top of each other or where agglomeration leads to an increased diameter. However, it is also possible that unoxidized metallic Co inside the particles contributes to the darker areas.

Oxidation initially proceeds at the surface of the nanoparticles. It is known that metallic Co inside the particles initially resists the oxidation process, leading to the formation of Co@CoO core@shell nanoparticles [224, 225, 229]. While the initial oxidation leads to the formation of a < 1 nm thick shell layer within several minutes, additional oxidation proceeds on a much slower time-scale, on the order of several hours [225]. This suggests that the formed nanoparticles mainly consist of cobalt oxide, with regions of unoxidized metallic Co in their interior.

The two common oxidation states of cobalt are CoO [cobalt(II) oxide] and Co_3O_4 [cobalt(II,III) oxide]. Previous studies employing different synthesis methods showed that upon exposure to oxygen at room temperature, Co-nanoparticles prefer the cobalt(II) oxide form [224, 229, 230]. In order to reveal the stoichiometry of the He droplet synthesized cobalt oxide nanoparticles, an analysis of diffractograms for selected nanoparticles is performed. The diffractograms are obtained by fast Fourier transformation (FFT) of TEM images that exhibit periodic structures corresponding to the crystal lattice. CoO has a rock salt crystal structure (cubic, $Fm\bar{3}m$), consisting of two interpenetrating fcc sublattices of Co^{2+} and O^{2-}. The lattice constant of CoO is 0.426 nm whereas the lattice constant for spinel Co_3O_4 (cubic, $Fd\bar{3}m$) is 0.808 nm [231]. An example of this approach can be seen in Figure 48, which shows a HR-TEM image at high magnification. The inset shows a diffractogram obtained from the top most nanoparticle to the left of the inset. Diffraction spots are clearly visible and can be assigned. Note that the presented diffractogram has been corrected by employing a bandpass filter in

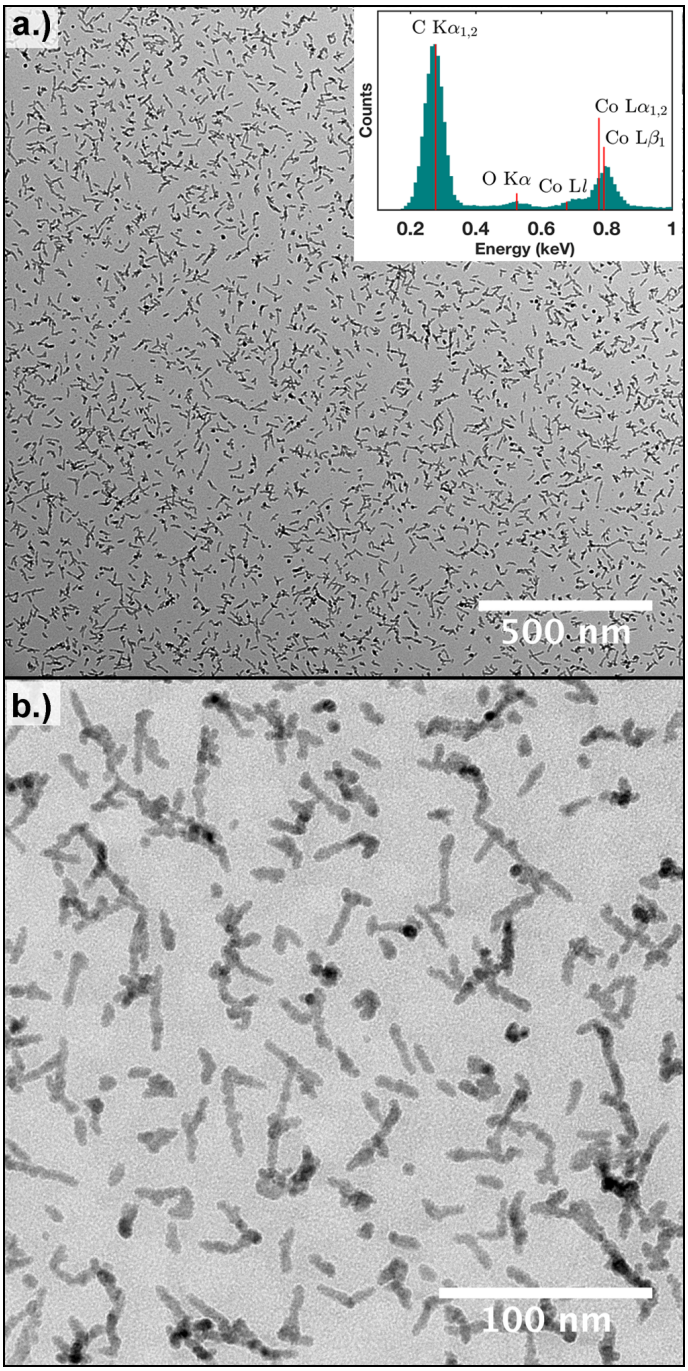

Figure 47: Panels a.) and b.) show HR-TEM images of the produced nanoparticles at two different scales. The nanoparticles exhibit wire-like structures, some of which are fused together. The inset in panel a.) features a section of the recorded EDXS spectrum, which exhibits a carbon peak originating from the substrate, as well as cobalt and oxygen features associated with the nanoparticles.

order to improve the visibility of the diffraction spots.

In total, 9 images with a comparable resolution as in Figure 48, each containing a few nanoparticles, have been analyzed. Additional images can be found in the Supplementary Material. Among the identified diffraction spots, the most abundant lattice distances are found around 0.24 nm and 0.21 nm, which match the lattice distances of the CoO (111) and (200) planes with 0.246 nm and 0.213 nm, respectively (see Supplementary Material) [224]. Note that these planes give rise to the two main features in X-ray powder diffraction experiments on CoO [232], followed by less intense diffraction peaks below 0.15 nm. The uncertainty of the measurement is estimated with about 0.01 nm. Furthermore, we also find lattice distances between 0.18 nm and 0.21 nm, indicating the presence of pristine Co, which exhibits diffraction features in this range [233]. At room temperature and exposure to ambient air, it has been shown that hcp α-Co (hexagonal, $P6_3/mmc$) is preferentially formed [234]. However, the fcc phase β-Co (cubic, $Fm\bar{3}m$) exhibits prominent features in this range as well (see Table 3 in the Supplementary Material). We do not find any lattice distances larger than 0.25 nm, which would be clear evidence for the formation of Co_3O_4. If present, one would expect diffraction spots associated with lattice distances of 0.286 nm and 0.467 nm [229], corresponding to the (220) and (111) planes, respectively [224, 235].

The lattice distances for selected particle areas are indicated in Figure 48, associated with the (111) and (200) planes of CoO and the (200) plane of Co. Based on this analysis, we conclude that the nanowires consist predominantly of CoO. However, the presence of metallic Co lattices in the particles clearly shows that some particles contain regions with unoxidized Co in their interior, in agreement with previous results [224, 225].

With the structure and composition of the deposited nanoparticles determined from the TEM images and EDXS data, we proceed in the following to demonstrate the feasibility of ultrafast XUV absorption spectroscopy as a means to investigate these particles. Note that the TEM analysis employs amorphous carbon grids while the XUV absorption experiments are carried out using ultrathin Si_3N_4 substrates. However, previous experiments on metal particles synthesized using the He droplet approach showed no differences between silicon nitride [8] and carbon [50] substrates. The helium droplet source conditions (20 bar, 5.4 K), which determine the particle size and structure, as well as the deposition time (120 min) are identical for both employed substrates.

Figure 49 shows an XUV absorption spectrum (black) of the deposited nanoparticles on a 10 nm thick Si_3N_4 substrate. Absorption spectra are obtained by recording reference spectra without sample (I_{ref}) and spectra with sample inserted (I_{sig}) in the XUV beam and are given in units of optical density:

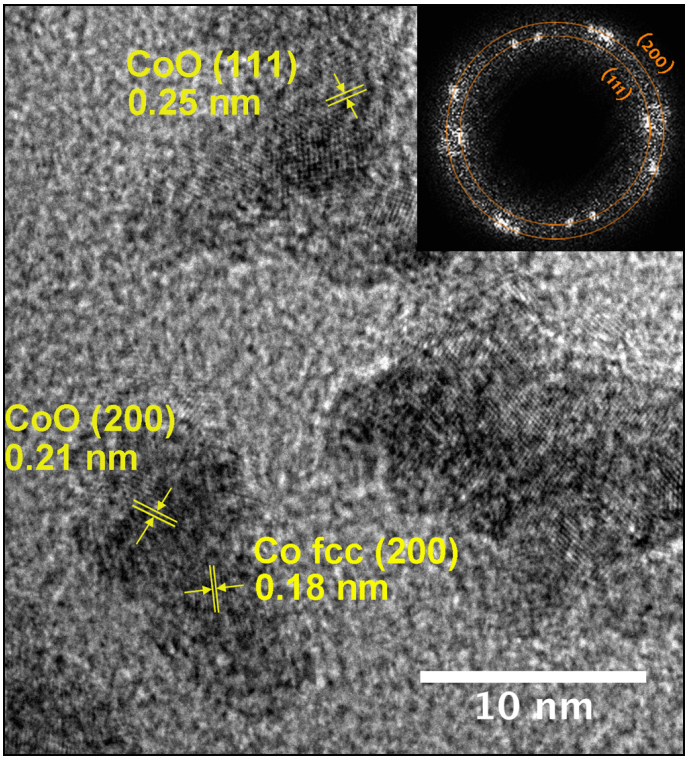

Figure 48: Close up of a selected HR-TEM image region. Co and CoO lattices are indicated with arrows for selected particle areas. The inset shows a fast 2D Fourier transform of the area where the top most nanoparticle is located (to the left of the inset), revealing diffraction spots associated with the (200) and (111) planes of CoO [224].

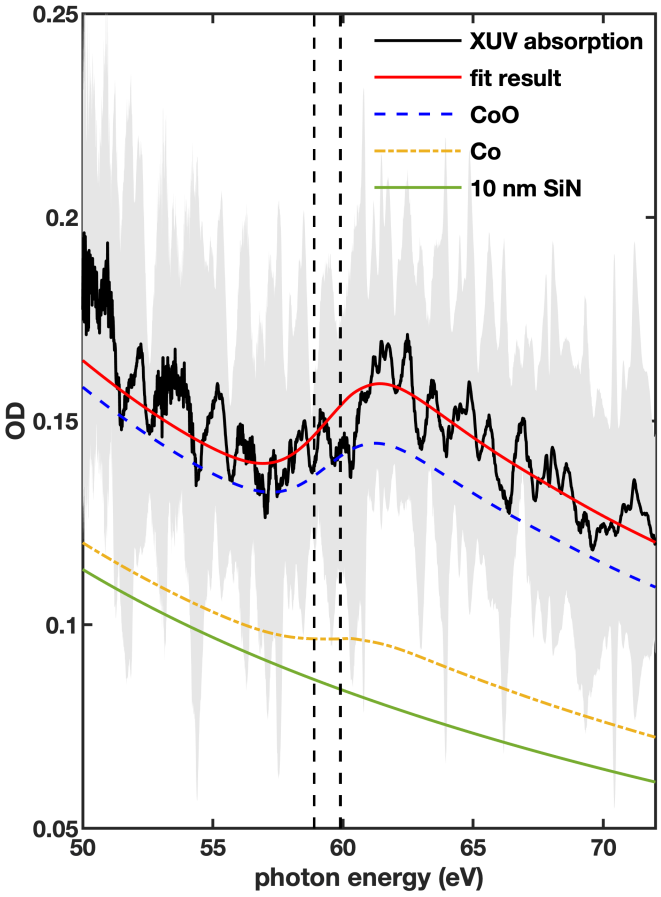

Figure 49: XUV absorption spectrum of a sub-monolayer of nanoparticles deposited on a 10 nm thick Si_3N_4 substrate. The black spectrum is plotted together with a grey-shaded 1σ uncertainty range. The spectrum is well described by a simulation (red), consisting of a superposition of XUV absorption spectra of Co (orange), CoO (blue) and the Si_3N_4 substrate (green) [236]. Note that the plotted Co and CoO components include the substrate effect as offset. The spectrum has been recorded within 6 minutes of total exposure time using a laboratory-based HHG source.

$OD = \log(I_{ref}/I_{sig})$. The presented spectrum is derived by averaging over 6 static absorption spectra, followed by application of an FFT-based smoothing algorithm. The grey shaded area in Figure 49 corresponds to the 1σ uncertainty range of the unsmoothed signal. The Co M_2 ($3P_{1/2}$) and M_3 ($3P_{3/2}$) absorption edges are located at 58.9 eV and 59.9 eV, respectively (indicated by vertical dashed lines) [237]. The corresponding increase in absorption can clearly be identified in the recorded spectrum, peaking around 62 eV. The peak height is approximately 40 mOD with respect to a background, which has been estimated by extrapolating the signal from 50 to 55 eV with an exponentially decreasing function.

The recorded XUV absorption spectrum is described by a superposition of individual Co (orange) and CoO (blue) spectra, as well as a contribution from the Si_3N_4 substrate (green). Co_3O_4 is not considered based on the results of the TEM analysis. Component spectra are taken from the online database of the Center for X-ray Optics (CXRO) [236]. A least-squares fit procedure is performed based on the function $OD(E) = OD_{Si}(E) + a\,OD_{CoO}(E) + b\,OD_{Co}(E)$, which includes the contributions of the three materials to the overall absorption and two free fit parameters, a and b, in order to describe the total optical density (OD) of the sample as a function of the photon energy E. $OD_{CoO}(E)$ and $OD_{Co}(E)$ are reference spectra for thin-films with 4.5 nm thickness, corresponding to the estimated diameter of the nanowires. The fit result is shown as red curve in Figure 49. Note that, for better visualization, the blue CoO and orange Co curve in Figure 49 include the green substrate contribution as well.

The spectrum can only be described if a considerable amount of CoO is taken into account because of the broad background originating from oxygen 2s and 2p valence absorption. This gives rise to increased absorption below the M edge, a contribution that is required to describe the peak form accurately and that is absent in the metallic Co absorption spectrum. The best fit is obtained for a composition of (20 ± 7)% Co and (80 ± 9)% CoO (fit parameters $a = 0.07 \pm 0.02, b = 0.28 \pm 0.02$). The fit excludes data below 55 eV, which leads to a slightly better reproduction of the main peak structure. A detailed analysis of the fit suggests that as long as the Co/CoO ratio remains below ≈ 0.8 (45%/55%), the fit result describes the spectrum reasonably well (the variation of the root mean square (rms) error is below 3%). While marked by substantial uncertainties, the fit result confirms that CoO is the dominant species, presumably complemented by a small contribution of metallic Co, in good agreement with conclusions from the TEM and EDXS measurements.

It is also possible to estimate the total surface coverage from the XUV spectra. Fitting the absorption spectrum by a superposition of the absorption spectra of 4.5 nm thick Co and CoO films with the above 1:4 abundance ratio, a surface

coverage of $(35 \pm 4)\%$ is obtained from the sum of the coefficients a and b. This value remains fairly constant for different Co/CoO ratios. To approximate the nanoparticle shapes by cylindrical rods, the value has to be multiplied by $\frac{4}{\pi}$, resulting in an estimated surface coverage between 35 and 45%, slightly larger than the $(23 \pm 6)\%$ obtained from the TEM images. Note that the estimate from the XUV absorption spectra is subject to considerable uncertainties. For instance, the Si_3N_4 substrate may not exhibit a uniform 10 nm thickness as assumed, the exact three-dimensional shape of the particles is not known, and the fit model relies on data for the XUV absorption of thin filters, while nanoparticles may behave differently. Considering the uncertainties accompanying this analysis, the agreement between the surface coverage from the XUV measurements and the TEM analysis is acceptable.

The relatively low signal-to-noise ratio in the XUV absorption spectrum in Figure 49 is a consequence of the employed apparatus, which was designed for gas phase experiments. As a result, the time between the recording of signal and reference images was on the order of several tens of seconds. Thus, fluctuations in the stability of the HHG source, which are much faster, cannot be accounted for, causing the large noise. In future experiments, we expect that the signal can be greatly improved using more stable laser sources and a shorter period between the recording of signal and reference spectra. In particular, the noise caused by instabilities of the HHG source is less critical in a pump-probe setup where fast switching between reference and signal (periods with the pump laser off and on, respectively) is straightforward. The height of the main absorption peak around 62 eV of about 40 mOD will increase with surface coverage. This, however, entails the risk of particle coagulation on the substrate. Considering that recent XUV absorption experiments have shown that a change in the optical density down to 1 mOD can be detected [238], our results suggest that the investigation of photoinduced dynamics in separated nanoparticles is likely possible with HHG based XUV transient absorption spectroscopy. Based on these estimates, photoinduced spectral changes in the investigated nanoparticles would have to be larger than about 3% in order to be detectable in a transient absorption spectroscopy experiment.

6.5 Conclusions

In summary, nanowire-shaped particles are synthesized by agglomeration of Co atoms along the cores of quantum vortices inside superfluid He nanodroplets, followed by deposition and oxidation on ultrathin substrates. A table-top XUV absorption spectrum recorded within minutes demonstrates that an investigation

of deposited nanoparticles with a surface coverage far below a monolayer is possible with an HHG based light source, paving the way for time-resolved pump-probe experiments on these systems. The employed synthesis of nanoparticles in helium nanodroplets provides a solvent- and surfactant-free method to produce clean nanoparticles with the advantage of a very soft deposition process. The latter is crucial for a decoration of ultrathin, XUV transparent substrates that are required for XUV absorption spectroscopy. An analysis of the deposited particles by transmission electron microscopy reveals that the synthesis method based on the deposition of metallic Co particles, which are subsequently exposed to ambient air, results in the formation of cobalt(II) oxide (CoO) nanoparticles. Both methods, transmission electron microscopy and XUV absorption spectroscopy indicate that some particles retain an unoxidized Co core region.

Even though the XUV absorption of the deposited particles is relatively low, our results suggest that standard state-of-the-art XUV transient absorption spectroscopy setups may be used to study photoinduced dynamics in nanoparticles. Therefore, XUV absorption based spectroscopies could provide a formidable approach with unique elemental site-specificity and unprecedented temporal resolution for the study of charge-carrier dynamics [83] that underlie photocatalytic processes in transition metal oxide nanoparticles. This may be particularly interesting for an investigation of plasmon-induced charge carrier dynamics [216,239,240], considering that the helium droplet synthesis approach easily allows for the fabrication of nanoparticles that combine plasmonic materials and transition metal oxides [8,194]. Other applications may address the dynamics in small magnetic systems, such as Co nanoparticles, similar to recent attosecond spectroscopy experiments on Ni containing thin films [241].

6.6 Supplementary Material

6.6.1 Nanoparticle diameter and length

Particle diameters have been determined from the recorded TEM images for particles that are not agglomerated. The obtained histogram is shown in Figure 50, left panel. The length has only been determined for particles that did not show a branched structure. The corresponding histogram is presented in Figure 50, right panel.

Both histograms are created from a set of 100 measured values. The data have been fitted using a normal distribution, the obtained values for the mean μ and the standard deviation σ are given in the Figure. It can be seen that the particle diameter follows a relatively narrow distribution ($\mu = 4.5\,\mathrm{nm}$, $\sigma = 0.7\,\mathrm{nm}$) while

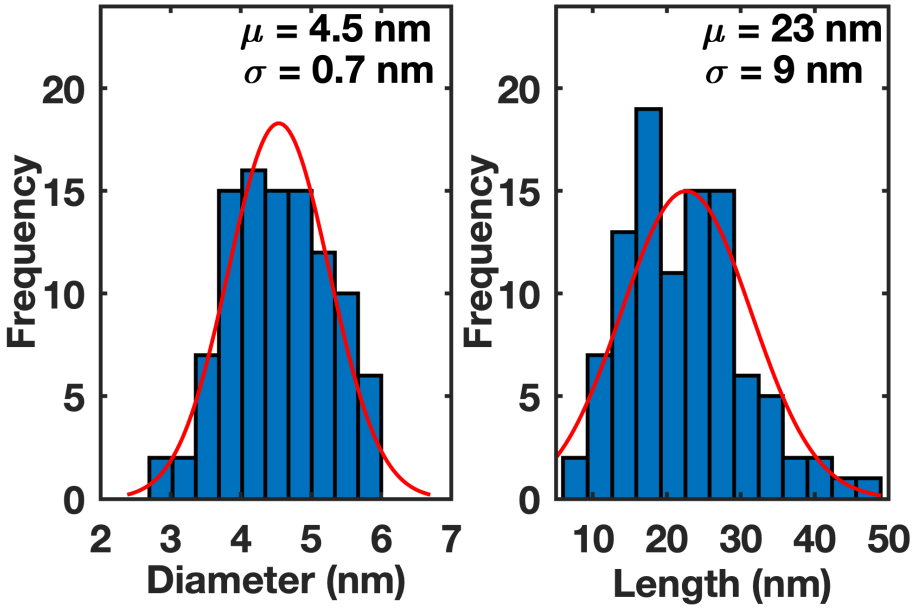

Figure 50: Histograms showing the measured nanoparticle diameters (left panel) and lengths (right panel). The data are fitted with a normal distribution, the obtained mean μ and standard deviation σ are given

the particle lengths are scattered over a large range ($\mu = 23\,\text{nm}$, $\sigma = 9\,\text{nm}$). For the latter case it has to be considered that a bias towards lower values may be introduced because only particles that are not coagulated and branched have been selected. However, 93% of the nanoparticles have a length between 10 and 40 nm, which is the range given in the main manuscript.

6.6.2 Nanoparticle analysis

Table 3 lists major lattice spacings for Co, CoO and Co_3O_4 [242], including the strongest reflections as observed in X-ray diffraction measurements (XRD). The corresponding relative intensities, taken from Ref. 243 for Co and from Ref. [244] for CoO and Co_3O_4, can be found in Figure 53 (b), (c), and (d). Note that for bare Co the parameters for the α-phase (hcp) and β-phase (fcc) are both listed, however, the α-phase is the most stable structure at room-temperature and ambient conditions [234].

In addition to Figure 48 of the main manuscript, Figure 51 and 52 present diffractograms (top images). The corresponding TEM images are shown below. Regions from the recorded TEM images are selected in order to improve the signal to noise ratio. Note that the presented images have not been corrected by using a band-pass filter in order to not obscure diffraction spots that correlate to

Table 3: Major lattice spacings given in nm with corresponding Miller indices for Co, CoO and Co_3O_4 (from Ref. 242, modified)

Co (hexagonal,$P6_3/mmc$)	Co (cubic, $Fm\bar{3}m$)	CoO (cubic, $Fm\bar{3}m$)	Co_3O_4 (cubic, $Fd\bar{3}m$)
0.216 (100)	0.205 (111)	0.246 (111)	0.467 (111)
0.202 (002)	0.177 (200)	0.213 (200)	0.286 (220)
0.191 (101)	0.125 (220)	0.151 (220)	0.243 (311)
0.149 (102)	0.106 (311)	0.128 (311)	0.233 (222)
0.125 (220)	0.102 (222)	0.123 (222)	0.202 (400)

lattice spacings beyond 0.25 nm, which would provide evidence for the presence of Co_3O_4 (see Table 3). The orange circles are drawn to guide the eye for selected lattice spacings and can be compared to the lattice spacings listed in Table 3. Note that the scale in the diffractograms is not exactly the same in each plot as it depends on the magnification used to acquire the TEM images.

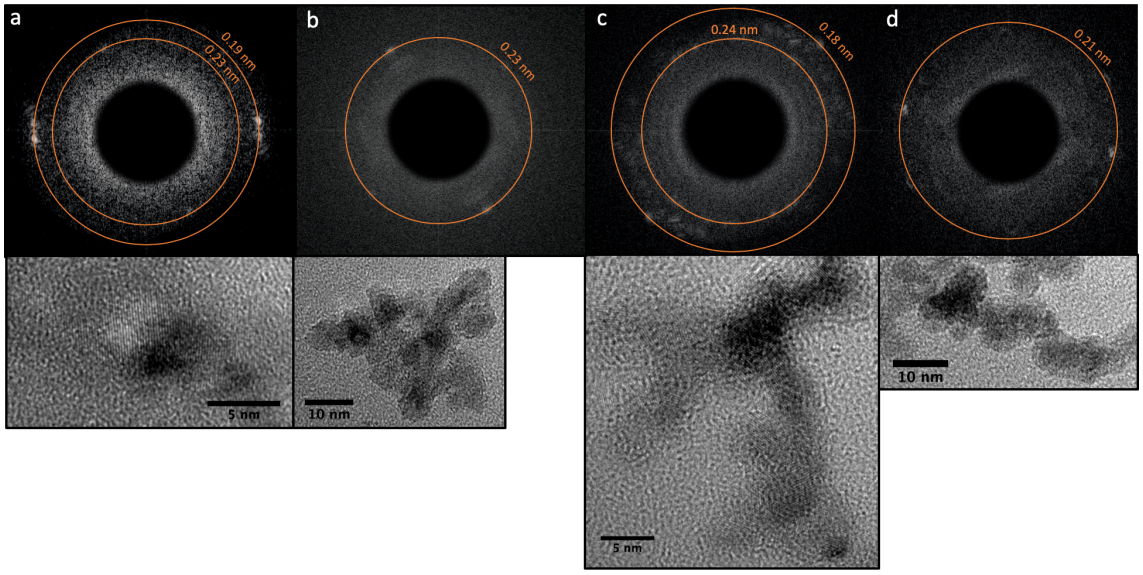

Figure 51: Diffractograms, top images, obtained by 2D Fourier transformation of the corresponding TEM images, shown below. Selected lattice spacings are drawn as orange circles to guide the eye.

The diffraction spots that can be identified in the diffractograms presented in Figure 51 and 52 have been further analyzed in more detail. The position of each reflection is determined using the FIJI software package [199] with an estimated uncertainty of 0.01 nm. The diffraction spots are counted in order to prepare the histogram in Figure 53 (a). Note that this does not reflect the intensities of

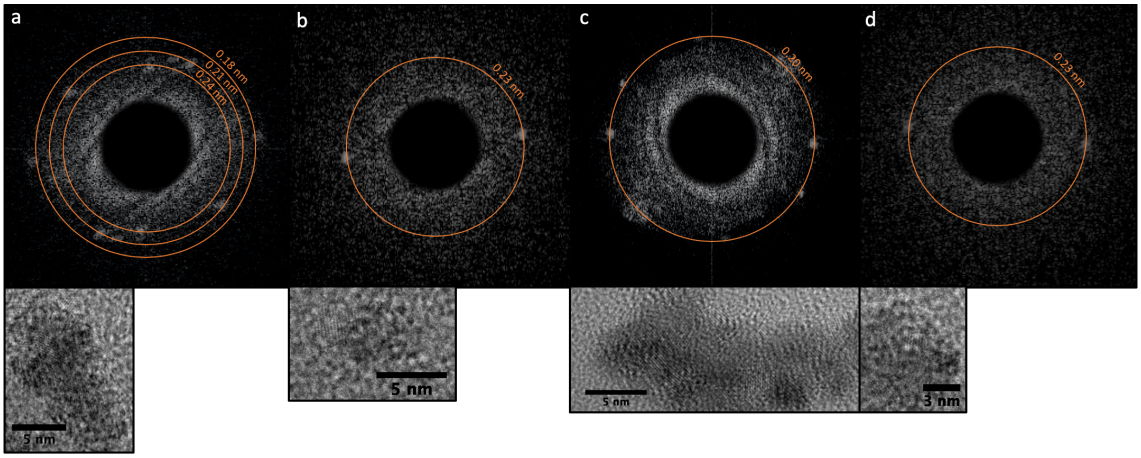

Figure 52: Diffractograms, top images, obtained by 2D Fourier transformation of the corresponding TEM images, shown below. Selected lattice spacings are drawn as orange circles to guide the eye.

the diffraction spots as would be obtained in an XRD measurement. However, the strongest diffraction peaks should also be prominent in the diffractograms. Thus, a comparison of peak positions and intensities from XRD experiments [233, 245, 246] to the histogram, represented by the red line, in Figure 53 (a) is discussed in the following.

In particular, it can be seen that many diffraction spots are observed between 0.23 and 0.24 nm. They can, in principle, be either associated with the CoO (111) or Co_3O_4 (311) reflection at 0.246 nm or 0.243 nm, respectively. Regardless of which oxide, this observation indicates an offset between our values and literature values. Consequently, a 0.01 nm offset is accounted for in panels (b), (c) and (d) by shifting the red line accordingly.

The separation between the most frequent lattice spacings is best reproduced by the (200) and (111) peaks in CoO, as can be seen in panel (c). Furthermore, the Co_3O_4 (220) peak, which served as a fingerprint of Co_3O_4 in previous TEM studies [229], is not observed and neither is the Co_3O_4 (111) lattice (see Table 3 for the latter) [224]. Note that, in contrast to smaller lattice spacings below 0.17 nm, where the resolution of the microscope becomes insufficient and the intensity drops, these peaks could be easily observed in the diffractograms as well as in the real space images. Furthermore, the observation of diffraction spots corresponding to lattice spacings below 0.2 nm can only be explained by the presence of unoxidized Co such as the α-Co (101) reflection.

Based on this discussion, our conclusion, as outlined in the main manuscript, is that the nanoparticles that have been employed for XUV absorption spectroscopy

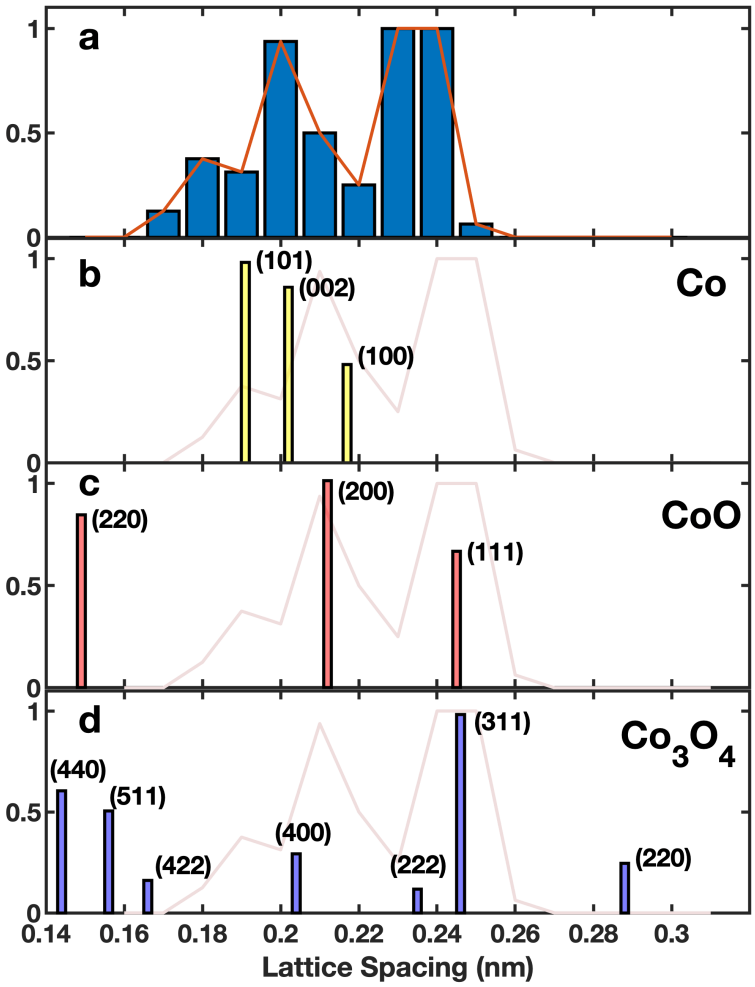

Figure 53: Panel (a) shows a histogram created for the measured diffraction spot positions. The peak intensities for different lattice planes as obtained from XRD measurements [233, 245, 246], are plotted in panels (b) (α-Co), (c) (CoO) and (d) (Co_3O_4). These peaks are compared to the red line in panel (a), offset by $+0.01$ nm.

consist predominantly of CoO, some of which retain regions of unoxidized Co in their interior.

7 Summary

The present thesis describes how nanoparticles, synthesized with the helium droplet approach, are investigated and characterized by a broad range of analytical methods. The emphasis lies on plasmonically active nanoparticles and the role they can potentially play in a more application-oriented strand of research.

In the first presented experiment, Ag@Au core@shell nanorods were produced and their plasmonic properties were investigated by means of electron energy loss spectroscopy (EELS). Though the technique is widely used and well developed, it reaches its detection limits once the tiny volumes of nanoparticles are examined. An ultra-thin hexagonal boron nitride (h-BN) substrate was produced and, for the first time, employed in nanoscale plasmon spectroscopy to overcome those limitations. In a successful study the direct comparison to commercially available substrates shows the advantages for data extraction, especially in the low-loss energy range. With the conducted measurements not only the substrate was tested, but also the plasmonic properties of the nanoparticles were conclusively demonstrated.

Building on this experience, more Ag@Au core@shell species with varying material ratios were tailored by utilizing the versatile adjustability of the subsequent pickup scheme in the helium droplet apparatus. Thereby, a shift of the localized surface plasmon resonance (LSPR) was introduced and measured by means of UV/vis spectroscopy. In a set of experiments, high surface coverage with nanoparticles was achieved on fused silica slides, allowing for the production of substrates for surface enhanced Raman spectroscopy (SERS). A functionalization with 4-MBT molecules and subsequent SERS measurements yielded enhancement factors on the order of $10^3 - 10^4$. The results show, in principle, the possibility for the production of high-density substrates for sensor-related applications with the helium droplet method.

The capability of the approach, regarding the variety of employed metals, was shown with the synthesis of Ag@ZnO core@shell nanoparticles in spherical and wire-like shapes. ZnO is known as a difficult material for a reliable production on the nanoscale. With the formation of core@shell species in varying sizes and shapes and subsequent oxidation, the helium droplet method is well suited to embark the production of new and more complicated material combinations. Electron microscopy images reveal how uniform the thin high-quality ZnO shell covers the Ag cores, independent of their shapes. In the according experiments, the plasmonic activity of the Ag was shown by means of two-photon photoemission (2PPE) spectroscopy. Furthermore, the properties and oxidation state of the

shell were investigated by UV photoelectron spectroscopy (UPS) measurements. The results suggest that the plasmonic active Ag cores are well protected by the evenly distributed ZnO shells and that complex material combinations can be reliably synthesized.

The final presented experiment revolves around a new measurement possibility by employing XUV absorption spectroscopy for the analysis of CoO nanowires. The proof-of-concept study demonstrates that the evaluation of a sub-monolayer of nanoparticles can be reliably conducted. This is the first step towards time resolved pump-probe measurements on comparable samples. With an according setup, time resolution down in the femtosecond regime is possible, paving the way towards the observation of e.g. plasmon induced charge carrier dynamics. Core@shell combinations of plasmonic materials with transition metal oxides, like the successfully synthesized Ag@ZnO nanoparticles, are promising candidates for future experiments.

Overall, the unique properties and advantages of the helium droplet synthesis approach were utilized to tailor a variety of different nanoparticles under controlled circumstances within a pristine environment. The wide range of possible material combinations together with the variability of producible shapes and sizes are unique features of the helium droplet method. Furthermore, a wide range of analytical techniques were employed, some of them for the first time, for the conduction of measurements on nanoparticle samples. In this context, information was not only gained on the properties of the samples, but also on the usability of analysis methods, on their resolution limits and precision. Thereby, important perspectives open up for future research, especially in the field of plasmonics, since the importance of nanoparticles and measurements on the nanoscale will certainly increase in years to come.

8 References

[1] A. Schiffmann, D. Knez, F. Lackner, M. Lasserus, R. Messner, M. Schnedlitz, G. Kothleitner, F. Hofer, and W. E. Ernst, "Ultra-thin h-BN substrates for nanoscale plasmon spectroscopy," *J. Appl. Phys.*, vol. 125, p. 023104, Jan. 2019.

[2] F. Lackner, A. Schiffmann, M. Lasserus, R. Messner, M. Schnedlitz, H. Fitzek, P. Pölt, D. Knez, G. Kothleitner, and W. E. Ernst, "Helium nanodroplet assisted synthesis of bimetallic Ag@Au nanoparticles with tunable localized surface plasmon resonance," *Eur. Phys. J. D*, vol. 73, p. 104, May 2019.

[3] A. Schiffmann, T. Jauk, D. Knez, H. Fitzek, F. Hofer, F. Lackner, and W. E. Ernst, "Helium droplet assisted synthesis of plasmonic Ag@ZnO core@shell nanoparticles," *Nano Res.*, vol. 13, pp. 2979–2986, Nov. 2020.

[4] A. Schiffmann, B. W. Toulson, D. Knez, R. Messner, M. Schnedlitz, M. Lasserus, F. Hofer, W. E. Ernst, O. Gessner, and F. Lackner, "Ultrashort XUV pulse absorption spectroscopy of partially oxidized cobalt nanoparticles," *J. Appl. Phys.*, vol. 127, p. 184303, May 2020.

[5] D. Knez, M. Schnedlitz, M. Lasserus, A. Schiffmann, W. E. Ernst, and F. Hofer, "Modelling electron beam induced dynamics in metallic nanoclusters," *Ultramicroscopy*, vol. 192, pp. 69–79, Sept. 2018.

[6] M. Lasserus, M. Schnedlitz, D. Knez, R. Messner, A. Schiffmann, F. Lackner, A. W. Hauser, F. Hofer, and W. E. Ernst, "Thermally induced alloying processes in a bimetallic system at the nanoscale: AgAu sub-5 nm core–shell particles studied at atomic resolution," *Nanoscale*, vol. 10, pp. 2017–2024, Jan. 2018.

[7] R. Messner, A. Schiffmann, J. V. Pototschnig, M. Lasserus, M. Schnedlitz, F. Lackner, and W. E. Ernst, "Spectroscopy of gold atoms and gold oligomers in helium nanodroplets," *J. Chem. Phys.*, vol. 149, p. 024305, July 2018.

[8] M. Schnedlitz, R. Fernandez-Perea, D. Knez, M. Lasserus, A. Schiffmann, F. Hofer, A. W. Hauser, M. P. de Lara-Castells, and W. E. Ernst, "Effects of the Core Location on the Structural Stability of Ni–Au Core–Shell Nanoparticles," *J. Phys. Chem. C*, vol. 123, pp. 20037–20043, Aug. 2019.

[9] A. Volk, *Nanocluster and Nanowire Growth in Superfluid Helium Droplets*. PhD Thesis, Graz University of Technology, Jan. 2016.

[10] P. Thaler, *Buildup and Characterization of an Apparatus for the Synthesis of Metallic Nanoparticles Inside Helium Droplets*. PhD Thesis, Graz University of Technology, Sept. 2015.

[11] J. Steurer, *Helium Droplet Mediated Fabrication and Analysis of Noble Metal Nanoparticles*. Master's Thesis, Graz University of Technology, Apr. 2014.

[12] L. L. Lohr and S. M. Blinder, "The Weakest Link: Bonding between Helium Atoms," *J. Chem. Educ.*, vol. 84, p. 860, May 2007.

[13] R. J. Donnelly and C. F. Barenghi, "The Observed Properties of Liquid Helium at the Saturated Vapor Pressure," *J. Phys. Chem. Ref. Data*, vol. 27, pp. 1217–1274, Nov. 1998.

[14] P. Kapitza, "Viscosity of Liquid Helium below the λ-Point," *Nature*, vol. 141, pp. 74–74, Jan. 1938.

[15] J. F. Allen and A. D. Misener, "Flow of Liquid Helium II," *Nature*, vol. 141, pp. 75–75, Jan. 1938.

[16] E. W. Becker, R. Klingelhöfer, and P. Lohse, "Notizen: Strahlen aus kondensiertem Helium im Hochvakuum," *Z. Naturforsch.*, vol. 16, pp. 1259–1259, Nov. 1961.

[17] C. Callegari and W. E. Ernst, "Helium Droplets as Nanocryostats for Molecular Spectroscopy—from the Vacuum Ultraviolet to the Microwave Regime," in *Handbook of High-Resolution Spectroscopy*, John Wiley & Sons, Inc., 2011.

[18] J. P. Toennies and A. F. Vilesov, "Superfluid Helium Droplets: A Uniquely Cold Nanomatrix for Molecules and Molecular Complexes," *Angew. Chem. Int. Ed.*, vol. 43, no. 20, pp. 2622–2648, 2004.

[19] M. Hartmann, R. E. Miller, J. P. Toennies, and A. Vilesov, "Rotationally Resolved Spectroscopy of SF6 in Liquid Helium Clusters: A Molecular Probe of Cluster Temperature," *Phys. Rev. Lett.*, vol. 75, pp. 1566–1569, Aug. 1995.

[20] G. Auböck, J. Nagl, C. Callegari, and W. E. Ernst, "Triplet State Excitation of Alkali Molecules on Helium Droplets: Experiments and Theory," *J. Phys. Chem. A*, vol. 111, pp. 7404–7410, Aug. 2007.

[21] S. Grebenev, J. P. Toennies, and A. F. Vilesov, "Superfluidity Within a Small Helium-4 Cluster: The Microscopic Andronikashvili Experiment," *Science*, vol. 279, pp. 2083–2086, Mar. 1998.

[22] R. J. Donnelly, *Quantized Vortices in Helium II*. Cambridge University Press, Mar. 1991.

[23] Y. A. Sergeev and C. F. Barenghi, "Particles-Vortex Interactions and Flow Visualization in 4He," *J. Low Temp. Phys.*, vol. 157, p. 429, Oct. 2009.

[24] J. Tiggesbäumker and F. Stienkemeier, "Formation and properties of metal clusters isolated in helium droplets," *Phys. Chem. Chem. Phys.*, vol. 9, pp. 4748–4770, Aug. 2007.

[25] S. Yang, A. M. Ellis, D. Spence, C. Feng, A. Boatwright, E. Latimer, and C. Binns, "Growing metal nanoparticles in superfluid helium," *Nanoscale*, vol. 5, no. 23, pp. 11545–11553, 2013.

[26] A. W. Hauser, A. Volk, P. Thaler, and W. E. Ernst, "Atomic collisions in suprafluid helium-nanodroplets: Timescales for metal-cluster formation derived from He-density functional theory," *Phys. Chem. Chem. Phys.*, vol. 17, no. 16, pp. 10805–10812, 2015.

[27] A. Volk, P. Thaler, D. Knez, A. W. Hauser, J. Steurer, W. Grogger, F. Hofer, and W. E. Ernst, "The impact of doping rates on the morphologies of silver and gold nanowires grown in helium nanodroplets," *Phys. Chem. Chem. Phys.*, vol. 18, pp. 1451–1459, Jan. 2016.

[28] V. Mozhayskiy, M. N. Slipchenko, V. K. Adamchuk, and A. F. Vilesov, "Use of helium nanodroplets for assembly, transport, and surface deposition of large molecular and atomic clusters," *J. Chem. Phys.*, vol. 127, p. 094701, Sept. 2007.

[29] E. Gordon, A. Karabulin, V. Matyushenko, V. Sizov, and I. Khodos, "Stability and structure of nanowires grown from silver, copper and their alloys by laser ablation into superfluid helium," *Phys. Chem. Chem. Phys.*, vol. 16, pp. 25229–25233, Nov. 2014.

[30] M. Schnedlitz, M. Lasserus, D. Knez, A. W. Hauser, F. Hofer, and W. E. Ernst, "Thermally induced breakup of metallic nanowires: Experiment and theory," *Phys. Chem. Chem. Phys.*, vol. 19, no. 14, pp. 9402–9408, 2017.

[31] L. F. Gomez, E. Loginov, and A. F. Vilesov, "Traces of Vortices in Superfluid Helium Droplets," *Phys. Rev. Lett.*, vol. 108, p. 155302, Apr. 2012.

[32] G. Sauerbrey, "Verwendung von Schwingquarzen zur Wägung dünner Schichten und zur Mikrowägung," *Z. Physik*, vol. 155, pp. 206–222, Apr. 1959.

[33] P. Thaler, A. Volk, M. Ratschek, M. Koch, and W. E. Ernst, "Molecular dynamics simulation of the deposition process of cold Ag-clusters under different landing conditions," *J. Chem. Phys.*, vol. 140, p. 044326, Jan. 2014.

[34] V. N. Popok, I. Barke, E. E. B. Campbell, and K.-H. Meiwes-Broer, "Cluster–surface interaction: From soft landing to implantation," *Surf. Sci. Rep.*, vol. 66, pp. 347–377, Oct. 2011.

[35] E. Loginov, L. F. Gomez, and A. F. Vilesov, "Surface Deposition and Imaging of Large Ag Clusters Formed in He Droplets," *J. Phys. Chem. A*, vol. 115, pp. 7199–7204, June 2011.

[36] W. Demtröder, *Experimentalphysik 4 - Kern-, Teilchen- Und Astrophysik*. Springer-Verlag GmbH Deutschland, fifth ed., 2017.

[37] D. McMullan, "Scanning electron microscopy 1928–1965," *Scanning*, vol. 17, no. 3, pp. 175–185, 1995.

[38] W. Demtröder, *Experimentalphysik 3 - Atome, Moleküle Und Festkörper*. Springer-Verlag GmbH Deutschland, fifth ed., 2016.

[39] J. I. Goldstein, D. E. Newbury, J. R. Michael, N. W. Ritchie, J. H. J. Scott, and D. C. Joy, *Scanning Electron Microscopy and X-Ray Microanalysis*. Springer Science+Business Media LLC, fourth ed., 2018.

[40] T. E. Everhart and R. F. M. Thornley, "Wide-band detector for micro-microampere low-energy electron currents," *J. Sci. Instrum.*, vol. 37, pp. 246–248, July 1960.

[41] A. V. Crewe, J. Wall, and J. Langmore, "Visibility of Single Atoms," *Science*, vol. 168, pp. 1338–1340, June 1970.

[42] H. H. Rose, "Optics of high-performance electron microscopes," *Sci. Technol. Adv. Mater.*, vol. 9, p. 014107, Apr. 2008.

[43] N. Dellby, L. Krivanek, D. Nellist, E. Batson, and R. Lupini, "Progress in aberration-corrected scanning transmission electron microscopy," *J. Electron Microsc.*, vol. 50, pp. 177–185, May 2001.

[44] C. Kisielowski, B. Freitag, M. Bischoff, H. van Lin, S. Lazar, G. Knippels, P. Tiemeijer, M. van der Stam, S. von Harrach, M. Stekelenburg, M. Haider, S. Uhlemann, H. Müller, P. Hartel, B. Kabius, D. Miller, I. Petrov, E. A. Olson, T. Donchev, E. A. Kenik, A. R. Lupini, J. Bentley, S. J. Pennycook, I. M. Anderson, A. M. Minor, A. K. Schmid, T. Duden, V. Radmilovic, Q. M.

Ramasse, M. Watanabe, R. Erni, E. A. Stach, P. Denes, and U. Dahmen, "Detection of Single Atoms and Buried Defects in Three Dimensions by Aberration-Corrected Electron Microscope with 0.5-Å Information Limit," *Microsc. Microanal.*, vol. 14, pp. 469–477, Oct. 2008.

[45] S. J. Pennycook, "The impact of STEM aberration correction on materials science," *Ultramicroscopy*, vol. 180, pp. 22–33, Sept. 2017.

[46] M. T. Otten, "High-Angle annular dark-field imaging on a tem/stem system," *J. Electron Microsc. Tech.*, vol. 17, no. 2, pp. 221–230, 1991.

[47] P. D. Nellist and S. J. Pennycook, "The principles and interpretation of annular dark-field Z-contrast imaging," in *Advances in Imaging and Electron Physics* (P. W. Hawkes, ed.), vol. 113, pp. 147–203, Elsevier, Jan. 2000.

[48] A. Muller and J. Grazul, "Optimizing the environment for sub-0.2 nm scanning transmission electron microscopy," *J. Electron Microsc.*, vol. 50, pp. 219–226, May 2001.

[49] G. Haberfehlner, P. Thaler, D. Knez, A. Volk, F. Hofer, W. E. Ernst, and G. Kothleitner, "Formation of bimetallic clusters in superfluid helium nanodroplets analysed by atomic resolution electron tomography," *Nat. Commun.*, vol. 6, p. 8779, Oct. 2015.

[50] M. Schnedlitz, M. Lasserus, R. Meyer, D. Knez, F. Hofer, W. E. Ernst, and A. W. Hauser, "Stability of Core–Shell Nanoparticles for Catalysis at Elevated Temperatures: Structural Inversion in the Ni–Au System Observed at Atomic Resolution," *Chem. Mater.*, vol. 30, pp. 1113–1120, Feb. 2018.

[51] G. Gauglitz and D. S. Moore, *Handbook of Spectroscopy*. Wiley-VCH Verlag & Co. KGaA, second ed., 2014.

[52] P. Lechner, S. Eckbauer, R. Hartmann, S. Krisch, D. Hauff, R. Richter, H. Soltau, L. Strüder, C. Fiorini, E. Gatti, A. Longoni, and M. Sampietro, "Silicon drift detectors for high resolution room temperature X-ray spectroscopy," *Nuclear Instruments and Methods in Physics Research Section A: Accelerators, Spectrometers, Detectors and Associated Equipment*, vol. 377, pp. 346–351, Aug. 1996.

[53] J. Hillier and R. F. Baker, "Microanalysis by Means of Electrons," *J. Appl. Phys.*, vol. 15, pp. 663–675, Sept. 1944.

[54] R. F. Egerton, "Electron energy-loss spectroscopy in the TEM," *Rep. Prog. Phys.*, vol. 72, no. 1, p. 016502, 2009.

[55] Q. M. Ramasse, C. R. Seabourne, D.-M. Kepaptsoglou, R. Zan, U. Bangert, and A. J. Scott, "Probing the Bonding and Electronic Structure of Single Atom Dopants in Graphene with Electron Energy Loss Spectroscopy," *Nano Lett.*, vol. 13, pp. 4989–4995, Oct. 2013.

[56] R. Gross and A. Marx, *Festkörperphysik*. Oldenbourg Wissenschaftsverlag GmbH, 2012.

[57] V. Amendola, R. Pilot, M. Frasconi, O. M. Maragò, and M. A. Iatì, "Surface plasmon resonance in gold nanoparticles: A review," *J. Phys.: Condens. Matter*, vol. 29, p. 203002, Apr. 2017.

[58] L. C. Oliveira, A. M. Nogueira Lima, C. Thirstrup, and H. F. Neff, *Surface Plasmon Resonance Sensors - A Materials Guide to Design and Optimization*. Springer International Publishing, 2015.

[59] L. Novotny and B. Hecht, *Principles of Nano-Optics*. Cambridge University Press, second ed., 2012.

[60] S. A. Maier, *Plasmonics - Fundamentals and Applications*. Springer Science+Business Media LLC, first ed., 2007.

[61] T. Jauk, *Energy-Filtered Photoemission Electron Microscopy of Surfaces, Nanoparticles and Nanostructures*. Master's Thesis, Graz University of Technology, Graz, Nov. 2019.

[62] E. Kretschmann and H. Raether, "Notizen: Radiative Decay of Non Radiative Surface Plasmons Excited by Light," *Z. Naturforsch. A*, vol. 23, pp. 2135–2136, Dec. 1968.

[63] E. Petryayeva and U. J. Krull, "Localized surface plasmon resonance: Nanostructures, bioassays and biosensing—A review," *Anal. Chim. Acta*, vol. 706, pp. 8–24, Nov. 2011.

[64] C. V. Raman, "A new radiation," *Indian J. Phys.*, vol. 2, pp. 387–398, 1928.

[65] A. Smekal, "Zur Quantentheorie der Dispersion," *Naturwissenschaften*, vol. 11, pp. 873–875, Oct. 1923.

[66] F. Lackner, "Research Laboratory Quantum Optics and Molecular Physics: Raman Spectroscopy - Laser Physics," 2019.

[67] W. Demtröder, *Laser Spectroscopy 2 - Experimental Techniques*. Springer-Verlag Berlin Heidelberg, fifth ed., 2015.

[68] K. Kneipp, M. Moskovits, and H. Kneipp, *Surface-Enhanced Raman Scattering: Physics and Applications*. Springer-Verlag Berlin Heidelberg, 2006.

[69] Shimadzu Corporation, "Instruction Manual: System User's guide UV-1800 Shimadzu Spectrophotometer," Feb. 2008.

[70] M. C. Patt, *Bulk and Surface Sensitive Energy-Filtered Photoemission Microscopy Using Synchrotron Radiation for the Study of Resistive Switching Memories*. No. Band 122 in Schriften Des Forschungszentrums Jülich Reihe Schlüsseltechnologien, Jülich: Forschungszentrum Jülich, 2016.

[71] M. P. Seah and W. A. Dench, "Quantitative electron spectroscopy of surfaces: A standard data base for electron inelastic mean free paths in solids," *Surf. Interface Anal.*, vol. 1, no. 1, pp. 2–11, 1979.

[72] M. Escher, N. Weber, M. Merkel, C. Ziethen, P. Bernhard, G. Schönhense, S. Schmidt, F. Forster, F. Reinert, B. Krömker, and D. Funnemann, "Nanoelectron spectroscopy for chemical analysis: A novel energy filter for imaging x-ray photoemission spectroscopy," *J. Phys.: Condens. Matter*, vol. 17, pp. S1329–S1338, Apr. 2005.

[73] Focus GmbH and Omicron Nano Technology, "NanoESCA Technical Reference Manual: Instrument," Nov. 2014.

[74] Focus GmbH, "Instruction Manual FOCUS PEEM," Nov. 2015.

[75] Focus GmbH, "VUV Source HIS 13 / HIS 14 HD and HIS Mono - Instruction Manual," Jan. 2018.

[76] O. Renault, R. Brochier, A. Roule, P.-H. Haumesser, B. Krömker, and D. Funnemann, "Work-function imaging of oriented copper grains by photoemission," *Surf. Interface Anal.*, vol. 38, no. 4, pp. 375–377, 2006.

[77] H. Ueba and B. Gumhalter, "Theory of two-photon photoemission spectroscopy of surfaces," *Prog. Surf. Sci.*, vol. 82, pp. 193–223, Jan. 2007.

[78] T. Mii and H. Ueba, "Theory of time-resolved two-photon photoemission spectroscopy from metal surfaces," *J. Lumin.*, vol. 87-89, pp. 898–901, May 2000.

[79] D. Bayer, C. Wiemann, O. Gaier, M. Bauer, and M. Aeschlimann, "Time-Resolved 2PPE and Time-Resolved PEEM as a Probe of LSP's in Silver Nanoparticles," *J. Nanomater.*, vol. 2008, p. e249514, Sept. 2008.

[80] A. Volk, D. Knez, P. Thaler, A. W. Hauser, W. Grogger, F. Hofer, and W. E. Ernst, "Thermal instabilities and Rayleigh breakup of ultrathin silver nanowires grown in helium nanodroplets," *Phys. Chem. Chem. Phys.*, vol. 17, no. 38, pp. 24570–24575, 2015.

[81] I. V. Hertel and C.-P. Schulz, *Atoms, Molecules and Optical Physics 1 - Atoms and Spectroscopy*. Springer-Verlag Berlin Heidelberg, 2015.

[82] M. F. Jager, *Attosecond Transient Absorption of Solid-State and Phase-Change Materials*. PhD Thesis, University of Berkeley, California, 2017.

[83] R. Geneaux, H. J. B. Marroux, A. Guggenmos, D. M. Neumark, and S. R. Leone, "Transient absorption spectroscopy using high harmonic generation: A review of ultrafast X-ray dynamics in molecules and solids," *Philosophical Transactions of the Royal Society A: Mathematical, Physical and Engineering Sciences*, vol. 377, p. 20170463, May 2019.

[84] P. B. Corkum, "Plasma perspective on strong field multiphoton ionization," *Phys. Rev. Lett.*, vol. 71, pp. 1994–1997, Sept. 1993.

[85] M.-F. Lin, A. N. Pfeiffer, D. M. Neumark, S. R. Leone, and O. Gessner, "Strong-field induced XUV transmission and multiplet splitting in 4d-16p core-excited Xe studied by femtosecond XUV transient absorption spectroscopy," *J. Chem. Phys.*, vol. 137, p. 244305, Dec. 2012.

[86] B. W. Toulson, M. Borgwardt, H. Wang, F. Lackner, A. S. Chatterley, C. D. Pemmaraju, D. M. Neumark, S. R. Leone, D. Prendergast, and O. Gessner, "Probing ultrafast C–Br bond fission in the UV photochemistry of bromoform with core-to-valence transient absorption spectroscopy," *Struct. Dyn.*, vol. 6, p. 054304, Sept. 2019.

[87] A. S. Chatterley, F. Lackner, D. M. Neumark, S. R. Leone, and O. Gessner, "Tracking dissociation dynamics of strong-field ionized 1,2-dibromoethane with femtosecond XUV transient absorption spectroscopy," *Phys. Chem. Chem. Phys.*, vol. 18, pp. 14644–14653, May 2016.

[88] F. Lackner, A. S. Chatterley, C. D. Pemmaraju, K. D. Closser, D. Prendergast, D. M. Neumark, S. R. Leone, and O. Gessner, "Direct observation of ring-opening dynamics in strong-field ionized selenophene using femtosecond inner-shell absorption spectroscopy," *J. Chem. Phys.*, vol. 145, p. 234313, Dec. 2016.

[89] A. S. Chatterley, F. Lackner, C. D. Pemmaraju, D. M. Neumark, S. R. Leone, and O. Gessner, "Dissociation Dynamics and Electronic Structures of Highly Excited Ferrocenium Ions Studied by Femtosecond XUV Absorption Spectroscopy," *J. Phys. Chem. A*, vol. 120, pp. 9509–9518, Dec. 2016.

[90] R. C. Jaklevic, J. Lambe, A. H. Silver, and J. E. Mercereau, "Quantum Interference Effects in Josephson Tunneling," *Phys. Rev. Lett.*, vol. 12, pp. 159–160, Feb. 1964.

[91] B. D. Josephson, "Possible new effects in superconductive tunnelling," *Phys. Lett.*, vol. 1, pp. 251–253, July 1962.

[92] P. W. Anderson and J. M. Rowell, "Probable Observation of the Josephson Superconducting Tunneling Effect," *Phys. Rev. Lett.*, vol. 10, pp. 230–232, Mar. 1963.

[93] L. N. Cooper, "Bound Electron Pairs in a Degenerate Fermi Gas," *Phys. Rev.*, vol. 104, pp. 1189–1190, Nov. 1956.

[94] O. Dössel, *Bildgebende Verfahren in Der Medizin - Von Der Technik Zur Medizinischen Anwendung*. Springer-Verlag Berlin Heidelberg, second ed., 2016.

[95] S. Topolovec, H. Krenn, and R. Würschum, "Enhanced magnetic moment of ultrathin Co films measured by in situ electrodeposition in a SQUID," *J. Magn. Magn. Mater.*, vol. 397, pp. 96–100, Jan. 2016.

[96] F. Shahzad, K. Nadeem, J. Weber, H. Krenn, and P. Knoll, "Magnetic behavior of NiO nanoparticles determined by SQUID magnetometry," *Mater. Res. Express*, vol. 4, p. 086102, Aug. 2017.

[97] M. Schnedlitz, D. Knez, M. Lasserus, F. Hofer, R. Fernández-Perea, A. W. Hauser, M. Pilar de Lara-Castells, and W. E. Ernst, "Thermally Induced Diffusion and Restructuring of Iron Triade (Fe, Co, Ni) Nanoparticles Passivated by Several Layers of Gold," *J. Phys. Chem. C*, vol. 124, pp. 16680–16688, July 2020.

[98] T. T. Tran, K. Bray, M. J. Ford, M. Toth, and I. Aharonovich, "Quantum emission from hexagonal boron nitride monolayers," *Nat. Nanotechnol.*, vol. 11, pp. 37–41, Jan. 2016.

[99] H. Liu, J. H. Meng, X. W. Zhang, Y.-N. Chen, Z. G. Yin, D. Wang, Y. Wang, J. You, M. Gao, and P. Jin, "High-performance deep ultraviolet photodetectors based on few-layer hexagonal boron nitride," *Nanoscale*, Feb. 2018.

[100] W. Zhu, Z. Wu, G. S. Foo, X. Gao, M. Zhou, B. Liu, G. M. Veith, P. Wu, K. L. Browning, H. N. Lee, H. Li, S. Dai, and H. Zhu, "Taming interfacial electronic properties of platinum nanoparticles on vacancy-abundant boron nitride nanosheets for enhanced catalysis," *Nat. Commun.*, vol. 8, p. 15291, June 2017.

[101] S. Torii, K. Jimura, S. Hayashi, R. Kikuchi, and A. Takagaki, "Utilization of hexagonal boron nitride as a solid acid–base bifunctional catalyst," *J. Catal.*, vol. 355, pp. 176–184, Nov. 2017.

[102] J. Zhu, J. Kang, J. Kang, D. Jariwala, J. D. Wood, J.-W. T. Seo, K.-S. Chen, T. J. Marks, and M. C. Hersam, "Solution-Processed Dielectrics Based on Thickness-Sorted Two-Dimensional Hexagonal Boron Nitride Nanosheets," *Nano Lett.*, vol. 15, pp. 7029–7036, Oct. 2015.

[103] L. Britnell, R. V. Gorbachev, R. Jalil, B. D. Belle, F. Schedin, M. I. Katsnelson, L. Eaves, S. V. Morozov, A. S. Mayorov, N. M. R. Peres, A. H. Castro Neto, J. Leist, A. K. Geim, L. A. Ponomarenko, and K. S. Novoselov, "Electron Tunneling through Ultrathin Boron Nitride Crystalline Barriers," *Nano Lett.*, vol. 12, pp. 1707–1710, Mar. 2012.

[104] L. Wang, I. Meric, P. Y. Huang, Q. Gao, Y. Gao, H. Tran, T. Taniguchi, K. Watanabe, L. M. Campos, D. A. Muller, J. Guo, P. Kim, J. Hone, K. L. Shepard, and C. R. Dean, "One-Dimensional Electrical Contact to a Two-Dimensional Material," *Science*, vol. 342, pp. 614–617, Nov. 2013.

[105] K. K. Kim, A. Hsu, X. Jia, S. M. Kim, Y. Shi, M. Hofmann, D. Nezich, J. F. Rodriguez-Nieva, M. Dresselhaus, T. Palacios, and J. Kong, "Synthesis of Monolayer Hexagonal Boron Nitride on Cu Foil Using Chemical Vapor Deposition," *Nano Lett.*, vol. 12, pp. 161–166, Jan. 2012.

[106] Y. Wu, G. Li, and J. P. Camden, "Probing Nanoparticle Plasmons with Electron Energy Loss Spectroscopy," *Chem. Rev.*, vol. 118, pp. 2994–3031, Mar. 2018.

[107] G. Haberfehlner, F.-P. Schmidt, G. Schaffernak, A. Hörl, A. Trügler, A. Hohenau, F. Hofer, J. R. Krenn, U. Hohenester, and G. Kothleitner, "3D Imaging of Gap Plasmons in Vertically Coupled Nanoparticles by EELS Tomography," *Nano Lett.*, Oct. 2017.

[108] G. Haberfehlner, A. Trügler, F. P. Schmidt, A. Hörl, F. Hofer, U. Hohenester, and G. Kothleitner, "Correlated 3D Nanoscale Mapping and Simulation

of Coupled Plasmonic Nanoparticles," *Nano Lett.*, vol. 15, no. 11, pp. 7726–7730, 2015.

[109] F.-P. Schmidt, H. Ditlbacher, U. Hohenester, A. Hohenau, F. Hofer, and J. R. Krenn, "Dark Plasmonic Breathing Modes in Silver Nanodisks," *Nano Lett.*, vol. 12, no. 11, pp. 5780–5783, 2012.

[110] O. Nicoletti, F. de la Peña, R. K. Leary, D. J. Holland, C. Ducati, and P. A. Midgley, "Three-dimensional imaging of localized surface plasmon resonances of metal nanoparticles," *Nature*, vol. 502, no. 7469, pp. 80–84, 2013.

[111] A. L. Koh, A. I. Fernández-Domínguez, D. W. McComb, S. A. Maier, and J. K. W. Yang, "High-Resolution Mapping of Electron-Beam-Excited Plasmon Modes in Lithographically Defined Gold Nanostructures," *Nano Lett.*, vol. 11, no. 3, pp. 1323–1330, 2011.

[112] M. K. Krug, G. Schaffernak, M. Belitsch, M. Gašparić, V. Leitgeb, A. Trügler, U. Hohenester, J. R. Krenn, and A. Hohenau, "Mapping the local particle plasmon sensitivity with a scanning probe," *Nanoscale*, vol. 8, no. 36, pp. 16449–16454, 2016.

[113] M. Rycenga, C. M. Cobley, J. Zeng, W. Li, C. H. Moran, Q. Zhang, D. Qin, and Y. Xia, "Controlling the Synthesis and Assembly of Silver Nanostructures for Plasmonic Applications," *Chem. Rev.*, vol. 111, pp. 3669–3712, June 2011.

[114] S. A. Maier and H. A. Atwater, "Plasmonics: Localization and guiding of electromagnetic energy in metal/dielectric structures," *J. Appl. Phys.*, vol. 98, p. 011101, July 2005.

[115] K. Kneipp, "Surface-enhanced Raman scattering," *Phys. Today*, vol. 60, pp. 40–46, Nov. 2007.

[116] A. Naldoni, V. M. Shalaev, and M. L. Brongersma, "Applying plasmonics to a sustainable future," *Science*, vol. 356, pp. 908–909, June 2017.

[117] J. A. Jackman, A. R. Ferhan, and N.-J. Cho, "Nanoplasmonic sensors for biointerfacial science," *Chem. Soc. Rev.*, vol. 46, pp. 3615–3660, June 2017.

[118] X. Ren, E. Cao, W. Lin, Y. Song, W. Liang, and J. Wang, "Recent advances in surface plasmon-driven catalytic reactions," *RSC Adv.*, vol. 7, pp. 31189–31203, June 2017.

[119] G. Cassabois, P. Valvin, and B. Gil, "Hexagonal boron nitride is an indirect bandgap semiconductor," *Nat. Photonics*, vol. 10, pp. 262–266, Apr. 2016.

[120] P. Thaler, A. Volk, F. Lackner, J. Steurer, D. Knez, W. Grogger, F. Hofer, and W. E. Ernst, "Formation of bimetallic core-shell nanowires along vortices in superfluid He nanodroplets," *Phys. Rev. B*, vol. 90, p. 155442, Oct. 2014.

[121] E. Latimer, D. Spence, C. Feng, A. Boatwright, A. M. Ellis, and S. Yang, "Preparation of Ultrathin Nanowires Using Superfluid Helium Droplets," *Nano Lett.*, vol. 14, pp. 2902–2906, May 2014.

[122] K. K. Kim, A. Hsu, X. Jia, S. M. Kim, Y. Shi, M. Dresselhaus, T. Palacios, and J. Kong, "Synthesis and Characterization of Hexagonal Boron Nitride Film as a Dielectric Layer for Graphene Devices," *ACS Nano*, vol. 6, pp. 8583–8590, Oct. 2012.

[123] A. Boatwright, C. Feng, D. Spence, E. Latimer, C. Binns, A. M. Ellis, and S. Yang, "Helium droplets: A new route to nanoparticles," *Faraday Discuss.*, vol. 162, no. 0, pp. 113–124, 2013.

[124] P. Thaler, A. Volk, D. Knez, F. Lackner, G. Haberfehlner, J. Steurer, M. Schnedlitz, and W. E. Ernst, "Synthesis of nanoparticles in helium droplets—A characterization comparing mass-spectra and electron microscopy data," *J. Chem. Phys.*, vol. 143, p. 134201, Oct. 2015.

[125] L. F. Gomez, E. Loginov, R. Sliter, and A. F. Vilesov, "Sizes of large He droplets," *J. Chem. Phys.*, vol. 135, p. 154201, Oct. 2011.

[126] F. de la Peña, T. Ostasevicius, V. T. Fauske, P. Burdet, P. Jokubauskas, M. Nord, E. Prestat, M. Sarahan, K. E. MacArthur, D. N. Johnstone, J. Taillon, J. Caron, T. Furnival, A. Eljarrat, S. Mazzucco, V. Migunov, T. Aarholt, M. Walls, F. Winkler, B. Martineau, G. Donval, E. R. Hoglund, I. Alxneit, I. Hjorth, L. F. Zagonel, A. Garmannslund, C. Gohlke, I. Iyengar, and H.-W. Chang, "HyperSpy 1.3," *Zenodo*, May 2017.

[127] A. Savitzky and M. J. E. Golay, "Smoothing and Differentiation of Data by Simplified Least Squares Procedures.," *Anal. Chem.*, vol. 36, pp. 1627–1639, July 1964.

[128] N. L. McDougall, R. J. Nicholls, J. G. Partridge, and D. G. McCulloch, "The Near Edge Structure of Hexagonal Boron Nitride," *Micros. Microanal.*, vol. 20, pp. 1053–1059, Aug. 2014.

[129] J. M. Sanz, D. Ortiz, R. Alcaraz de la Osa, J. M. Saiz, F. González, A. S. Brown, M. Losurdo, H. O. Everitt, and F. Moreno, "UV Plasmonic Behavior of Various Metal Nanoparticles in the Near- and Far-Field Regimes: Geometry and Substrate Effects," *J. Phys. Chem. C*, vol. 117, pp. 19606–19615, Sept. 2013.

[130] M. Terauchi, "Electronic structure analyses of BN network materials using high energy-resolution spectroscopy methods based on transmission electron microscopy," *Mircrosc. Res. Tech.*, vol. 69, no. 7, pp. 531–537, 2006.

[131] M. M. Guraya, H. Ascolani, G. Zampieri, J. I. Cisneros, J. H. Dias da Silva, and M. P. Cantão, "Bond densities and electronic structure of amorphous SiNx:H," *Phys. Rev. B*, vol. 42, pp. 5677–5684, Sept. 1990.

[132] J. Park, S. Heo, J.-G. Chung, H. Kim, H. Lee, K. Kim, and G.-S. Park, "Bandgap measurement of thin dielectric films using monochromated STEM-EELS," *Ultramicroscopy*, vol. 109, pp. 1183–1188, Aug. 2009.

[133] L. A. J. Garvie, P. Rez, J. R. Alvarez, and P. R. Buseck, "Interband transitions of crystalline and amorphous SiO2: An electron energy-loss spectroscopy (EELS) study of the low-loss region," *Solid State Commun.*, vol. 106, pp. 303–307, May 1998.

[134] V. J. Keast, "Ab initio calculations of plasmons and interband transitions in the low-loss electron energy-loss spectrum," *J. Electron Spectrosc. Relat. Phenom.*, vol. 143, pp. 97–104, May 2005.

[135] R. J. Nicholls, J. M. Perkins, V. Nicolosi, D. W. McComb, P. D. Nellist, and J. R. Yates, "Low-loss EELS of 2D boron nitride," *J. Phys.: Conf. Ser.*, vol. 371, no. 1, p. 012060, 2012.

[136] C. T. Pan, R. R. Nair, U. Bangert, Q. Ramasse, R. Jalil, R. Zan, C. R. Seabourne, and A. J. Scott, "Nanoscale electron diffraction and plasmon spectroscopy of single- and few-layer boron nitride," *Phys. Rev. B*, vol. 85, no. 4, p. 045440, 2012.

[137] J. A. Scholl, A. L. Koh, and J. A. Dionne, "Quantum plasmon resonances of individual metallic nanoparticles," *Nature*, vol. 483, pp. 421–427, Mar. 2012.

[138] S. Raza, N. Stenger, S. Kadkhodazadeh, S. V. Fischer, N. Kostesha, A.-P. Jauho, A. Burrows, M. Wubs, and N. A. Mortensen, "Blueshift of the surface plasmon resonance in silver nanoparticles studied with EELS," *Nanophotonics*, vol. 2, no. 2, pp. 131–138, 2013.

[139] Y. Fang, W.-S. Chang, B. Willingham, P. Swanglap, S. Dominguez-Medina, and S. Link, "Plasmon Emission Quantum Yield of Single Gold Nanorods as a Function of Aspect Ratio," *ACS Nano*, vol. 6, pp. 7177–7184, Aug. 2012.

[140] B. S. Guiton, V. Iberi, S. Li, D. N. Leonard, C. M. Parish, P. G. Kotula, M. Varela, G. C. Schatz, S. J. Pennycook, and J. P. Camden, "Correlated Optical Measurements and Plasmon Mapping of Silver Nanorods," *Nano Lett.*, vol. 11, no. 8, pp. 3482–3488, 2011.

[141] A. L. Koh, D. W. McComb, S. A. Maier, H. Y. Low, and J. K. W. Yang, "Sub-10 nm patterning of gold nanostructures on silicon-nitride membranes for plasmon mapping with electron energy-loss spectroscopy," *J. Vac. Sci. Technol. B*, vol. 28, pp. C6O45–C6O49, Nov. 2010.

[142] M. N'Gom, J. Ringnalda, J. F. Mansfield, A. Agarwal, N. Kotov, N. J. Zaluzec, and T. B. Norris, "Single Particle Plasmon Spectroscopy of Silver Nanowires and Gold Nanorods," *Nano Lett.*, vol. 8, no. 10, pp. 3200–3204, 2008.

[143] M. B. Gawande, A. Goswami, T. Asefa, H. Guo, A. V. Biradar, D.-L. Peng, R. Zboril, and R. S. Varma, "Core–shell nanoparticles: Synthesis and applications in catalysis and electrocatalysis," *Chem. Soc. Rev.*, vol. 44, pp. 7540–7590, Oct. 2015.

[144] H. A. Atwater and A. Polman, "Plasmonics for improved photovoltaic devices," in *Materials for Sustainable Energy*, pp. 1–11, Co-Published with Macmillan Publishers Ltd, UK, Oct. 2010.

[145] B. Sharma, R. R. Frontiera, A.-I. Henry, E. Ringe, and R. P. Van Duyne, "SERS: Materials, applications, and the future," *Mater. Today*, vol. 15, pp. 16–25, Jan. 2012.

[146] P. K. Jain, I. H. El-Sayed, and M. A. El-Sayed, "Au nanoparticles target cancer," *Nano Today*, vol. 2, pp. 18–29, Feb. 2007.

[147] M. B. Cortie and A. M. McDonagh, "Synthesis and Optical Properties of Hybrid and Alloy Plasmonic Nanoparticles," *Chem. Rev.*, vol. 111, pp. 3713–3735, June 2011.

[148] M. G. Blaber, M. D. Arnold, and M. J. Ford, "A review of the optical properties of alloys and intermetallics for plasmonics," *J. Phys.: Condens. Matter*, vol. 22, p. 143201, Mar. 2010.

[149] Y. Yang, J. Shi, G. Kawamura, and M. Nogami, "Preparation of Au–Ag, Ag–Au core–shell bimetallic nanoparticles for surface-enhanced Raman scattering," *Scripta Mater.*, vol. 58, pp. 862–865, May 2008.

[150] K. Mallik, M. Mandal, N. Pradhan, and T. Pal, "Seed Mediated Formation of Bimetallic Nanoparticles by UV Irradiation: A Photochemical Approach for the Preparation of "Core-Shell" Type Structures," *Nano Lett.*, vol. 1, pp. 319–322, June 2001.

[151] J. H. Hodak, A. Henglein, M. Giersig, and G. V. Hartland, "Laser-Induced Inter-Diffusion in AuAg Core-Shell Nanoparticles," *J. Phys. Chem. B*, vol. 104, pp. 11708–11718, Dec. 2000.

[152] A. K. Samal, L. Polavarapu, S. Rodal-Cedeira, L. M. Liz-Marzán, J. Pérez-Juste, and I. Pastoriza-Santos, "Size Tunable Au@Ag Core–Shell Nanoparticles: Synthesis and Surface-Enhanced Raman Scattering Properties," *Langmuir*, vol. 29, pp. 15076–15082, Dec. 2013.

[153] S. K. Cha, J. H. Mun, T. Chang, S. Y. Kim, J. Y. Kim, H. M. Jin, J. Y. Lee, J. Shin, K. H. Kim, and S. O. Kim, "Au–Ag Core–Shell Nanoparticle Array by Block Copolymer Lithography for Synergistic Broadband Plasmonic Properties," *ACS Nano*, vol. 9, pp. 5536–5543, May 2015.

[154] Y. Chen, H. Wu, Z. Li, P. Wang, L. Yang, and Y. Fang, "The Study of Surface Plasmon in Au/Ag Core/Shell Compound Nanoparticles," *Plasmonics*, vol. 7, pp. 509–513, Sept. 2012.

[155] M. S. Shore, J. Wang, A. C. Johnston-Peck, A. L. Oldenburg, and J. B. Tracy, "Synthesis of Au(Core)/Ag(Shell) Nanoparticles and their Conversion to AuAg Alloy Nanoparticles," *Small*, vol. 7, no. 2, pp. 230–234, 2011.

[156] M. P. Mallin and C. J. Murphy, "Solution-Phase Synthesis of Sub-10 nm Au-Ag Alloy Nanoparticles," *Nano Lett.*, vol. 2, pp. 1235–1237, Nov. 2002.

[157] B. Baruah and M. Kiambuthi, "Facile synthesis of silver and bimetallic silver–gold nanoparticles and their applications in surface-enhanced Raman scattering," *RSC Adv.*, vol. 4, pp. 64860–64870, Nov. 2014.

[158] R. Fernández-Perea, L. F. Gómez, C. Cabrillo, M. Pi, A. O. Mitrushchenkov, A. F. Vilesov, and M. P. de Lara-Castells, "Helium Droplet-Mediated Deposition and Aggregation of Nanoscale Silver Clusters on Carbon Surfaces," *J. Phys. Chem. C*, vol. 121, pp. 22248–22257, Oct. 2017.

[159] A. Volk, P. Thaler, M. Koch, E. Fisslthaler, W. Grogger, and W. E. Ernst, "High resolution electron microscopy of Ag-clusters in crystalline and non-crystalline morphologies grown inside superfluid helium nanodroplets," *J. Chem. Phys.*, vol. 138, p. 214312, June 2013.

[160] S. B. Emery, K. B. Rider, B. K. Little, and C. M. Lindsay, "Helium Droplet Assembled Nanocluster Films: Cluster Formation and Deposition Rates," *J. Phys. Chem. C*, vol. 117, pp. 2358–2368, Feb. 2013.

[161] C. Kittel, *Introduction to Solid State Physics*. John Wiley & Sons, Inc., eighth ed., 2005.

[162] E. C. Le Ru, E. Blackie, M. Meyer, and P. G. Etchegoin, "Surface Enhanced Raman Scattering Enhancement Factors: A Comprehensive Study," *J. Phys. Chem. C*, vol. 111, pp. 13794–13803, Sept. 2007.

[163] P. H. C. Camargo, L. Au, M. Rycenga, W. Li, and Y. Xia, "Measuring the SERS enhancement factors of dimers with different structures constructed from silver nanocubes," *Chem. Phys. Lett.*, vol. 484, pp. 304–308, Jan. 2010.

[164] T. Walther and C. J. Humphreys, "A quantitative study of compositional profiles of chemical vapour-deposited strained silicon–germanium/silicon layers by transmission electron microscopy," *J. Cryst. Growth*, vol. 197, pp. 113–128, Feb. 1999.

[165] H. Hövel, S. Fritz, A. Hilger, U. Kreibig, and M. Vollmer, "Width of cluster plasmon resonances: Bulk dielectric functions and chemical interface damping," *Phys. Rev. B*, vol. 48, pp. 18178–18188, Dec. 1993.

[166] A. Kuzma, M. Weis, M. Daricek, J. Uhrik, F. Horinek, M. Donoval, F. Uherek, and D. Donoval, "Plasmonic properties of Au-Ag nanoparticles: Distinctiveness of metal arrangements by optical study," *J. Appl. Phys.*, vol. 115, p. 053517, Feb. 2014.

[167] M. Moskovits, I. Srnová-Šloufová, and B. Vlčková, "Bimetallic Ag–Au nanoparticles: Extracting meaningful optical constants from the surface-plasmon extinction spectrum," *J. Chem. Phys.*, vol. 116, no. 23, pp. 10435–10446, 2002.

[168] W.-T. Wu, C.-H. Chen, C.-Y. Chiang, and L.-K. Chau, "Effect of Surface Coverage of Gold Nanoparticles on the Refractive Index Sensitivity in Fiber-Optic Nanoplasmonic Sensing," *Sensors*, vol. 18, p. 1759, June 2018.

[169] P. K. Jain and M. A. El-Sayed, "Plasmonic coupling in noble metal nanostructures," *Chem. Phys. Lett.*, vol. 487, pp. 153–164, Mar. 2010.

[170] T. P. Martin, "Shells of atoms," *Phys. Rep.*, vol. 273, pp. 199–241, Aug. 1996.

[171] V. Myroshnychenko, J. Rodríguez-Fernández, I. Pastoriza-Santos, A. M. Funston, C. Novo, P. Mulvaney, L. M. Liz-Marzán, and F. J. G. de Abajo, "Modelling the optical response of gold nanoparticles," *Chem. Soc. Rev.*, vol. 37, pp. 1792–1805, Aug. 2008.

[172] M. Pellarin, M. Broyer, J. Lermé, M.-A. Lebeault, J. Ramade, and E. Cottancin, "Plasmon resonances tailored by Fano profiles in silver-based core–shell nanoparticles," *Phys. Chem. Chem. Phys.*, vol. 18, pp. 4121–4133, Jan. 2016.

[173] X. Song, G. Wang, Y. Ma, S. Jiang, W. Yue, S. Xu, and C. Wang, "Density functional theory study of NEXAFS spectra of 4-methylbenzenethiol molecule," *Chem. Phys. Lett.*, vol. 645, pp. 164–168, Feb. 2016.

[174] O. Endo, M. Nakamura, and K. Amemiya, "Depth-dependent C K-NEXAFS spectra for self-assembled monolayers of 4-methylbenzenethiol and 4-ethylbenzenethiol on Au(111)," *J. Electron Spectrosc. Relat. Phenom.*, vol. 187, pp. 72–76, Apr. 2013.

[175] A. Ulman, "Formation and Structure of Self-Assembled Monolayers," *Chem. Rev.*, vol. 96, pp. 1533–1554, Jan. 1996.

[176] K. Ikeda, S. Suzuki, and K. Uosaki, "Enhancement of SERS Background through Charge Transfer Resonances on Single Crystal Gold Surfaces of Various Orientations," *J. Am. Chem. Soc.*, vol. 135, pp. 17387–17392, Nov. 2013.

[177] S. K. Ghosh, S. Nath, S. Kundu, K. Esumi, and T. Pal, "Solvent and Ligand Effects on the Localized Surface Plasmon Resonance (LSPR) of Gold Colloids," *J. Phys. Chem. B*, vol. 108, pp. 13963–13971, Sept. 2004.

[178] F. S. Ameer, Y. Zhou, S. Zou, and D. Zhang, "Wavelength-Dependent Correlations between Ultraviolet–Visible Intensities and Surface Enhanced Raman Spectroscopic Enhancement Factors of Aggregated Gold and Silver Nanoparticles," *J. Phys. Chem. C*, vol. 118, pp. 22234–22242, Sept. 2014.

[179] P. R. West, S. Ishii, G. V. Naik, N. K. Emani, V. M. Shalaev, and A. Boltasseva, "Searching for better plasmonic materials," *Laser Photonics Rev.*, vol. 4, no. 6, pp. 795–808, 2010.

[180] G. Maidecchi, G. Gonella, R. Proietti Zaccaria, R. Moroni, L. Anghinolfi, A. Giglia, S. Nannarone, L. Mattera, H.-L. Dai, M. Canepa, and F. Bisio, "Deep Ultraviolet Plasmon Resonance in Aluminum Nanoparticle Arrays," *ACS Nano*, vol. 7, pp. 5834–5841, July 2013.

[181] Q. Wu, C. J. Ridge, S. Zhao, D. Zakharov, J. Cen, X. Tong, E. Connors, D. Su, E. A. Stach, C. M. Lindsay, and A. Orlov, "Development of a New Generation of Stable, Tunable, and Catalytically Active Nanoparticles Produced by the Helium Nanodroplet Deposition Method," *J. Phys. Chem. Lett.*, vol. 7, pp. 2910–2914, Aug. 2016.

[182] S. Linic, P. Christopher, and D. B. Ingram, "Plasmonic-metal nanostructures for efficient conversion of solar to chemical energy," *Nat. Mater.*, vol. 10, pp. 911–921, Dec. 2011.

[183] C. B. Ong, L. Y. Ng, and A. W. Mohammad, "A review of ZnO nanoparticles as solar photocatalysts: Synthesis, mechanisms and applications," *Renew. Sust. Energ. Rev.*, vol. 81, pp. 536–551, Jan. 2018.

[184] K. H. Qi, B. Cheng, J. Yu, and W. Ho, "Review on the improvement of the photocatalytic and antibacterial activities of ZnO," *J. Alloys Compd.*, vol. 727, pp. 792–820, Dec. 2017.

[185] S. K. Mishra, R. K. Srivastava, S. G. Prakash, R. S. Yadav, and A. C. Panday, "Photoluminescence and photoconductive characteristics of hydrothermally synthesized ZnO nanoparticles," *Opto-Electronics Review*, vol. 18, no. 4, pp. 467–473, 2010.

[186] Ü. Özgür, D. Hofstetter, and H. Morkoc, "ZnO Devices and Applications: A Review of Current Status and Future Prospects," *Proc. IEEE*, vol. 98, pp. 1255–1268, July 2010.

[187] W.-W. Wang and Y.-J. Zhu, "Shape-controlled synthesis of zinc oxide by microwave heating using an imidazolium salt," *Inorg. Chem. Commun.*, vol. 7, pp. 1003–1005, Sept. 2004.

[188] A. Kołodziejczak-Radzimska and T. Jesionowski, "Zinc Oxide—From Synthesis to Application: A Review," *Materials*, vol. 7, pp. 2833–2881, Apr. 2014.

[189] B. Ghanbari Shohany and A. Khorsand Zak, "Doped ZnO nanostructures with selected elements - Structural, morphology and optical properties: A review," *Ceram. Int.*, vol. 46, pp. 5507–5520, Apr. 2020.

[190] R. Georgekutty, M. K. Seery, and S. C. Pillai, "A Highly Efficient Ag-ZnO Photocatalyst: Synthesis, Properties, and Mechanism," *J. Phys. Chem. C*, vol. 112, pp. 13563–13570, Sept. 2008.

[191] M. Xiao, R. Jiang, F. Wang, C. Fang, J. Wang, and J. C. Yu, "Plasmon-enhanced chemical reactions," *J. Mater. Chem. A*, vol. 1, pp. 5790–5805, Apr. 2013.

[192] L. F. Gomez, K. R. Ferguson, J. P. Cryan, C. Bacellar, R. M. P. Tanyag, C. Jones, S. Schorb, D. Anielski, A. Belkacem, C. Bernando, R. Boll, J. Bozek, S. Carron, G. Chen, T. Delmas, L. Englert, S. W. Epp, B. Erk, L. Foucar, R. Hartmann, A. Hexemer, M. Huth, J. Kwok, S. R. Leone, J. H. S. Ma, F. R. N. C. Maia, E. Malmerberg, S. Marchesini, D. M. Neumark, B. Poon, J. Prell, D. Rolles, B. Rudek, A. Rudenko, M. Seifrid, K. R. Siefermann, F. P. Sturm, M. Swiggers, J. Ullrich, F. Weise, P. Zwart, C. Bostedt, O. Gessner, and A. F. Vilesov, "Shapes and vorticities of superfluid helium nanodroplets," *Science*, vol. 345, pp. 906–909, Aug. 2014.

[193] O. Gessner and A. F. Vilesov, "Imaging Quantum Vortices in Superfluid Helium Droplets," *Annu. Rev. Phys. Chem.*, vol. 70, no. 1, pp. 173–198, 2019.

[194] M. Lasserus, D. Knez, M. Schnedlitz, A. W. Hauser, F. Hofer, and W. E. Ernst, "On the passivation of iron particles at the nanoscale," *Nanoscale Adv.*, vol. 1, pp. 2276–2283, June 2019.

[195] M. P. de Lara-Castells, N. F. Aguirre, H. Stoll, A. O. Mitrushchenkov, D. Mateo, and M. Pi, "Communication: Unraveling the 4He droplet-mediated soft-landing from ab initio-assisted and time-resolved density functional simulations: Au@4He300/TiO2(110)," *J. Chem. Phys.*, vol. 142, p. 131101, Apr. 2015.

[196] M. He, L. Protesescu, R. Caputo, F. Krumeich, and M. V. Kovalenko, "A General Synthesis Strategy for Monodisperse Metallic and Metalloid Nanoparticles (In, Ga, Bi, Sb, Zn, Cu, Sn, and Their Alloys) via in Situ Formed Metal Long-Chain Amides," *Chem. Mater.*, vol. 27, pp. 635–647, Jan. 2015.

[197] M. Schreyer, L. Guo, S. Thirunahari, F. Gao, and M. Garland, "Simultaneous determination of several crystal structures from powder mixtures: The combination of powder X-ray diffraction, band-target entropy minimization and Rietveld methods," *J. Appl. Cryst.*, vol. 47, pp. 659–667, Apr. 2014.

[198] D. Prieur, W. Bonani, K. Popa, O. Walter, K. W. Kriegsman, M. H. Engelhard, X. Guo, R. Eloirdi, T. Gouder, A. Beck, T. Vitova, A. C. Scheinost, K. Kvashnina, and P. Martin, "Size Dependence of Lattice Parameter and Electronic Structure in CeO2 Nanoparticles," *Inorg. Chem.*, vol. 59, pp. 5760–5767, Apr. 2020.

[199] J. Schindelin, I. Arganda-Carreras, E. Frise, V. Kaynig, M. Longair, T. Pietzsch, S. Preibisch, C. Rueden, S. Saalfeld, B. Schmid, J.-Y. Tinevez, D. J. White, V. Hartenstein, K. Eliceiri, P. Tomancak, and A. Cardona, "Fiji: An open-source platform for biological-image analysis," *Nat. Methods*, vol. 9, pp. 676–682, July 2012.

[200] J. Lehmann, M. Merschdorf, W. Pfeiffer, A. Thon, S. Voll, and G. Gerber, "Surface Plasmon Dynamics in Silver Nanoparticles Studied by Femtosecond Time-Resolved Photoemission," *Phys. Rev. Lett.*, vol. 85, pp. 2921–2924, Oct. 2000.

[201] S. Evans, "Energy calibration secondary standards for X-ray photoelectron spectrometers," *Surf. Interface Anal.*, vol. 7, pp. 299–302, Dec. 1985.

[202] S. W. Gaarenstroom and N. Winograd, "Initial and final state effects in the ESCA spectra of cadmium and silver oxides," *J. Chem. Phys.*, vol. 67, pp. 3500–3506, Oct. 1977.

[203] L. Ley, S. P. Kowalczyk, F. R. McFeely, R. A. Pollak, and D. A. Shirley, "X-Ray Photoemission from Zinc: Evidence for Extra-Atomic Relaxation via Semilocalized Excitons," *Phys. Rev. B*, vol. 8, pp. 2392–2402, Sept. 1973.

[204] G. Schön, "Auger and direct electron spectra in X-ray photoelectron studies of zinc, zinc oxide, gallium and gallium oxide," *J. Electron Spectrosc. Relat. Phenom.*, vol. 2, pp. 75–86, Jan. 1973.

[205] S. Gutmann, M. Conrad, M. A. Wolak, M. M. Beerbom, and R. Schlaf, "Work function measurements on nano-crystalline zinc oxide surfaces," *J. Appl. Phys.*, vol. 111, p. 123710, June 2012.

[206] M. Misra, P. Kapur, M. K. Nayak, and M. Singla, "Synthesis and visible photocatalytic activities of a Au@Ag@ZnO triple layer core–shell nanostructure," *New J. Chem.*, vol. 38, pp. 4197–4203, Aug. 2014.

[207] K. Aranishi, H.-L. Jiang, T. Akita, M. Haruta, and Q. Xu, "One-step synthesis of magnetically recyclable Au/Co/Fe triple-layered core-shell nanoparticles

as highly efficient catalysts for the hydrolytic dehydrogenation of ammonia borane," *Nano Res.*, vol. 4, pp. 1233–1241, Dec. 2011.

[208] V. Mazumder, M. Chi, K. L. More, and S. Sun, "Synthesis and Characterization of Multimetallic Pd/Au and Pd/Au/FePt Core/Shell Nanoparticles," *Angew. Chem. Int. Ed.*, vol. 49, no. 49, pp. 9368–9372, 2010.

[209] A. P. LaGrow, D. C. Lloyd, P. L. Gai, and E. D. Boyes, "In Situ Scanning Transmission Electron Microscopy of Ni Nanoparticle Redispersion via the Reduction of Hollow NiO," *Chem. Mater.*, vol. 30, pp. 197–203, Jan. 2018.

[210] M. Munzinger, C. Wiemann, M. Rohmer, L. Guo, M. Aeschlimann, and M. Bauer, "The lateral photoemission distribution from a defined cluster/-substrate system as probed by photoemission electron microscopy," *New J. Phys.*, vol. 7, pp. 68–68, Feb. 2005.

[211] M. Rohmer, F. Ghaleh, M. Aeschlimann, M. Bauer, and H. Hövel, "Mapping the femtosecond dynamics of supported clusters with nanometer resolution," *Eur. Phys. J. D*, vol. 45, pp. 491–499, Dec. 2007.

[212] A. G. Knapp, "Surface potentials and their measurement by the diode method," *Surf. Sci.*, vol. 34, pp. 289–316, Jan. 1973.

[213] F. Evers, C. Rakete, K. Watanabe, D. Menzel, and H.-J. Freund, "Two-photon photoemission from silver nanoparticles on thin alumina films: Role of plasmon excitation," *Surf. Sci.*, vol. 593, pp. 43–48, Nov. 2005.

[214] E. Roduner, "Size matters: Why nanomaterials are different," *Chem. Soc. Rev.*, vol. 35, pp. 583–592, June 2006.

[215] D. Wang and D. Astruc, "The recent development of efficient Earth-abundant transition-metal nanocatalysts," *Chem. Soc. Rev.*, vol. 46, pp. 816–854, Feb. 2017.

[216] C. Clavero, "Plasmon-induced hot-electron generation at nanoparticle/metal-oxide interfaces for photovoltaic and photocatalytic devices," *Nat. Photonics*, vol. 8, pp. 95–103, Feb. 2014.

[217] C.-M. Jiang, L. R. Baker, J. M. Lucas, J. Vura-Weis, A. P. Alivisatos, and S. R. Leone, "Characterization of Photo-Induced Charge Transfer and Hot Carrier Relaxation Pathways in Spinel Cobalt Oxide (Co3O4)," *J. Phys. Chem. C*, vol. 118, pp. 22774–22784, Oct. 2014.

[218] J. Vura-Weis, C.-M. Jiang, C. Liu, H. Gao, J. M. Lucas, F. M. F. de Groot, P. Yang, A. P. Alivisatos, and S. R. Leone, "Femtosecond M2,3-Edge Spectroscopy of Transition-Metal Oxides: Photoinduced Oxidation State Change in α-Fe2O3," *J. Phys. Chem. Lett.*, vol. 4, pp. 3667–3671, Nov. 2013.

[219] L. R. Baker, C.-M. Jiang, S. T. Kelly, J. M. Lucas, J. Vura-Weis, M. K. Gilles, A. P. Alivisatos, and S. R. Leone, "Charge Carrier Dynamics of Photoexcited Co3O4 in Methanol: Extending High Harmonic Transient Absorption Spectroscopy to Liquid Environments," *Nano Lett.*, vol. 14, pp. 5883–5890, Oct. 2014.

[220] L. Liao, Q. Zhang, Z. Su, Z. Zhao, Y. Wang, Y. Li, X. Lu, D. Wei, G. Feng, Q. Yu, X. Cai, J. Zhao, Z. Ren, H. Fang, F. Robles-Hernandez, S. Baldelli, and J. Bao, "Efficient solar water-splitting using a nanocrystalline CoO photocatalyst," *Nat. Nanotechnol.*, vol. 9, pp. 69–73, Jan. 2014.

[221] M. Zhang, M. de Respinis, and H. Frei, "Time-resolved observations of water oxidation intermediates on a cobalt oxide nanoparticle catalyst," *Nat. Chem.*, vol. 6, pp. 362–367, Apr. 2014.

[222] J. Zhu, K. Kailasam, A. Fischer, and A. Thomas, "Supported Cobalt Oxide Nanoparticles As Catalyst for Aerobic Oxidation of Alcohols in Liquid Phase," *ACS Catal.*, vol. 1, pp. 342–347, Apr. 2011.

[223] D. L. Peng, K. Sumiyama, T. J. Konno, T. Hihara, and S. Yamamuro, "Characteristic transport properties of CoO-coated monodispersive Co cluster assemblies," *Phys. Rev. B*, vol. 60, pp. 2093–2100, July 1999.

[224] D.-H. Ha, L. M. Moreau, S. Honrao, R. G. Hennig, and R. D. Robinson, "The Oxidation of Cobalt Nanoparticles into Kirkendall-Hollowed CoO and Co3O4: The Diffusion Mechanisms and Atomic Structural Transformations," *J. Phys. Chem. C*, vol. 117, pp. 14303–14312, July 2013.

[225] S. Jia, C.-H. Hsia, and D. H. Son, "In Situ Study of Room-Temperature Oxidation Kinetics of Colloidal Co Nanocrystals Investigated by Faraday Rotation Measurement," *J. Phys. Chem. C*, vol. 115, pp. 92–96, Jan. 2011.

[226] P. M. Kraus, M. Zürch, S. K. Cushing, D. M. Neumark, and S. R. Leone, "The ultrafast X-ray spectroscopic revolution in chemical dynamics," *Nat. Rev. Chem.*, vol. 2, pp. 82–94, June 2018.

[227] M. E. Vaida, B. M. Marsh, and S. R. Leone, "Nonmetal to Metal Transition and Ultrafast Charge Carrier Dynamics of Zn Clusters on p-Si(100) by

fs-XUV Photoemission Spectroscopy," *Nano Lett.*, vol. 18, pp. 4107–4114, July 2018.

[228] E. Loginov, L. F. Gomez, N. Chiang, A. Halder, N. Guggemos, V. V. Kresin, and A. F. Vilesov, "Photoabsorption of Ag_N (N approx. 6-6000) Nanoclusters Formed in Helium Droplets: Transition from Compact to Multicenter Aggregation," *Phys. Rev. Lett.*, vol. 106, p. 233401, June 2011.

[229] J. B. Tracy, D. N. Weiss, D. P. Dinega, and M. G. Bawendi, "Exchange biasing and magnetic properties of partially and fully oxidized colloidal cobalt nanoparticles," *Phys. Rev. B*, vol. 72, p. 064404, Aug. 2005.

[230] P. Bazylewski, D. W. Boukhvalov, A. I. Kukharenko, E. Z. Kurmaev, A. Hunt, A. Moewes, Y. H. Lee, S. O. Cholakh, and G. S. Chang, "The characterization of Co-nanoparticles supported on graphene," *RSC Adv.*, vol. 5, pp. 75600–75606, Sept. 2015.

[231] J. Wang, *Low Energy Electron Diffraction Studies of Transition Metal Oxide Surfaces and Films*. PhD thesis, Martin-Luther-Universität Halle-Wittenberg, 2005.

[232] M. Ghosh, E. V. Sampathkumaran, and C. N. R. Rao, "Synthesis and Magnetic Properties of CoO Nanoparticles," *Chem. Mater.*, vol. 17, pp. 2348–2352, May 2005.

[233] L. Meziane, C. Salzemann, C. Aubert, H. Gérard, C. Petit, and M. Petit, "Hcp cobalt nanocrystals with high magnetic anisotropy prepared by easy one-pot synthesis," *Nanoscale*, vol. 8, pp. 18640–18645, Nov. 2016.

[234] V. A. de la Peña O'Shea, I. d. P. R. Moreira, A. Roldán, and F. Illas, "Electronic and magnetic structure of bulk cobalt: The α, β, and ϵ-phases from density functional theory calculations," *J. Chem. Phys.*, vol. 133, p. 024701, July 2010.

[235] C. Y. Ma, Z. Mu, J. J. Li, Y. G. Jin, J. Cheng, G. Q. Lu, Z. P. Hao, and S. Z. Qiao, "Mesoporous Co3O4 and Au/Co3O4 Catalysts for Low-Temperature Oxidation of Trace Ethylene," *J. Am. Chem. Soc.*, vol. 132, pp. 2608–2613, Mar. 2010.

[236] B. L. Henke, E. M. Gullikson, and J. C. Davis, "X-Ray Interactions: Photoabsorption, Scattering, Transmission, and Reflection at E = 50-30,000 eV, Z = 1-92," *At. Data Nucl. Data Tables*, vol. 54, pp. 181–342, July 1993.

[237] A. C. Thompson and D. Vaughan, *X-Ray Data Booklet*. Lawrence Berkeley National Library, third ed., 2009.

[238] Z. Wei, L. Tian, J. Li, Y. Lu, M. Yang, and Z.-H. Loh, "Tracking Ultrafast Bond Dissociation Dynamics at 0.1 Å Resolution by Femtosecond Extreme Ultraviolet Absorption Spectroscopy," *J. Phys. Chem. Lett.*, vol. 9, pp. 5742–5747, Oct. 2018.

[239] A. Naldoni, F. Riboni, U. Guler, A. Boltasseva, V. M. Shalaev, and A. V. Kildishev, "Solar-Powered Plasmon-Enhanced Heterogeneous Catalysis," *Nanophotonics*, vol. 5, pp. 112–133, June 2016.

[240] M. L. Brongersma, N. J. Halas, and P. Nordlander, "Plasmon-induced hot carrier science and technology," *Nat. Nanotechnol.*, vol. 10, pp. 25–34, Jan. 2015.

[241] F. Siegrist, J. A. Gessner, M. Ossiander, C. Denker, Y.-P. Chang, M. C. Schröder, A. Guggenmos, Y. Cui, J. Walowski, U. Martens, J. K. Dewhurst, U. Kleineberg, M. Münzenberg, S. Sharma, and M. Schultze, "Light-wave dynamic control of magnetism," *Nature*, vol. 571, pp. 240–244, July 2019.

[242] R. Dehghan, T. W. Hansen, J. B. Wagner, A. Holmen, E. Rytter, Ø. Borg, and J. C. Walmsley, "In-Situ Reduction of Promoted Cobalt Oxide Supported on Alumina by Environmental Transmission Electron Microscopy," *Catal. Lett.*, vol. 141, p. 754, May 2011.

[243] Q. Meng, S. Guo, X. Zhao, and S. Veintemillas-Verdaguer, "Bulk metastable cobalt in fcc crystal structure," *J. Alloys Compd.*, vol. 580, pp. 187–190, Dec. 2013.

[244] V. Bartůněk, Š. Huber, D. Sedmidubský, Z. Sofer, P. Šimek, and O. Jankovský, "CoO and Co3O4 nanoparticles with a tunable particle size," *Ceram. Int.*, vol. 40, pp. 12591–12595, Sept. 2014.

[245] V. D. Jović, V. Maksimović, M. G. Pavlović, and K. I. Popov, "Morphology, internal structure and growth mechanism of electrodeposited Ni and Co powders," *J. Solid State Electrochem.*, vol. 10, pp. 373–379, June 2006.

[246] Q. Liu, X. Cao, T. Wang, C. Wang, Q. Zhang, and L. Ma, "Synthesis of shape-controllable cobalt nanoparticles and their shape-dependent performance in glycerol hydrogenolysis," *RSC Adv.*, vol. 5, pp. 4861–4871, Dec. 2014.